Numerical Modeling and Experimental Testing of a Wave Energy Converter

deliverable D4.2

Zurkinden, Andrew Stephen; Kramer, Morten; Ferri, Francesco; Kofoed, Jens Peter

Publication date:
2013

Document Version
Publisher's PDF, also known as Version of record

S D W E D

STRUCTURAL DESIGN OF WAVE ENERGY DEVICES

Numerical modeling and experimental testing of a Wave Energy Converter

A. S. Zurkinden
M. M. Kramer
F. Ferri
J. P. Kofoed

Deliverable D4.2

ISSN 1901-726X
DCE Technical Report No. 153

AALBORG UNIVERSITY
Department of Civil Engineering

Aalborg University
Department of Civil Engineering
Structural Design of Wave Energy Devices

DCE Technical Report No. 153

Numerical modeling and experimental testing of a Wave Energy Converter

by

A. S. Zurkinden
M. M. Kramer
F. Ferri
J. P. Kofoed

May. 2013

Scientific Publications at the Department of Civil Engineering

Technical Reports are published for timely dissemination of research results and scientific work carried out at the Department of Civil Engineering (DCE) at Aalborg University. This medium allows publication of more detailed explanations and results than typically allowed in scientific journals.

Technical Memoranda are produced to enable the preliminary dissemination of scientific work by the personnel of the DCE where such release is deemed to be appropriate. Documents of this kind may be incomplete or temporary versions of papers—or part of continuing work. This should be kept in mind when references are given to publications of this kind.

Contract Reports are produced to report scientific work carried out under contract. Publications of this kind contain confidential matter and are reserved for the sponsors and the DCE. Therefore, Contract Reports are generally not available for public circulation.

Lecture Notes contain material produced by the lecturers at the DCE for educational purposes. This may be scientific notes, lecture books, example problems or manuals for laboratory work, or computer programs developed at the DCE.

Theses are monograms or collections of papers published to report the scientific work carried out at the DCE to obtain a degree as either PhD or Doctor of Technology. The thesis is publicly available after the defence of the degree.

Latest News is published to enable rapid communication of information about scientific work carried out at the DCE. This includes the status of research projects, developments in the laboratories, information about collaborative work and recent research results.

Published 2012 by
Aalborg University
Department of Civil Engineering
Sohngaardsholmsvej 57,
DK-9000 Aalborg, Denmark

Printed in Aalborg at Aalborg University

ISSN 1901-726X
DCE Technical Report No. 153

Numerical modeling and experimental testing of a Wave Energy Converter.

by

Andrew S. Zurkinden and Morten M. Kramer, Francesco Ferri, Jens Peter Kofoed

DCE Technical Report No. 153
Department of Civil Engineering
Faculty of Engineering and Science, Aalborg University
ISSN 1901-726X, Deliverable 4.2 in the SDWED project.

Acknowledgement

The Structural Design of Wave Energy Devices project (SDWED) is an international research alliance supported by the Danish Council for Strategic Research.

Summary

The objective of this document is to summarize the outcome of the research which has been carried out during the period Mai 2011 until June 2012 i.e. during the first year of the PhD study. The work has been done in collaboration with the co-authors. The aim of the project was primarily to provide numerical values for comparison with the experimental test results which were carried out in the same time. It is for this reason why Chapter 4 does consist exclusively of numerical values. Experimental values and measured time series of wave elevations have been used throughout the report in order to a) validate the numerical model and b) preform stochastic analysis. The latter technique is introduced in order to optimize the control parameters of the power take off system. The content is summarized in the following manner:

Chapter 1 starts with an introduction. A brief literature review about optimal control of wave energy converters is given.

In **Chapter 2** the dynamic equation of the laboratory scale Wavestar model is presented. The calculation of the hydrodynamic loads is based on the diffraction/radiation theory. The boundary element method is used to solve the flow problem around the geometry in 3D. The hydrodynamic loads are given in the frequency domain and are linearized by assuming a constant equilibrium position. The exact hydrodynamic force would result if the "exact" or "actual" position of the float in the waves is considered. However, in general the analyses by using non-linear 3D codes are time consuming and the justification to carry out a non-linear analysis at the design stage must be given. In the case of the Wavestar model the wetted surface does not undergo large changes in head seas. Thus the linear assumption is justified. A simpler approach to account for the predominant non-linear forces such as the Froude-Krylov and the buoyancy forces is to evaluate the forces for each position of the float. In Chapter 2.1.1 a simple methodology is described which addresses the non-linear hydrostatic restoring moment. The results of the numerical implementation of the non-linear force are presented in the first paper; see Appendix A.

Chapter 2 starts directly by setting up the equation of motion in the time domain. The integro-differential equation is formulated for the laboratory model which is also known as the Cummin's equation. In order to solve the problem in the time domain a convolution product between the radiation force and the body velocity must be solved. Two different methodologies are described. In the second model the convolution integral is replaced by a rational approximation of the radiation force. A state-space model is introduced to formulate the equation of motion. Chapter 2.3 discusses the introduction of a control moment.

In **Chapter 3** the experimental setup of the laboratory model is described. The model is basically a reproduction of the Wavestar prototype which is located in Hanstholm, Denmark. The model scale is 1:20. Ten different wave states are analyzed. A stochastic analysis is carried out of the measured wave states. The optimal damping coefficient is calculated by taking into account the auto-correlation coefficient of irregular waves.

In **Chapter 4** the results from the experimental and numerical calculation are presented. Four different control strategies are applied. The numerical results are compared with the experimental tests for the passive damped point absorber. Unfortunately no experimental results

are available for the case where a negative spring stiffness is applied to the controller. In general the comparison shows very good agreement between the numerical and experimental results.

Contents

List of Figures

List of Tables

CHAPTER 1
Introduction

1.1 Introduction

The dynamical behaviour of wave energy converters (WEC's) has been extensively investigated during the past half century by means of analytical and numerical studies, including testing at laboratory scale and under real-sea conditions. Many concepts have been proposed such as the oscillating-water-column (OWC), the Pico OWC (Neumann *et al.* 2008), overtopping WEC types like the Wave Dragon (see `http://www.wavedragon.net`), multi-body point absorber concepts like e.g. FO^3 (Taghipour 2008) and the Wavestarenergy device (see `http://www.wavestarenergy.com`). Point absorbers constitute an important class of wave energy converters particularly with regard to offshore deployment.

The definition of a point absorber system lies in the ratio between the maximum geometrical dimension and the minimum wavelength of a representative sea state. If this ratio is considered to be small it may be concluded that the resonance bandwidth of the absorber is narrow and hence optimal control strategies can be very promising to maximize the power production. Oscillators with large horizontal extensions can also be classified as broad banded devices from a control point of view. Optimal control for these devices would be less effective than for point absorber concepts.

The use of control engineering to optimize the power absorption of point absorber wave energy converters was first proposed by Budal (Budal 1975). A maximum power is extracted from the waves, when the velocity of the body is in phase with the incoming wave excitation force at any time. At excitation frequencies away, a phase difference is present, and the power absorption is considerably reduced.

This behaviour can be observed in Fig. 1.1 and Fig. 1.2 for a laboratory scale model (1:20) of the Wavestar point absorber. The non-dimensional performance index is shown in the vertical axis; the peak period is displayed in the horizontal axis. Irregular waves based on a Pierson Moskovitz spectrum are analysed. The natural period of the oscillating system is 0.79 s. The red curve in the graph is based on experiments whereas the black dashed line is calculated with a time domain model, assuming linear fluid structure interaction. For peak periods close to the natural period, the capture width ratio reaches its maximum of about $\nu \cong 0.55$. On the other hand for peak periods larger than the natural period, the efficiency is considerably reduced; see the decrease of the efficiency curve in the two Figures. The black and red curves in the right

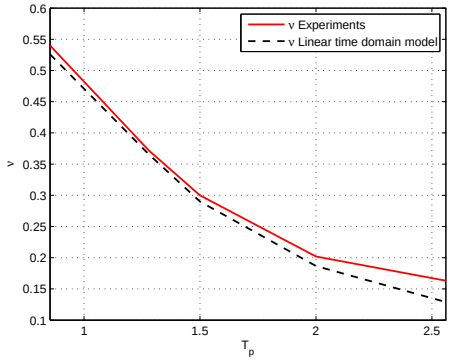

Figure 1.1 Non-dimensional performance index in function of the peak period, for irregular waves with a steepness factor of H_s/λ_p=0.02 - linear, passive damping.

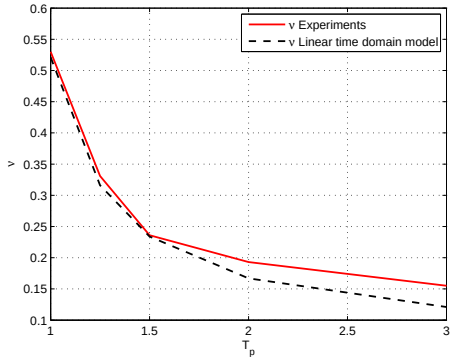

Figure 1.2 Non-dimensional performance index in function of the peak period, for irregular waves with a steepness factor of H_s/λ_p=0.04 - linear, passive damping.

plot are deviating for higher peak periods. This is due to the linearity assumption of the linear model. Higher and hence steeper waves tend to overtop the device more often. This effect is not captured by the linear numerical model however predominant for peak periods above 2.25 s.

One of the main objectives of optimal control, in the present context, is to increase the efficiency for the wave states where the peak periods are away from the natural period of the oscillator. The objective is to decrease the steepness of the efficiency curve for larger peak periods and thus to smooth out the efficiency curve.

"Optimal" control will be replaced by the word "sub-optimal" as it suits better the concepts presented in this work: the control is applied by using the peak period of the waves rather than the instantaneous wave period. In irregular waves the control problem becomes non-causal due to the fact that the input is not the direct cause for the output (Falnes 1995). Optimal control in irregular waves requires prediction of the future waves. All the calculation in the present case are based on the assumption that the wave force is fully known, thus one can talk about causal reactive control. The word reactive control reflects the fact that the dynamics of the oscillating system are changed during the power absorption process. In other words the natural period of the float is tuned to the peak period of the waves. This concept is also known as impedance matching which was first presented by (Falnes 2007).

In the 1970's a handful of independent reports were published introducing the theoretical fundamentals of maximum wave-power absorption. Salter (Salter 1974) pointed out the potential energy in ocean waves and highlights the design problems of such devices. In 1974 he reported that already more than hundred proposals of WECs concepts were registered at the British patent office. Salter illustrated the importance of experimental studies on wave energy in order to test their efficiency for power extraction. Furthermore he pointed out that the installation must be freely floating out at the sea. Rigid connections should be avoided wherever possible.

Evans (Evans 1976) pointed out that heaving bodies with an inbuilt hydrostatic spring and

hence a natural oscillation period shorter than the wave periods require negative applied spring stiffness from an external power source in order to oscillate in resonance.

Mei (Mei 1976) presented a design based on the idea of a tethered-float breakwater and reported criteria's for maximum power extraction. He pointed out that the energy extraction must be equal to the rate of radiation damping of the device. For a body of one degree of freedom and symmetric about one axis, the maximum efficiency at a given frequency can reach 50%. For asymmetric bodies it can even be greater than the half of the incoming energy, like in the case of Wavestar, for instance. For a body with two degrees of freedom, all the wave power can be extracted (Mei 1976). In this paper the first structural design criteria's for a WEC were presented, however only regular waves were considered for the power extraction calculation.

Budal et al. (Budal 1975) published results of model experiments of a phase controlled point absorber operating in heave only. One of the first latching control strategies was applied at this time.

CHAPTER 2
Description of the numerical model

Contents:

- Laboratory scale model of the Wavestar device.
- Nonlinear hydrostatic restoring moment.
- Truncation of the convolution integral.
- Rational approximation of the radiation force.

2.1 The dynamic model

The equation of motion is obtained by formulating the momentum equilibrium condition around the fixed point A, see Fig. 2.2.

$$J\,\ddot{\theta}(t) + R\,\theta(t) + \int_{-\infty}^{t} h_{r\dot{\theta}}(t-\tau)\dot{\theta}(\tau)\,d\tau = M_e(t) - M_c(t) \tag{2.1}$$

$$J = j + j_h^{\infty} \tag{2.2}$$

Pitch $\theta(t)$ is the corresponding degree of freedom around the bearing. The mass moment of inertia around the fixed point of the float mass and the arm is denoted as j , j_h^{∞} is the added mass at infinitely high frequencies, $h_{r\dot{\theta}}(t)$ is the impulse response function of the radiation force, R is the hydrostatic stiffness coefficient, $M_c(t)$ represents the control moment from the power take-off system, $M_e(t)$ is the excitation moment. In the following experiment, two-dimensional irregular waves are considered, propagating in the positive y-direction relative to (x, y, z)-coordinate system defined in Fig. 2.2.

In order to calculate the exact wave excitation moment we would need to brake down the component $M_e(t)$ into the Froude-Krylov and the diffraction force. The equation of motion is reformulated:

$$(j + j_h^\infty)\ddot{\theta}(t) + M_g + M_{rad} = M_{FK} + M_d + M_B \tag{2.3}$$

- M_g: Moment due to gravity
- M_{rad} : Radiation moment
- M_d: Diffraction moment
- M_B: Buoyancy moment
- $(j + j_h^\infty)$: Inertia moment

For a quasi static structural response analysis it is advantageous to reformulate the equation differently.

$$\underbrace{(j + j_h^\infty)}_{\text{Angular acceleration}} \ddot{\theta} = \underbrace{M_{FK} + M_d + M_B - M_g - M_{rad}}_{\sum M_i} \tag{2.4}$$

The force components are summarized as follows, (Næsee 2012):

1. Froude-Krylov force: Pressure effect due to the undisturbed incident waves.

2. Diffraction force: Pressure effect due to the presence of the structure.

3. Hydrodynamic added mass and damping force: Pressure effects due to motion of structural components in an ideal fluid.

4. Viscous drag force: Pressure effects due to relative velocity between water particles and structural components.

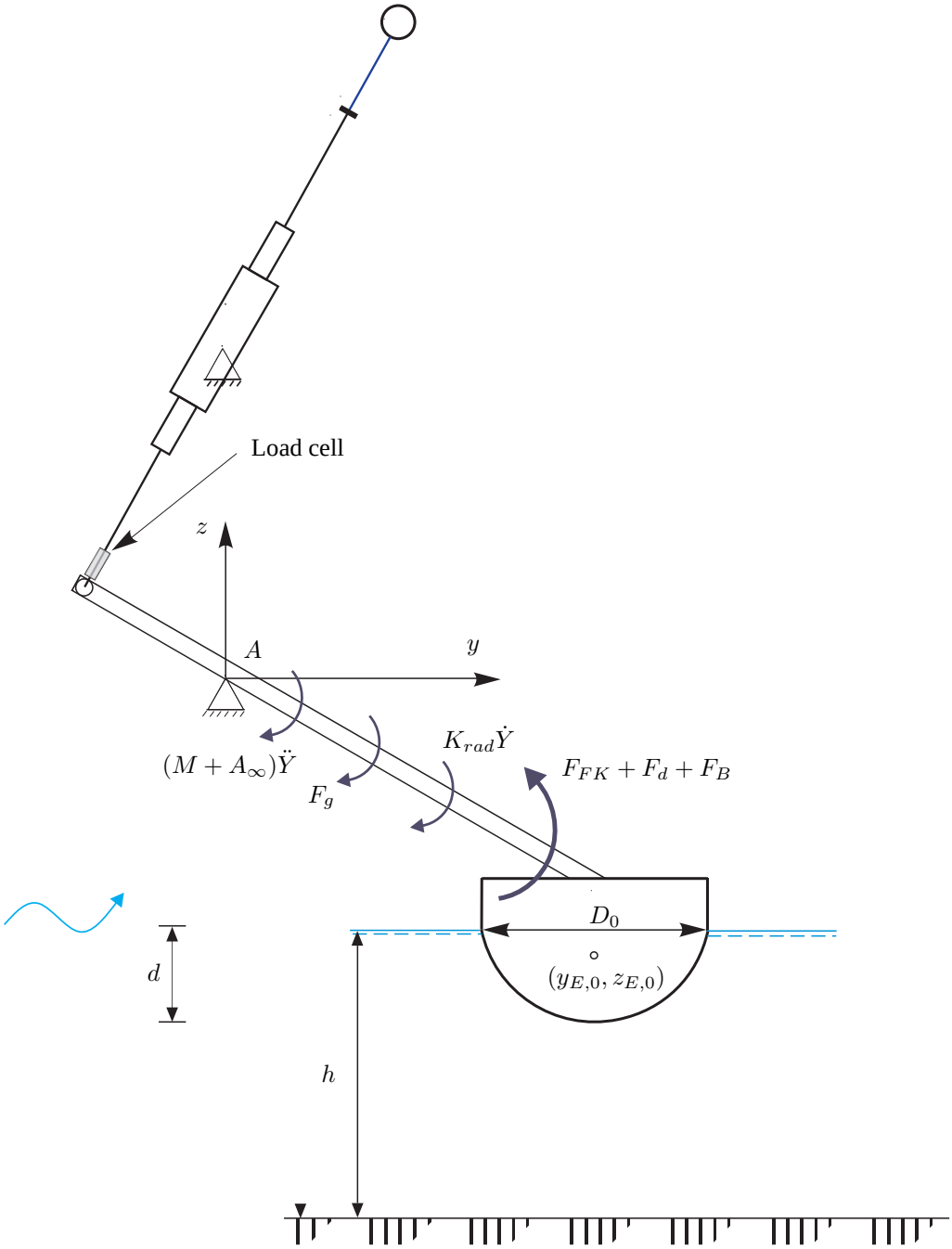

Figure 2.1 Definition of the laboratory model (1:20) representing the Wavestar prototype model in Hanstholm, static referential state, $y_{E,0}$ and $z_{E,0}$: center of buoyancy.

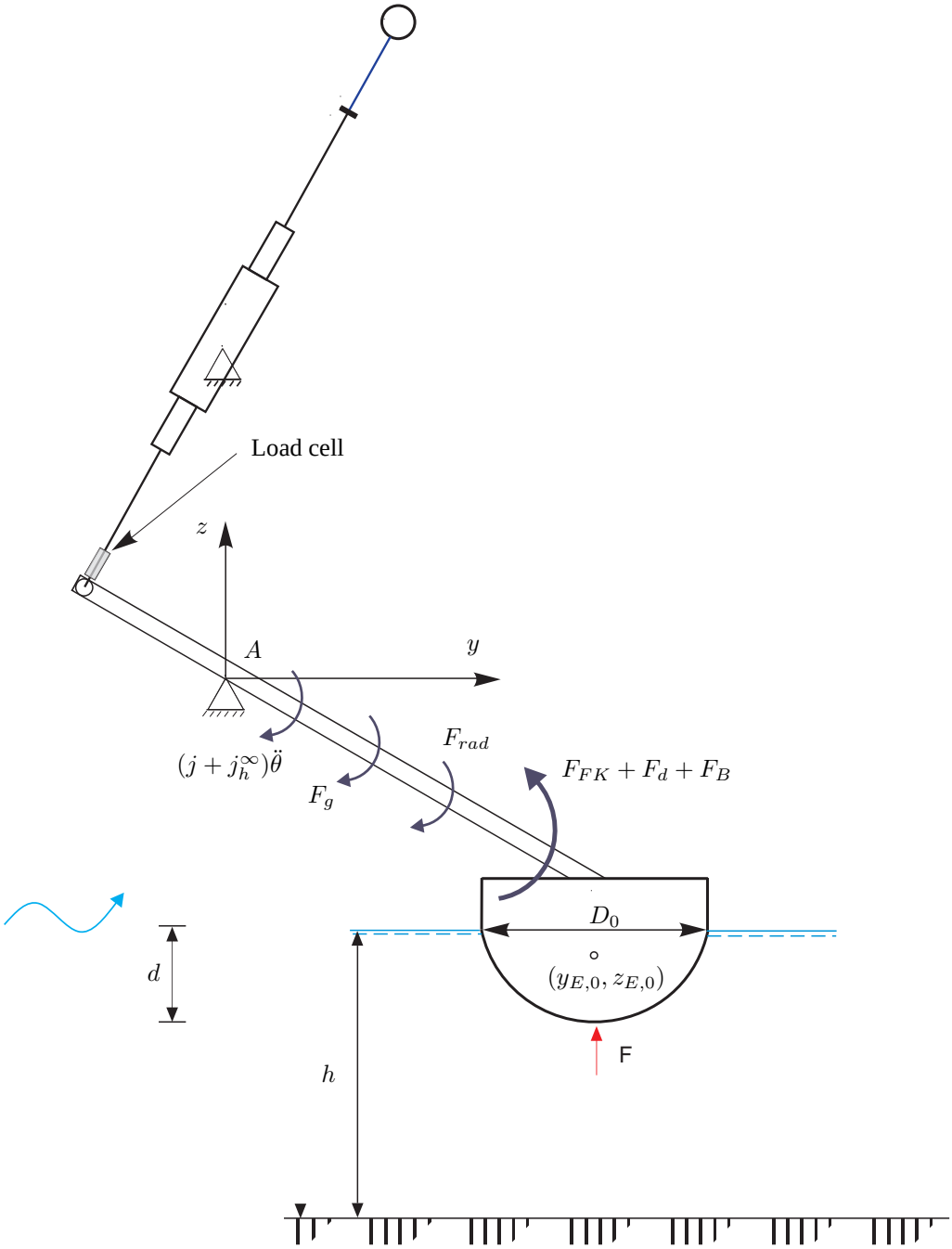

Figure 2.2 Definition of the laboratory model (1:20) representing the Wavestar prototype model in Hanstholm, static referential state, $y_{E,0}$ and $z_{E,0}$: center of buoyancy.

2.1.1 Nonlinear hydrostatic restoring moment

The change of the hydrostatic pressure at each instantaneous position of the float below the water plane can be taken into account by integrating the hydrostatic pressure over the instantaneous wetted surface. Thus the hydrostatic restoring moment can be formulated in a more generalized form as follows:

$$R = -\rho g \iint_{S_B(t)} \mathbf{n} \cdot z \cdot dS(t) \tag{2.5}$$

The time domain simulations in this paper include the nonlinear hydrostatic moment R given in Eqn. (2.5). Static tests have been carried out in order to experimentally describe the hydrostatic moment acting on the float. The change of the wetted surface can be observed when the float is successively dipping into the water. Figure 2.3 shows the experimental results. The time domain model considers a trilinear piecewise approximation of the hydrostatic behavior depicted in the dashed black curve in the Figure 2.3. The relative position of the float is calculated by the difference of the undisturbed incident wave elevation and the rotational displacement at the instantaneous time step.

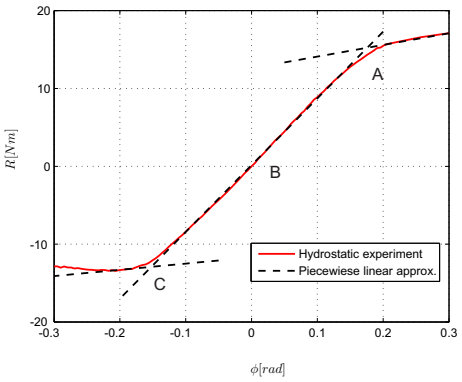

Figure 2.3 The piecewise linear approximation of the hydrostatic restoring moment is shown in the black dashed line, the red curve shows the results from the experiments.

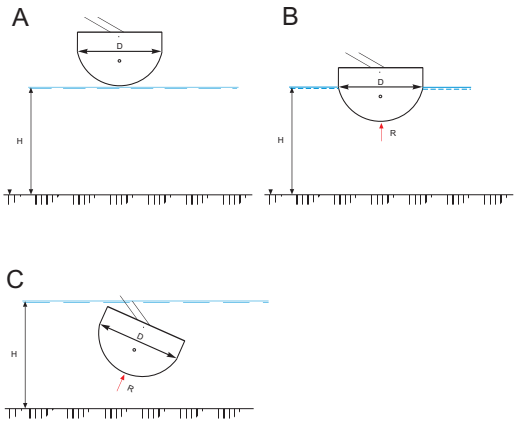

Figure 2.4 Point A: the float is out of the water no hydrostatic force is acting on the sphere, Point B: the float is in its static equilibrium position the hydrostatic restoring moment increases linearly with degree of submergence, Point C: the float is fully submerged the weight of the overtopped water reduces the "spring effect" of the buoyancy force.

2.1.2 Impulse response function of the radiation force

The impulse response function of the radiation force can be seen as the system identity. If we know the response to an impulse, then we know the response to any excitation by convolution with the impulse response function. The basic work for this formulation of the problem was laid by W.E. Cummins (Cummins 1962). In Figure 2.5 two different radiation impulse response functions are shown. The blue line represents the solution based on a high frequency approximation, whereas the red line is based on a unmodified FFT analysis, i.e. no approximation of the high frequencies. The "cut-off" frequency for the blue curve can be observed at a frequency of 0.5 Hz, $(T \cong 2.0sec)$. For the first case the initial damping value $h_{r\dot{\theta}}(t=0)$ is slightly higher than for the second method, however for higher periods it seems to be the opposite case. The MATLAB command is [y,x,t]=impulse[A,B,C,D,iu].

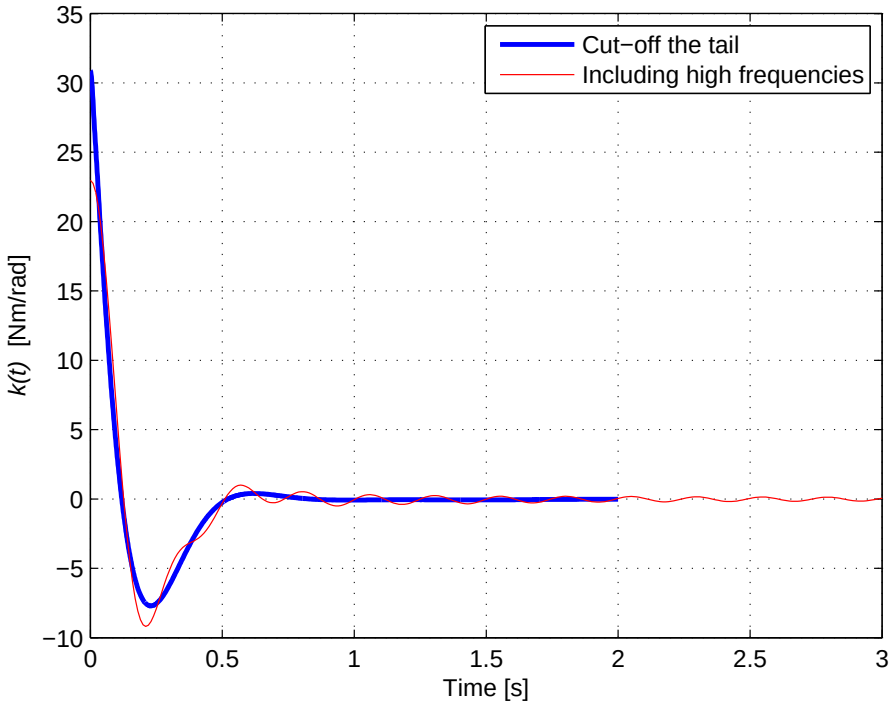

Figure 2.5 The radiation impulse response function $h_{r\dot{\theta}}(t)$. The blue line represents the solution based on a high frequency approximation whereas the red line is based on a unmodified FFT analysis, i.e. no approximation of high frequencies.

2.1.3 Rational Approximation of the radiation force

The radiation moment $M_r(t)$ is given as:

$$M_r(t) = -j_h^{\infty}\ddot{\theta}(t) - M_{r,0}(t) \tag{2.6}$$

where

$$M_{r,0}(t) = \int_0^t h_{r\dot{\theta}}(t-\tau)\dot{\theta}(\tau)d\tau \tag{2.7}$$

The idea in this section is to replace the convolution integral by an equivalent system of coupled first order differential equations, which are solved numerically along with the equations of motion of the absorber. The method is based on an initial replacement of the actual frequency response function $H_{r\dot{\theta}}(\omega)$ with an approximating *rational function* $\tilde{H}_{r\dot{\theta}}(\omega)$ given in the form

$$H_{r\dot{\phi}_4}(s) = B(\omega) + i\omega(A(\omega) - A^{\infty}) \tag{2.8}$$

$$\tilde{H}_{r\dot{\phi}_4}(s) = \frac{P(s)}{Q(s)} = \frac{p_0 s^m + p_1 s^{m-1} + ... + p_{m-1}s + p_m}{s^n + q_1 s^{n-1} + ... + q_{n-1}s + q_n} \tag{2.9}$$

The unknowns are the coefficients of polynomials P and Q. The parameters p_0,p_1,...,p_{m-1},p_m and q_1,...,q_{n-1} q_n define the *poles* and the *zeros* of the rational approximation and are all real. The order of the filter as given by the pair (n,m) may be chosen freely with the only restriction that $m \leq n$, and that all poles have negative real part, i.e.

$$Re(p_j) < 0, \qquad j = 1, ..., n \tag{2.10}$$

Eqn. (2.10) ensures that the filter is *stable* and *causal*. Correspondingly, the indicated approach only applies to frequency response functions. A rational causal approximation for $H_{r\dot{\theta}}$ can be obtained by the *MATLAB control toolbox* (Matlab 2012) or the *MSS FDI toolbox* (Perez and Fossen 2009). Next, the convolution integral $M_{r,0}(t)$ is obtained as output of the following system of differential equations

$$M_{r,0}(t) = p_0\frac{d^m y}{dt^m} + p_1\frac{d^{m-1}y}{dt^{m-1}} + \cdots + p_{m-1}\frac{dy}{dt} + p_m y \tag{2.11}$$

$$\frac{d^n y}{dt^n} + q_1\frac{d^{n-1}y}{dt^{n-1}} + \cdots + q_{n-1}\frac{dy}{dt} + q_n y = \dot{\theta}(t) \tag{2.12}$$

where $y(t)$ is an auxiliary variable, which cannot be related with any physical interpretation. Eqn. (2.12) may be written in the following state vector form

$$\dot{\mathbf{z}}_r(t) = \mathbf{A}_r\,\mathbf{z}_r(t) + \mathbf{b}_r\dot{\theta}(t) \tag{2.13}$$

where:

$$\mathbf{z}_r(t) = \begin{bmatrix} y(t) \\ \frac{d}{dt}y(t) \\ \frac{d^2}{dt^2}y(t) \\ \vdots \\ \frac{d^{n-2}}{dt^{n-2}}y(t) \\ \frac{d^{n-1}}{dt^{n-1}}y(t) \end{bmatrix} \quad , \quad \mathbf{b}_r = \begin{bmatrix} 0 \\ 0 \\ 0 \\ \vdots \\ 0 \\ 1 \end{bmatrix} \tag{2.14}$$

$$\mathbf{A}_r = \begin{bmatrix} 0 & 1 & 0 & \cdots & 0 & 0 \\ 0 & 0 & 1 & \cdots & 0 & 0 \\ \vdots & \vdots & \vdots & \ddots & \vdots & \vdots \\ 0 & 0 & 0 & \cdots & 0 & 1 \\ -q_n & -q_{n-1} & -q_{n-2} & \cdots & -q_2 & -q_1 \end{bmatrix} \tag{2.15}$$

Similarly, Eqn.(2.7) may be written on the vector form

$$M_{r,0}(t) = \mathbf{p}_r \, \mathbf{z}_r(t) \tag{2.16}$$

$$\mathbf{p_r} = \begin{bmatrix} p_m & p_{m-1} & \cdots & p_1 & p_0 & 0 & \cdots & 0 \end{bmatrix} \tag{2.17}$$

By rearranging the equations above the equation of motion can now be rewritten in a state space model as follows:

$$\frac{d}{dt}\mathbf{z}(t) = \mathbf{A}\mathbf{z}(t) + \begin{bmatrix} 0 \\ \frac{1}{J} \\ \mathbf{0} \end{bmatrix} \int_{-\infty}^{\infty} h_{r\dot{\theta}}(t-\tau)\eta(\tau)d\tau \tag{2.18}$$

where

$$\mathbf{z}(t) = \begin{bmatrix} \theta(t) \\ \dot{\theta}(t) \\ \mathbf{z}_r(t) \end{bmatrix} \tag{2.19}$$

$$\mathbf{A} = \begin{bmatrix} 0 & 1 & \mathbf{0} \\ -\frac{R}{J} & 0 & -\frac{1}{J}\mathbf{p}_r \\ \mathbf{0} & \mathbf{b}_r & \mathbf{A}_r \end{bmatrix} \tag{2.20}$$

In Eqn.(2.18) the control moment $M_c(t)$ has been omitted. The method has been illustrated below for the absorber defined in Fig. 2.2 with the numerical values in Tab. 3.1, using the relatively low order filter $(m, n) = (4, 5)$. In Fig. 2.6 and Fig. 2.6 the resulting frequency response functions has been compared with the corresponding target frequency response function calculated by the BEM program WAMIT, (WAMIT 2012).

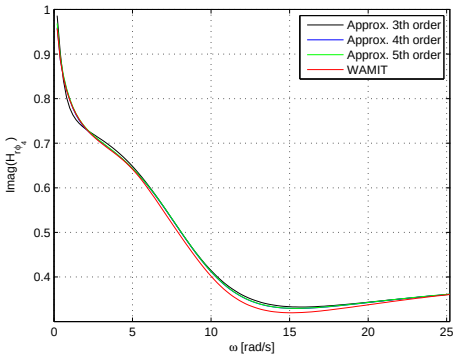

Figure 2.6 Imaginary part of the frequency response curve.

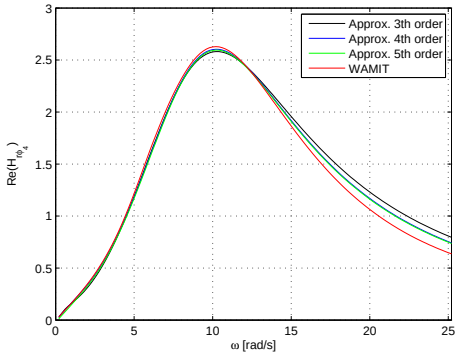

Figure 2.7 Piecewise linear approximation of the nonlinear hydrostatic restoring moment.

2.2 Solving the dynamic model

The time-domain analysis of a floating structure involves the calculation of a convolution integral between the impulse response function of the radiation force and the unknown body velocity due to an external force. The convolution integral can be seen as a memory effect where the system response in the past affects the response in the future. Two different time-domain models will be presented.
The first one is based on a discretization of the convolution integral. The calculation of the convolution integral is performed at each time step regardless of the chosen numerical scheme.
In the second model the convolution integral is replaced by a system of linear ordinary differential equations. The formulation of the state-space model is advantageous regarding the computational effort and the robustness of the solver. Another important feature is the linear-time invariance of the system. In a next step the influence of the nonlinear hydrostatic behavior of the float is investigated by using a simplified formulation.

2.2.1 Truncation of the convolution integral

Let us consider the following dynamic equilibrium equation of the WEC device shown in Fig. 2.2.

$$(J + j_h^{\infty})\ddot{\theta}(t) + \int_0^t h_{r\dot{\theta}}(t-\tau)\dot{\theta}(\tau)d\tau + R\theta(t) + c_{pto}\dot{\theta}(t) = \int_{-\infty}^{\infty} h_{e\eta}(t-\tau)\eta(t)d\tau \qquad (2.21)$$

The convolution integral in Eqn. 2.21 can be expressed by means of a sum:

$$\int_0^t h_{r\dot{\theta}}(t-\tau)\dot{\theta}(\tau)d\tau = \Delta t \sum_{\tau=0}^{t} h_{r\dot{\theta}}(t-\tau)\dot{\theta}(\tau) \tag{2.22}$$

Expanding the sum in Eqn. 2.22, we get the following expression:

$$\Delta t \sum_{\tau=0}^{t} h_{r\dot{\theta}}(t-\tau)\dot{\theta}(\tau) = \Delta t[h_{r\dot{\theta}}(t)\dot{\theta}(0) + h_{r\dot{\theta}}(t-1)\dot{\theta}(1) + ... + h_{r\dot{\theta}}(0)\dot{\theta}(t)] \tag{2.23}$$

The equation of motion can then be written as follows:

$$(J+j_h^{\infty})\ddot{\theta}(t)+h_{r\dot{\theta}}(0)\dot{\theta}(t)+R\theta(t)+c^{pto}\dot{\theta}(t) = \int_{-\infty}^{\infty} h_{e\eta}(t-\tau)\eta(t)d\tau - \int_0^{t^-} h_{r\dot{\theta}}(t-\tau)\dot{\theta}(\tau)d\tau \tag{2.24}$$

The numerical integration of Eqn. 2.24 only requires the calculation of the integral at the preceding time-steps and can therefore be considered as a known quantity. A fourth order Runge Kutta scheme with a constant time step Δt has been used to evaluate the linear equation of motion given in Eqn. 2.24. Drawbacks of this method are *i)* time consuming *ii)* the convolution integral needs to be calculated at each time step *iii)* the impulse response function needs to be interpolated with the same Δt as the time integration, which is not very convenient. The results are shown in the last page of this chapter. Fairly good agreement can be observed when comparing the numerical discretization of the convolution integral with an analytical calculation for regular waves, i.e. when a constant damping coefficient can be assumed.

Comparison between the two different integration techniques are presented in the workshop paper of the IWWWFB workshop held in 2012 in Copenhagen, see appendix A.

2.2.2 State space model

The state space approximation of the convolution integral may be directly calculated from the frequency domain coefficients. The convolution integral is expressed as follows:

$$\int_0^t h_{r\dot{\theta}}(t-\tau)\dot{\theta}(\tau)d\tau = g(I) \tag{2.25}$$

where $g(I)$ are the new state variables.

$$\dot{I} = h(I,\dot{\theta}) \tag{2.26}$$

The approximation of the convolution integral using the coefficients of the polynomial P(s), introduced in Eqn. 2.9, gives us then:

$$\int_0^t h_{r\dot{\theta}}(t-\tau)\dot{\theta}(\tau)d\tau \approx \left[\begin{array}{cccc} p_0 & p_1 & \ldots & p_{n-1} \end{array}\right] I(t) \tag{2.27}$$

where the derivatives of the new states are given as:

$$\dot{I}(t) = \left[\begin{array}{cccc} -q_1 & -q_2 & -q_3 & q_n \\ 1 & 0 & 0 & 0 \\ 0 & 1 & 0 & 0 \\ 0 & 0 & 1 & 0 \end{array}\right] I(t) + \left[\begin{array}{c} 1 \\ 0 \\ 0 \\ 0 \end{array}\right] \dot{\theta}(t) \tag{2.28}$$

Having defined the new state vector $\dot{I}_i$, we assemble and get:

$$Y = \left(\begin{array}{c} \theta \\ \dot{\theta} \\ I_i \end{array}\right) \tag{2.29}$$

The equation of motion is then rewritten in an ODE of first order

$$\dot{Y} = F(t, I) \tag{2.30}$$

$$F(t,I) = \left(\begin{array}{c} \dot{\theta} \\ (j+j_\infty)^{-1}(M_{ex} - \int_0^t h_{r\dot{\theta}}(t-\tau)\dot{\theta}(\tau)d\tau - R\theta + F_{drag} + F_{PTO}) \\ \dot{I}_i \end{array}\right) \tag{2.31}$$

The state space form of the equations above may be formulated as:

$$\dot{x} = Ax + Bu \tag{2.32}$$

$$y = Cx + Du \tag{2.33}$$

Assuming the geometry in Fig. 2.2 and based on the hydrodynamic coefficients shown in Fig. 2.6 and Fig. 2.7 we get the following numerical values by using the inbuild invfreqs function in Matlab.

$$\dot{x} = Ax + B\dot{\theta}(t) = \dot{I}(t) = \left[\begin{array}{cccc} -14.69 & -124.78 & -124.79 & -14.56 \\ 1 & 0 & 0 & 0 \\ 0 & 1 & 0 & 0 \\ 0 & 0 & 1 & 0 \end{array}\right] I(t) + \left[\begin{array}{c} 1 \\ 0 \\ 0 \\ 0 \end{array}\right] \dot{\theta}(t) \tag{2.34}$$

$$y = \int_0^t h_{r\dot{\theta}}(t-\tau)\dot{\theta}(\tau)d\tau \approx Cx + D\dot{\theta}(t) = \left[\begin{array}{cccc} 35.13 & 60.57 & 10.71 & 0 \end{array}\right] I(t) + 0\dot{\theta}(t) \tag{2.35}$$

The above equations are solved in MATLAB. The Figures 2.8 to 2.11 show the comparison between the convolution of the impulse response function with a sinusoidal function and the approximation of the convolution integral with the state space model presented in Eqn. 2.34 and 2.35. The MATLAB comment $conv(K, \dot{X}(t)) \cdot \Delta t$ is used. Figures 2.12 and 2.13 compare the two methods i.e. the truncation and the approximation of the convolution integral for two different damping coefficients.

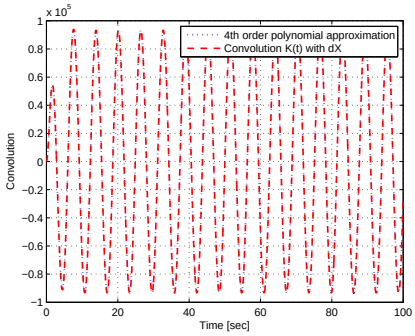

Figure 2.8 Convolution of the impulse response function with a $sin(t)$ signal

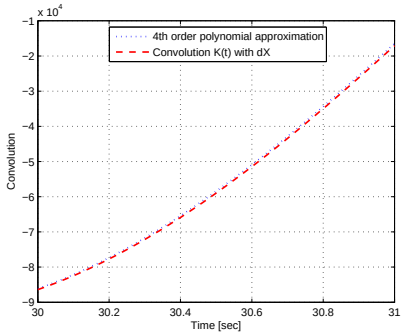

Figure 2.9 Convolution of the impulse response function with a $sin(t)$ signal - zoom

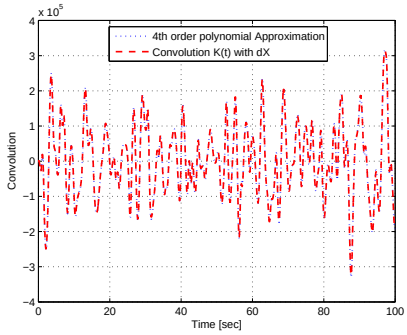

Figure 2.10 Convolution of the impulse response function with a zero mean random noise signal

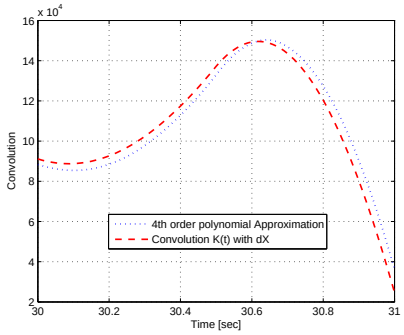

Figure 2.11 Convolution of the impulse response function with a zero mean random noise signal

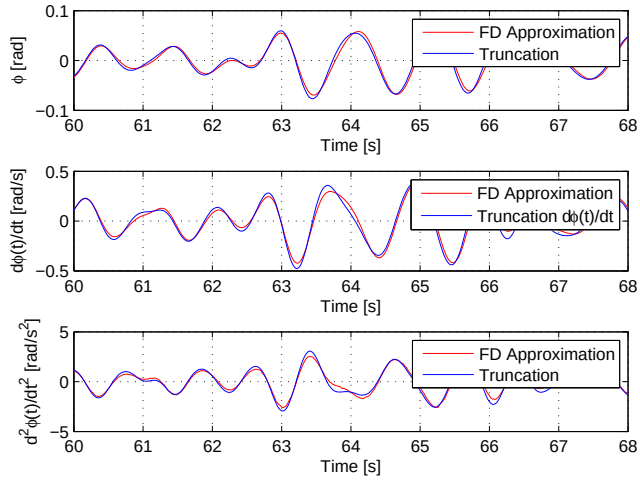

Figure 2.12 Comparison between direct numerical integration and a state-space approximation of the radiation kernel, $c_{pto} = 4Nm/rad/s$

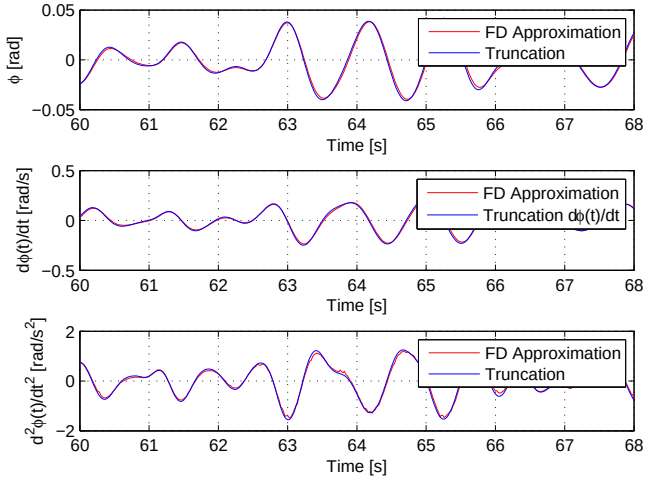

Figure 2.13 Comparison between direct numerical integration and a state-space approximation of the radiation kernel, $c_{pto} = 12Nm/rad/s$

The comparison between the experiments and the numerical calculation has been presented in a OMAE conference in 2012 in Rio de Janeiro, see appendix B. The experimental results will be discussed in chapter 4. The comparison is carried out for the passive damped case.

2.2.3 State space model of the wave excitation force

The block diagram in Fig. 2.14 shows the procedure which is applied hereafter in order to calculate the wave excitation moment in the time domain. $W(t)$ is a zero mean random process known as withe noise, $H_{\eta\omega}(\omega)$ is the frequency response function of the wave spectrum, $\eta(t)$ corresponds to the wave elevation, $h_{e\eta}(t)$ is the impulse response function of the wave excitation moment and $M_e(t)$ is the wave excitation moment.

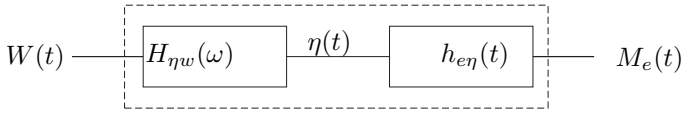

Figure 2.14 Block diagram for the calculation of the excitation force in the time domain

The wave excitation moment is expressed as follows:

$$M_e(t) = \int_{-\infty}^{\infty} h_{e\eta}(t-\eta)\eta(\tau)d\tau \tag{2.36}$$

The related frequency response function is:

$$H_{e\eta}(\omega) = \int_{-\infty}^{\infty} e^{-i\omega t} h_{e\eta}(t)dt \tag{2.37}$$

Furthermore the following relation holds:

$$M_e(\omega) = |M_e|e^{-i\alpha} = H_{e\eta}(\omega)\eta(\omega) \tag{2.38}$$

$|M_e|$ is the modulus (amplitude) and α is the negative argument of the fourier transformation and $\eta(\omega)$ is the fourier transformation of the sea-surface elevation $\eta(t)$.

The real and imaginary part of the frequency response function are shown in Fig. 2.15 and Fig. 2.16. The corresponding impulse response function (IRF) is shown in Fig. 2.17. In a next step we split the IRF function into a causal and non-causal part respectively. The fourier transformations of Eqn. 2.39 and Eqn. 2.39 are shown in Fig. 2.18 and Fig. 2.19 and are compared with the original frequency response function calculated with a Boundary Element method (BEM). From Fig. 2.19 one can see the difference between the full frequency response function based on the BEM calculation and only the causal part of it. It can be concluded that, for the calculation of the wave excitation force based on time series of the wave elevation, cf. Eqn. 2.36 one has to convolute with the non-causal impulse response function rather than only the causal part i.e. red curve in Fig. 2.17.

$$H^{+}_{e\eta}(\omega) = \int_{0}^{\infty} e^{-i\omega t} h^{+}_{e\eta}(t)dt \tag{2.41}$$

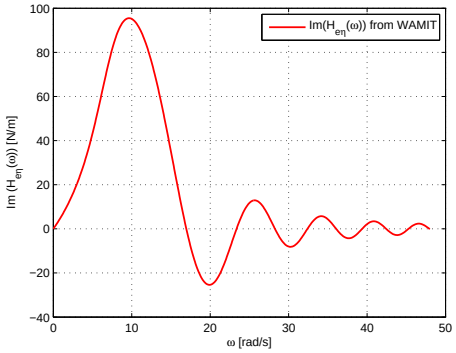

Figure 2.15 Real part, frequency response function of the excitation force Re$(H_{e\eta})(\omega))$

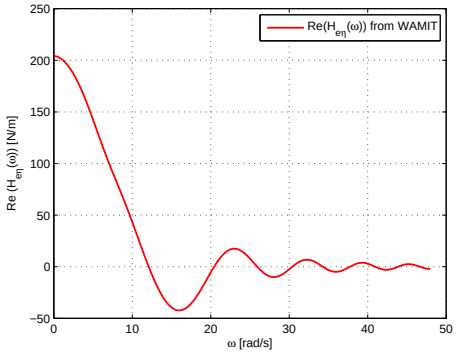

Figure 2.16 Imaginary part, frequency response function of the excitation force Im$((H_{e\eta})(\omega))$

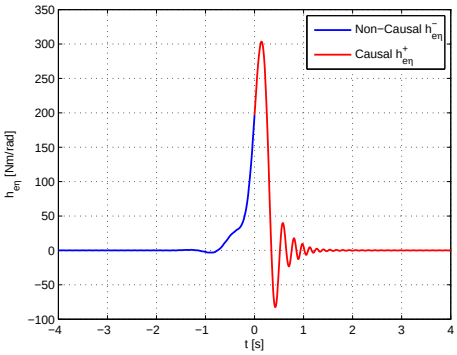

Figure 2.17 Impulse response function of the excitation force, $h_{e\eta}(t)$, blue curve: non-causal, red curve: causal part

$$h_{e\eta}^{-} = \begin{cases} h_{e\eta}(-t) & \text{if } t \leq 0, \\ 0 & \text{if } t > 0. \end{cases} \tag{2.39}$$

$$h_{e\eta}^{+} = \begin{cases} h_{e\eta}(t) & \text{if } t \geq 0, \\ 0 & \text{if } t < 0. \end{cases} \tag{2.40}$$

$$H_{e\eta}^{-}(\omega) = \int_0^\infty e^{-i\omega t} h_{e\eta}^{-}(t) dt \tag{2.42}$$

Random phase method

The wave spectrum is divided into N parts by the frequency band width Δf. This means that the irregular wave is composed of N linear waves.

The variance of each linear wave is:

$$S_\eta(f_i)\Delta f = \frac{1}{2} a_i^2, \qquad i = 1, 2, ..., N \tag{2.43}$$

The amplitude is:

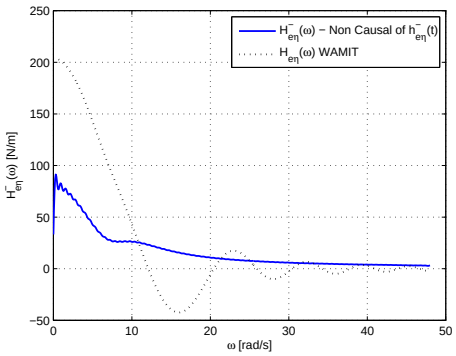

Figure 2.18 Non Causal-part frequency response function $H^{-}_{e\eta}(\omega)$

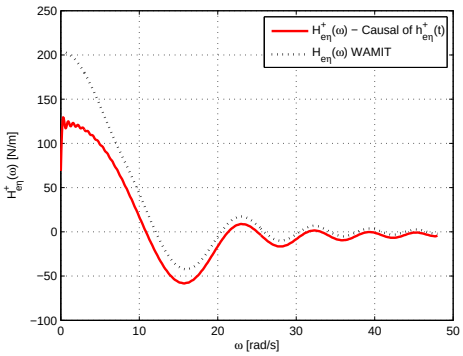

Figure 2.19 Causal-part frequency response function $H^{+}_{e\eta}(\omega)$

$$a_i = \sqrt{2S_\eta(f_i)\Delta f}, \qquad i = 1, 2, ..., N \tag{2.44}$$

and the angular frequency is:

$$\omega_i = \frac{2\pi}{T_i} = 2\pi f_i, \qquad i = 1, 2, ..., N \tag{2.45}$$

The wave elevation is then a discrete sum over all the angular frequencies and amplitudes:

$$\eta(t) = \sum_{i=1}^{N} \eta_i(t) = \sum_{i=1}^{N} a_i cos(\omega_i t + \delta_i)$$

2.3 Control moment

The control force moment $M_c(t)$ is work conjugated to the contraction of the piston arm BC, see Fig. 2.2 and is used to control the motion of the WEC in a way that a maximum power outtake is obtained. The following parameterized feed-back control law is assumed, (S.R.K. Nielsen 2012):

$$M_c(t) = m_c\ddot{\theta}(t) + c_c\dot{\theta}(t) + k_c\theta(t) + b_c \int_{-\infty}^{\infty} h_{c\dot{\theta}}(t-\tau)\dot{\theta}(\tau)\, d\tau \tag{2.46}$$

m_c denotes the gain factor for the control force component proportional to the acceleration, c_c signifies the gain factor for the control force component proportional to the velocity and k_c denotes the gain factor for the control force component proportional to the rotational displacement θ, b_c is a number between zero and one. In control theory the force components proportional to the displacement and the velocity are referred to as proportional and derivative control, respectively. m_c and k_c may attain positive as well as negative values. c_c is always positive in the present application. The last term in Eqn. 2.46 represents the weighted influence on the control force of previous and future velocities. Accordingly, the impulse response function is not causal.

2.3.1 Optimal control of a linear point absorber

The following derivations and equations are taken from the script (Nielsen 2012). The material was presented during a PhD course which was held at Aalborg University in 2011. The goal was to highlight the application of stochastic methods to define the optimal control parameters of a wave energy point absorber in irregular waves. With this approach the optimal damping coefficient is calculated to be a function of the auto-correlation coefficient of the given wave excitation process. An analytical expression for the optimal damping coefficient will be presented. It will be shown that, the closer the oscillator moves into resonance with the incoming waves the smaller becomes the ideal damping coefficient. This means that the system experiences higher oscillations therefore also higher inertial forces at a higher energy absorbtion rate. The question which urges from this observation is: Are there control parameters which can also reduce the structural forces and still keep the energy production at the most highest level ? To answer this question the model must be extended and ideally an adequate fatigue model has to be introduced to account for the effect of structural loads in function of the control loads.

The dynamic response of the wave energy converter in presence of waves is assumed to be a stationary Gaussian random process with zero mean value. The optimal control parameters are depending on the frequency spectrum in the waves. Hence for irregular waves the control becomes difficult to establish and often simplified assumptions have to be made. The first unrealistic assumption is connected with the oscillator. In order to have an optimal controlled power absorber the velocity of the oscillator has to be in phase with the incoming wave excitation force. Assuming that this condition can be achieved physically by feeding enough power into the system and hoping that there is more power to be harvested, the control law can be formulated as follows:

$$M_{ex}(t) = 2c_c\dot{\theta}(t) \tag{2.47}$$

The control law in Eq. (2.47) is theoretical and has no physical meaning unless constraints are implemented in the control algorithm. Furthermore an important issue is related with the efficiency factors of the generator in both directions. In the present case the power is absorbed solely by the damping coefficient c_c. The following calculations are based on the assumptions that the oscillator is in resonance with the incoming wave frequency by a wave to wave resolution and the input and output time series are two stationary Gaussian processes. The dynamic response is expressed in function of the wave excitation force assuming the resonance condition:

$$\dot{\Theta}(t) = \frac{1}{2c_c}M_{ex}(t) \quad , \quad \Theta(t) = \frac{1}{2c_c}\int_{-\infty}^{t} M_{ex}(\tau)\,d\tau \tag{2.48}$$

The instantaneous power is given as:

$$\overline{P_c(t)} = E[\dot{\Theta}(t)M_c(t)] \tag{2.49}$$

where $E[]$ is the mathematical expectation of the random process in the square brackets. The response of the system is assumed to be stochastic so is the control moment, (S.R.K. Nielsen 2012):

$$M_c(t) = M\ddot{\Theta}(t) + c_c\dot{\Theta}(t) + K\Theta(t) + \int_{-\infty}^{\infty} h_{c\dot{\Theta}}(t-\tau)\dot{\Theta}(\tau)d\tau \tag{2.50}$$

In order to fulfill the condition given in Eq. 2.47 the coefficients in equation Eq. 2.50 have to be chosen accordingly:

$$M = -J \tag{2.51}$$
$$K = -k_c \tag{2.52}$$
$$h_{c\dot{\Theta}}(t-\tau) = -h_{r\dot{\Theta}}(t-\tau) \tag{2.53}$$

By inserting Eq. 2.50 into Eq. 2.49 we get

$$< P_c(t) >= E\big[\dot{\Theta}(t)M_c(t)\big] = -ME\big[\dot{\Theta}(t)\ddot{\Theta}(t)\big] + c_cE\big[\dot{\Theta}^2(t)\big] \tag{2.54}$$
$$-KE\big[\dot{\Theta}(t)\Theta(t)\big] - \int_{-\infty}^{t} h_{r\dot{\theta}}(t-\tau)E\big[\dot{\Theta}(t)\dot{\Theta}(\tau)\big]\,d\tau \tag{2.55}$$

The variables $\Theta(t)$, $\dot{\Theta}(t)$ and $\ddot{\Theta}(t)$ are statistically independent random variables with $E[\Theta(t)] = E[\dot{\Theta}(t)] = E[\ddot{\Theta}(t)] = 0$ (zero mean). According to the properties of the mean value operator of two independent random variables X and Y, (Ochi 1990), $E[XY] = E[X]E[Y]$, the first terms in Eq. (2.54) and Eq. (2.54) are vanishing, i.e. $E[\dot{\Theta}(t)\ddot{\Theta}(t)] = 0$ and $E[\dot{\Theta}(t)\Theta(t)] = 0$.

The expression $E[\dot{\Theta}(t)^2]$ is actually the variance of the random variable $\dot{\Theta}(t)$ and is denoted as $\sigma^2_{\dot{\Theta}\dot{\Theta}}$. Note that the mean value of the process $\dot{\Theta}^2$ is zero due to the fact that in presence of no waves the float is in its static equilibrium position, and hence the movements are zero. The variance is defined as the second order moment of the random variable x, i.e. $E[(X-\mu)^2] = \sigma^2_{XX}$.

The last term in Eq. (2.54) is known as the autocovariance function. Normally the autocovariance function is evaluated by the time average of a signal and by its time shift of τ. The definition is given by $R_{XX}(\tau) = E[X(t)X(t+\tau)]$. The convolution in Eq. (2.54) is a time shift in the past, i.e. it is also known as the memory effect of the system because it does account the behavior in the previous time step. In our case we can write, $R_{XX}(\tau - t) = E[X(t)X(\tau)]$ and therefore $\kappa_{\dot{\Theta}\dot{\Theta}}(t-\tau) = E[\dot{\Theta}(t)\dot{\Theta}(\tau)]$. Note that R_{XX} is an even function, i.e. $R_{XX}(-\tau) = R_{XX}(\tau)$. Another important characteristic is the amplitude of the auto-covariance function for $\tau = 0$, i.e. $R_{XX}(0) = E[(X(t)^2)] = \sigma^2_{XX}$.

Summarized the above and applied to our case, we can write:

$$\begin{aligned} E\big[\dot{\Theta}(t)\dot{\Theta}(t)\big] &= E\big[\frac{1}{4c_c^2}M_{ex}(t)M_{ex}(t)\big] = \frac{1}{4c_c^2}\,\sigma^2_{M_{ex}M_{ex}} \\ E\big[\dot{\Theta}(t)\dot{\Theta}(\tau)\big] &= \kappa_{\dot{\Theta}\dot{\Theta}}(\tau-t) = \kappa_{\dot{\Theta}\dot{\Theta}}(t-\tau) = \frac{1}{4c_c^2}\,\kappa_{M_{ex}M_{ex}}(t-\tau) \end{aligned} \tag{2.56}$$

It is hereby shown that based on the stationarity assumption of the instantaneous power we can express the process by two well known quantities namely by the variance and the auto-covariance function of the stochastic process. In order to continue we are going to introduce a few more useful relationships which are common in a stochastic process analysis.
The variance σ_{XX}^2 of a stochastic process can be calculated by setting $\tau = 0$ for the auto-covariance function or by simply integrating the energy spectrum $S_{XX}(\omega)$ in the frequency ω domain. Thus we write:

$$\sigma_{XX}^2 = R_{XX}(0) = \int_{-\infty}^{\infty} S_{XX}(\omega) d\omega \tag{2.57}$$

$S_{XX}(\omega)$ can therefore be seen as a distribution of variances over the frequency spectrum. In our case the energy spectrum is expressed by the frequency response function of the wave excitation moment, i.e.:

$$S_{M_e M_e}(\omega) = |H_{e\eta}(\omega)|^2 \, S_{\eta\eta}(\omega) \tag{2.58}$$

where $H_{e\eta}(\omega)$ is the frequency response function of the excitation force. This function is complex and is calculated by a BEM (Boundary Element Method) potential solver, like WAMIT or AQWA. The function consists of an amplitude and a phase. Note that with Eq. (2.58) only the amplitude information is kept whereas the phase information is "lost". In Eq. (2.58) the double sided spectrum is used, however negative frequencies have relatively low physical meaning.
The relationship between the auto-covariance function $R_{XX}(\tau)$ and the energy spectrum $S_{XX}(\omega)$ is widely known as the Wiener-Khintchine Theorem and defined as follows:

$$S_{XX}(\omega) = \frac{1}{\pi} \int_{-\infty}^{\infty} R_{XX}(\tau) e^{-i\omega\tau} d\tau \tag{2.59}$$

and to the auto-covariance function is then defined as:

$$R_{XX}(\tau) = \frac{1}{2} \int_{-\infty}^{\infty} S_{XX}(\omega) e^{i\omega\tau} d\omega \tag{2.60}$$

Applied to the wave excitation force process:

$$\kappa_{M_{ex} M_{ex}}(\tau) = \int_{-\infty}^{\infty} \mathrm{e}^{i\omega\tau} S_{M_e M_e}(\omega) \, d\omega \tag{2.61}$$

The relationship between the auto-covariance and the auto-correlation function is given by division of the variance σ_{XX}^2, i.e.:

$$\rho_{M_{ex} M_{ex}}(\tau) = \frac{\kappa_{M_{ex} M_{ex}}(\tau)}{\sigma_{M_{ex} M_{ex}}^2} \tag{2.62}$$

By inserting the stochastic relations (variance and auto-covariance function) into the Eq. (2.54) we get the following

$$\bar{P}_c = \frac{1}{2c_c}\,\sigma^2_{\dot{M}_e} - \frac{1}{4c_c^2}\int_{-\infty}^{t} h_{r\dot{v}}(t-\tau)\kappa_{M_eM_e}(t-\tau)\,d\tau \;=$$
$$\sigma^2_{\dot{M}_e}\left(\frac{1}{2c_c} - \frac{1}{4c_c^2}\int_0^{\infty} \rho_{M_eM_e}(u)h_{r\dot{v}}(u)\,du\right) \tag{2.63}$$

$\rho_{M_{ex}M_{ex}}(\tau)$ denotes the auto-correlation coefficient function of the wave excitation process. The qualitative variation of $\rho_{M_eM_e}(\tau)$ has been shown on Fig. 2.20 for monochromatic, narrow-banded stochastic and broad-banded stochastic wave excitation forces. In order to make comparison meaningful, the separation time τ has been normalized with respect to the mean zero-upcrossing period T of the stochastic processes.

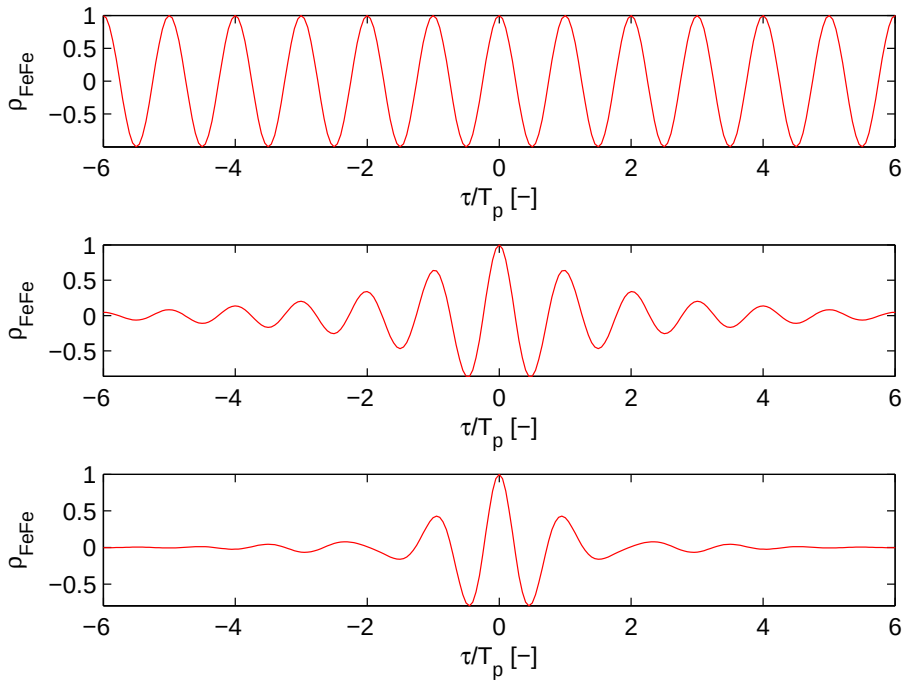

Figure 2.20 Autocorrelation coefficient function of the wave excitation force. a) Monochromatic wave excitation force. b) Narrow-banded stochastic excitation force (swells). c) Broad-banded stochastic wave excitation force (wind waves)

Now as we have expressed the power by two stochastic variables $\rho_{M_{ex}M_{ex}}(\tau)$ and the damping coefficient c_c we are interested if an optimal damping coefficient exists. We derive the expression in Eq. (2.61) and set it to zero:

$$\frac{\delta P_{c_c}}{\delta c_c} = 0 = \sigma^2_{M_{ex}M_{ex}} \left(-\frac{1}{2} c_c^{-2} + \frac{1}{2} c_c^{-3} \cdot \int_0^\infty \rho_{M_{ex}M_{ex}}(u) h_{\theta\dot{v}}(u) du \right) \tag{2.64}$$

Eq. 2.64 has three roots, i.e. $c_{c1} = 0$, $c_{c2} = 0$ and the third one is

$$c_{c3} = \int_0^\infty \rho_{M_e M_e}(u) h_{r\dot{v}}(u)\, du \tag{2.65}$$

Figure 2.23 shows the power in function of the damping coefficients. If Eq. (2.65) is inserted into the expression for the energy we get.

$$\bar{P}_{c,\mathrm{opt}} = \frac{1}{4} \frac{\sigma^2_{M_e}}{c_c} \tag{2.66}$$

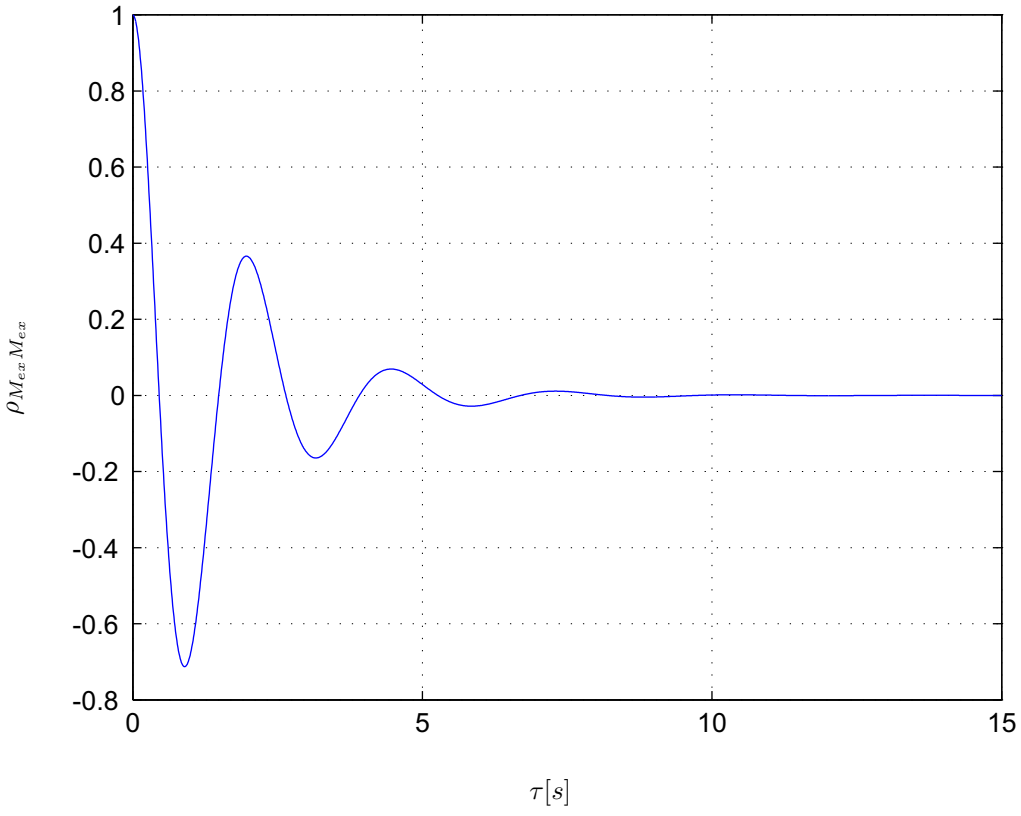

Figure 2.21 Auto-correlation function of the given wave process.

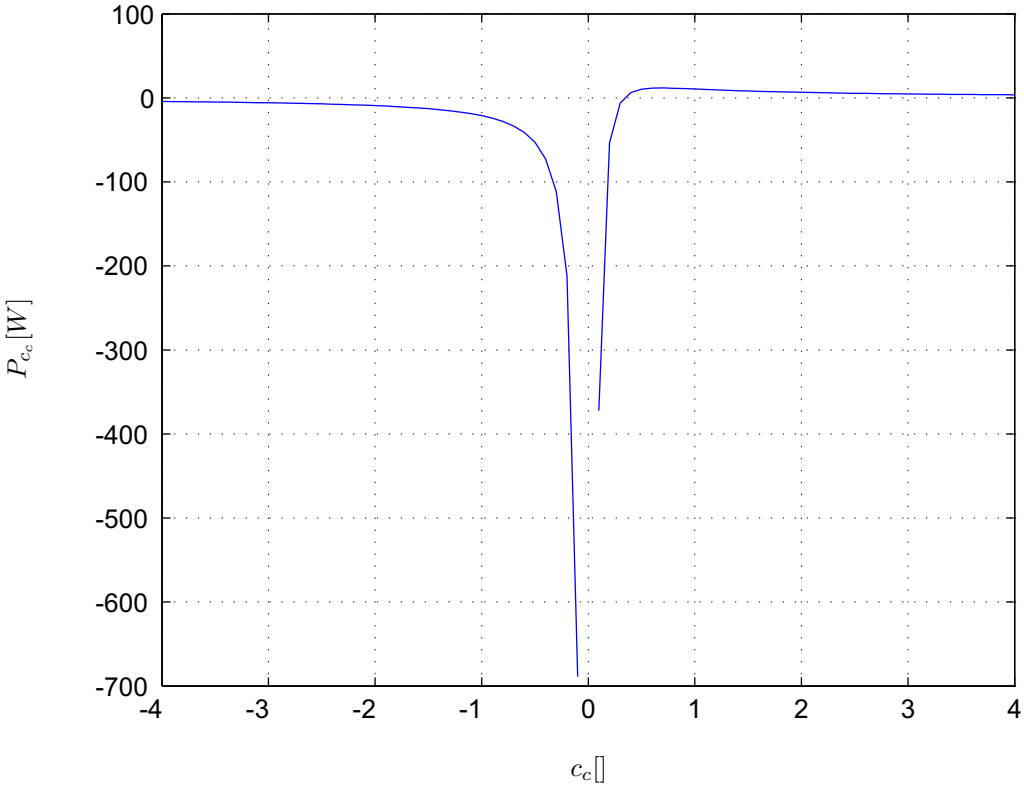

Figure 2.22 Corresponding power function in function of the damping coefficient - resonance control (Brutto power, energy which has been fed in by negative spring coefficient is not considered, $c_{opt} = 0.7 = c_{c3}$.

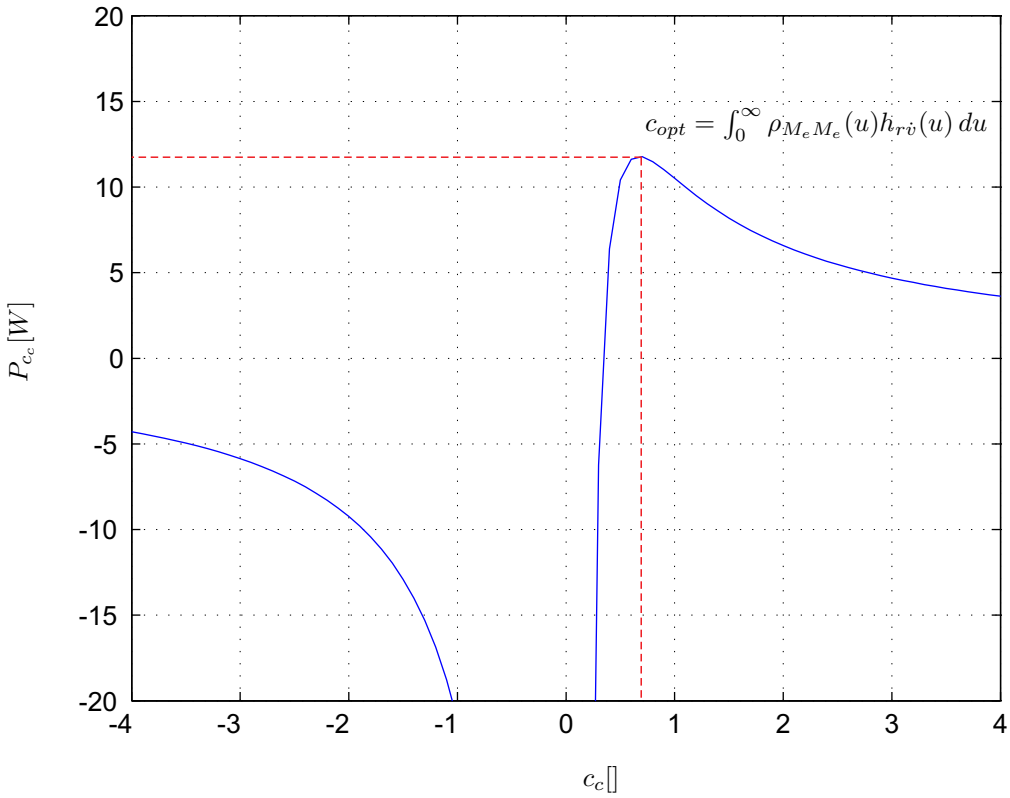

Figure 2.23 Corresponding power function in function of the damping coefficient - resonance control (Brutto power, energy which has been fed in by negative spring coefficient is not considered, $c_{opt} = 0.7 = c_{c3}$.

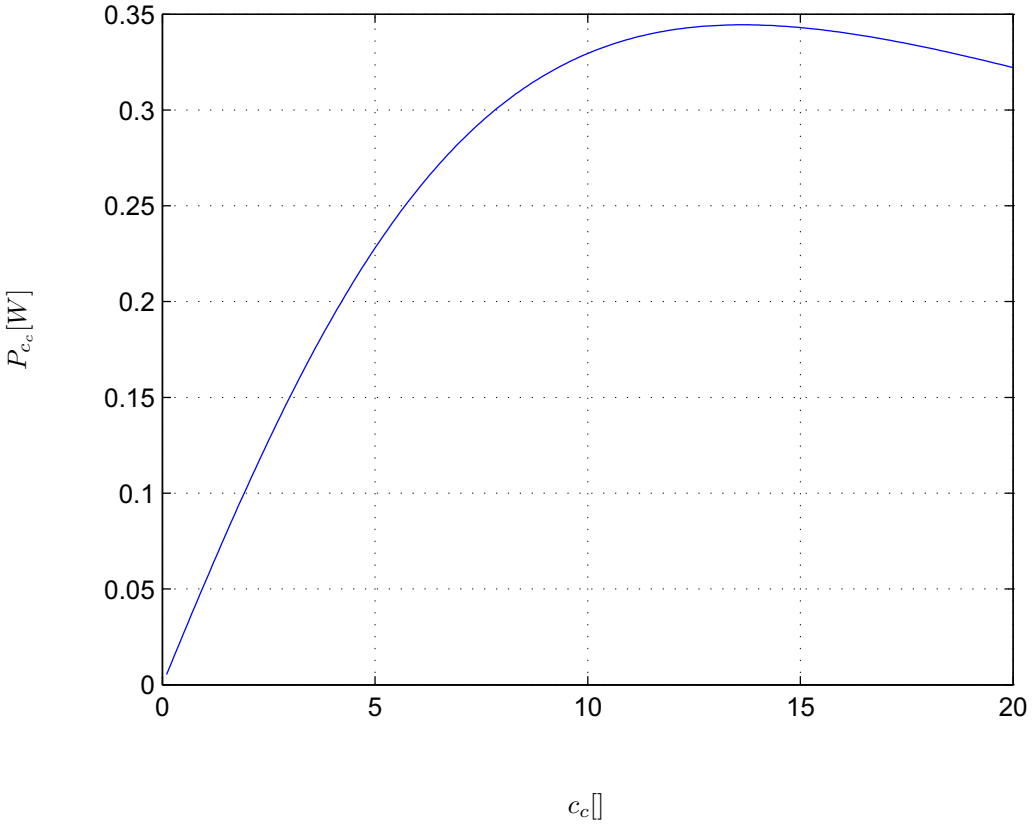

Figure 2.24 Corresponding power function in function of the damping coefficient - only passive control.

2.3.2 Performance of a WEC

The efficiency of a wave energy converter can be expressed by the non-dimensional performance index (NDI) which is given as:

$$\eta = \frac{P_{abs}}{P_{wave} \cdot d_{active}} \tag{2.67}$$

where P_{abs} is the absorbed wave energy by the device. This can be in the form of pneumatic, hydraulic or mechanical energy. P_{abs} has the units $[W]$ and is also referred to P_{num} or P_{exp} in this document. The generated power is referred as the mechanical power for the present device. P_{wave} corresponds to the available energy in the waves and has the units power per unit width, $[W/m]$. In the present case the calculation of P_{wave} is based on the wave elevation time series which is measured at the center of the float when the device was not in the water. The active width of the structure is referred as d_{active}. In the case of the WS absorber the active width is equal to the diameter of the float.
The transported wave power per unit width of the wave front, for plane progressive irregular waves in finite water depth is given as:

$$P_{wave} = 2\rho g \int_0^\infty S_{\eta\eta}(\omega) c_g(\omega) d\omega \tag{2.68}$$

where ρ is the water density, g is the acceleration of gravity, $S_{\eta\eta}(\omega)$ is the one sided wave spectrum, and $c_g(\omega)$ is the group velocity, which is a function of the wave frequency ω and the water depth h. The multiplication of the group velocity with the wave spectrum in Eqn. (2.68) results from the fact that the wave energy travels with the group velocity rather than with the phase velocity.

The non dimensional performance index (NDI) indicates the amount of energy which is absorbed by the device in a unit width of wave front relative to its geometry. This coefficient may be in principle larger than one. Figure 2.25 indicates three different cases where the coefficient is smaller, equal or bigger than one.

- $\eta < 1.0$ The absorbed energy is smaller than the wave energy traveling in the active width zone of the device.
- $\eta = 1.0$ The absorbed energy is equal to the wave energy "".
- $\eta > 1.0$ The absorbed energy is larger than the wave energy "".

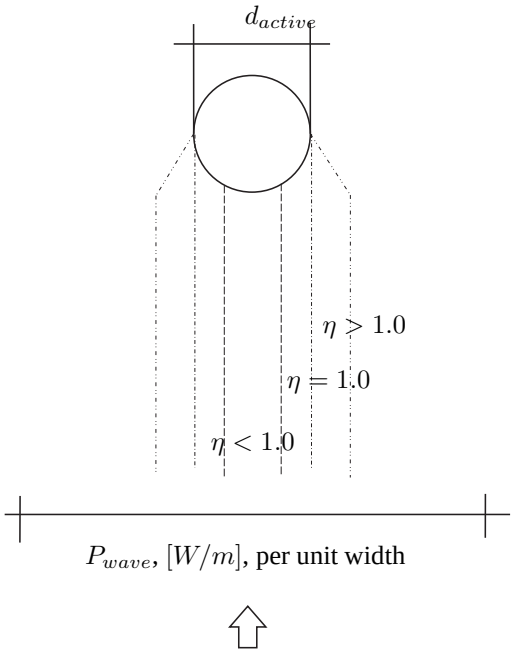

Figure 2.25 Non dimensional performance index η

CHAPTER 3
Description of the experimental setup

Contents:

- Experimental setup.
- Optimal damping coefficient.

3.1 Introduction

The dynamical behavior of a point absorber wave energy converter has been extensively investigated analytically and numerically during the past half century. The theoretical groundwork of wave power absorption considering simple geometries i.e. axisymmetric bodies oscillating in one mode was described by Evans, Mei and Newman in the late 1970s. Budal and Falnes have presented pioneering work in the beginning of the 1980s on experimental studies of a point absorber considering phase control. It was found that in order to apply optimum control it is necessary to predict an irregular wave some distance into the future.
More recent studies on advanced control strategies namely phase and amplitude control were carried out by Hals, Barbarit and Clement. A common characteristic of these models is the assumption of linear fluid structure interaction based on the linear wave-diffraction theory. Wave forces and corresponding dynamical responses are modeled using first order potential theory which satisfies the Laplacet's equation in the bulk of the fluid. Boundary conditions are formulated at the free surface by means of linearized Euler-Bernoulli pressure terms. A considerable drawback of this method, despite all the magnificent advantages, lies in the assumption of small waves heights and small body motions, two conditions which might be violated for many operational sea states.

3.2 Experimental setup

Experimental tests on a point absorber wave energy converter are carried out in the wave tank of Aalborg University. The tank has a length of 15 m, a width of 8 m and a maximum water depth

of 0.7 m. The wave paddles are driven by a total of 15 hydraulic pistons moving in the horizontal direction. The distance from the center of the float and the paddles is 5 m. A constant water depth of 0.65 m is chosen during all the tests. After 10 m the waves reach the slope of the beach. No active absorption is applied on the incoming waves thus a rather short duration of the time series has been chosen to avoid influences of any standing waves building up in the wave tank.
The test setup consists of a floating body in the shape of a hemisphere connected with a lever arm. The device rotates around a fixed point which is located 0.35 m above the mean water level. Pitch is the corresponding degree of freedom around the bearing point. The hydrodynamic parameters are therefore formulated as moments rather than forces or masses. The laboratory device is similar to the well-known Wavestar float located in the Danish North Sea. The test setup is modeled on a scale 20:1 compared to the prototype. A major characteristic of the laboratory model is the power take off system which consists of a linear generator based on the electromagnetic principle. This setup has a number of advantages. The control of the actuator can be either force control or motion control. In the following test series both configurations were applied. The experimental setup is shown in Fig. 3.1.

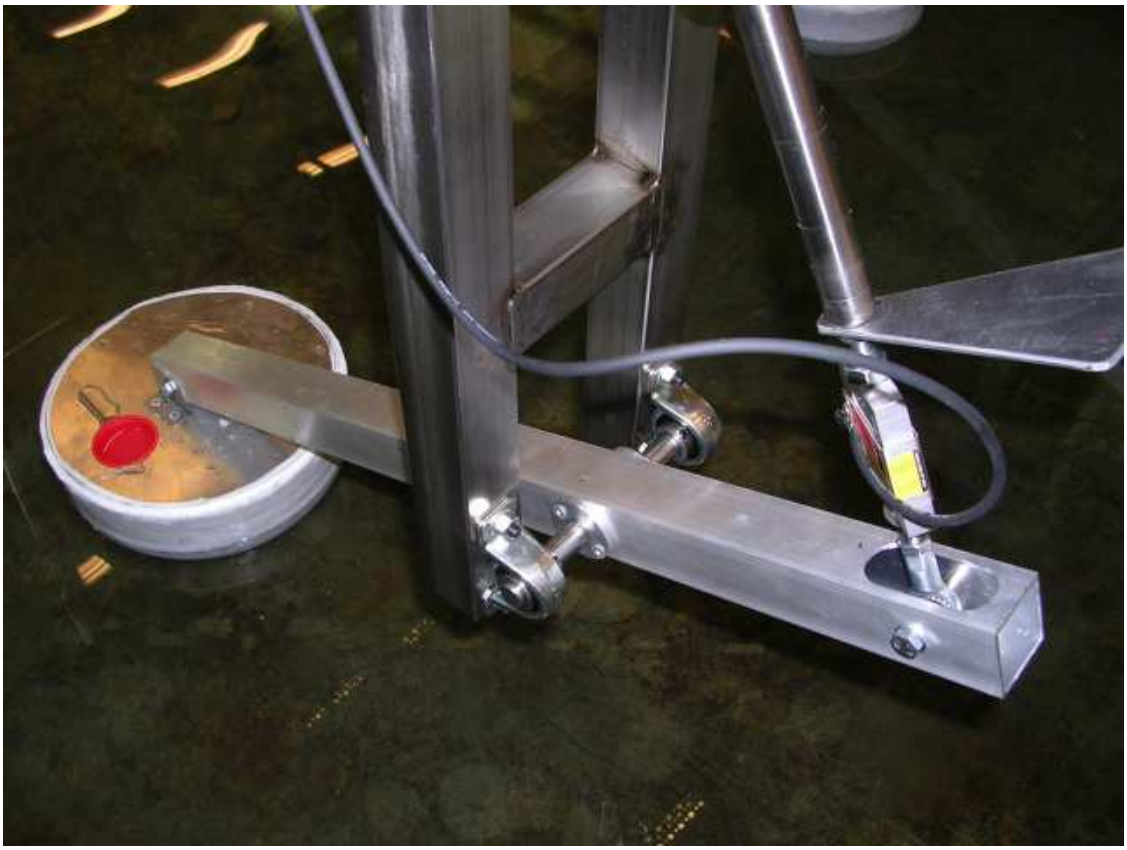

Figure 3.1 Experimental setup of the laboratory device.

3.2.1 Data acquisition

Force and displacement measurements were carried out on the device. Furthermore five wave gauges were placed in the vicinity of the float in order to measure the effective wave field, generated by the wave makers and oscillations by the device itself. A control program was developed in Simulink which was run on a different computer than the one used for the data acquisition. The control algorithm was programmed in Matlab and send to the controller via the Simulink model. The unfiltered force and displacement signals were reordered simultaneously through the use of an A/D converter. The sample frequency was 1000 Hz for the entire test runs. Down sampling of the time series was applied whenever needed in order to compare the results with the numerical calculations.

3.2.2 Design parameters

The design parameters of the laboratory scaled model are shown in Table 3.1. The applied scale law is 20:1 compared to the prototype model located in Hanstholm. The shape of the buoy corresponds to a Hemisphere where the sidewalls are slightly enlarged.

Table 3.1 Design parameters of the laboratory model.

Description:	Symbol:	Value:	Unit:
Length of the float arm:	L	0.680	m
Diameter of the float:	D_o	0.254	m
Lever arm initial:	c	0.200	m
Piston displacement:	$l(t)$	$var.$	m
Mass moment of Inertia:	j	0.96	kgm^2
Hydrostatic stiffness:	r_h	87.04	Nm
Added mass at infinitely high frequencies:	j_h^∞	0.41	kgm^2
Water depth:	h	0.650	m
Draught:	d	0.104	m
Wavelength:	λ	$var.$	m
Eigenfrequency:	ω_n	7.95	rad/s

3.2.3 Power-take off system

The wave energy absorber is equipped with an electric power generator via a linear actuator based on the electromagnetic principle. A linear movement, forced by the waves, generates a direct electromagnetic force without the use of mechanical devices such as cams, belts or gearboxes. The motor consists of two main parts: the slider and the stator. The slider is a precision assembly that consists of a stainless steel tube, which is filled with neodymium magnets. The stator, also called the bearing of the slider, contains the position sensors and a microprocessor board.

3.3 Sea states in the laboratory

Experimental tests on the point absorber have been carried out for regular and irregular waves. The waves were generated by the wave maker based on a Pierson Moskowitz spectrum. For the present analysis ten different irregular wave states are considered. The waves are unidirectional, two dimensional, longcrested waves. Two types of waves are analyzed; the first five waves states have a steepness ratio of 0.02 whereas the ratio for the second group is 0.04. An overview of the tested waves is shown in Table 3.2.

The analysis of the wave gauge signals is performed with the software programme Wavelab, (Wavelab 2012). It was found that the measured wave heights in the tank are slightly smaller than the target wave heights. The measured periods however correspond rather good with the target ones. It must be emphasized that the reliability of the H_{m0} and T_p is small since they are based on a short time series of approx. 300 sec. The measured irregular wave signals are used as input in the numerical time domain model. Thus the accuracy of the generated and measured waves does not affect the comparison between the experimental data and numerical calculation which will be shown later.

Table 3.2 Measured significant wave heights H_{m0} and measured peak periods T_p, total wave power P_{wave}, wave steepness $\frac{H_{m0}}{\lambda_p}$, non dimensional performance index for the ten analyzed wave states. The absorbed power was measured applying passive control by means of a linear damping coefficient - optimized for each sea state

Wave states	H_{m0} $[m]$	T_p $s]$	P_{wave} $[W/m]$	$\frac{H_{m0}}{\lambda_p}$ $[-]$	η [-]
IRA1	0.027	0.8	0.374	0.02	0.53
IRA2	0.044	1.25	1.174	0.02	0.37
IRA3	0.062	1.3	3.137	0.02	0.20
IRA4	0.080	2.5	6.024	0.02	0.19
IRA5	0.12	3.0	14.42	0.02	0.13
IRB1	0.055	0.85	1.520	0.04	0.52
IRB2	0.090	1.30	5.287	0.04	0.32
IRB3	0.115	1.35	10.83	0.04	0.23
IRB4	0.155	2.5	22.89	0.04	0.17
IRB5	0.232	3.0	51.36	0.04	0.12

The wave excitation moment is computed from the solution of the radiation problem. The latter relation is also known as the Haskind relation (Haskind 1953) and is considered to be computationally efficient because a single radiation solution can be used to compute the exciting moment for multiple angles of wave incidence without solving any additional hydrodynamic problems. In order to calculate the exact incident wave excitation moment, the undisturbed wave field at the center of the float had to be measured.

In a next step the same waves were run when the float was fixed at the equilibrium position. In this configuration the wave excitation moment was measured by a load transducer and compared with the wave excitation based on the linear wave theory. For moderate sea-states

wave excitation moment and the measurement are almost in perfect agreement, see Fig. 3.2. For steeper waves, where partial submergence and overtopping of the float was observed, the force sensor was unable to measure the signal accurately, see Fig. 3.3. The numerical excitation moment was calculated by means of a convolution integral. The following linear relationship is assumed:

$$M_{ex} = \int_0^\infty h_{e\eta}(t-\tau)\eta_m(t)d\tau \tag{3.1}$$

where $\eta_m(t)$ is the measured wave elevation at the position of the float, and $h_{e\eta}$ is the linear impulse response function of the excitation moment.

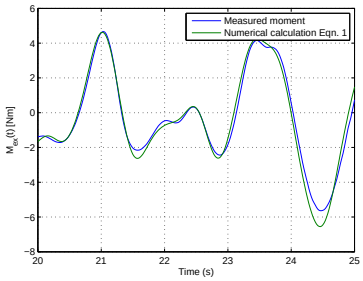

Figure 3.2 Measured moment by the load cell when the device is fixed compared with the calculated wave excitation moment based on the measured wave elevations when the float was taken out of the water in moderate sea state, $IRA4 : H_{m0} = 0.08m, T_p = 2.5sec.$

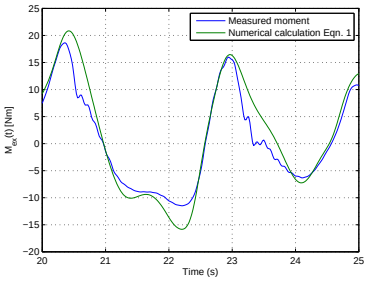

Figure 3.3 Measured moment by the load cell when the device is fixed compared with the calculated wave excitation moment based on the measured wave elevations when the float was taken out of the water in extreme sea, $IRB5 : H_{m0} = 0.232m, T_p = 3.0sec.$

3.4 Optimal damping coefficient

In the previous chapter a stochastic analysis of the wave state has been presented. It was discussed that the maximum power can be extracted from the waves when the device oscillates in resonance with the incoming wave excitation process. The input as well as the output were assumed to be a stationary process. Assuming that the device oscillates in resonance with the incoming wave frequency, the optimal damping coefficient becomes a function of the auto-correlation coefficient function of the wave excitation process and the impulse response function of the radiation force.

In this section the equations in chapter 2 will be applied for the wave states which are analyzed in the laboratory, see Table 3.2. The calculation of the optimal damping coefficient for a given irregular wave state based on Eqn. (2.65) requires the analysis of the wave elevation time series.

The signal shown in Fig. 3.4 corresponds to the wave elevation at the center of the absorber when measured without the absorber in the water. A FFT analysis is carried out using a home

made function which returns the power spectrum as a function of the angular frequency ω. The analysis is carried out for all the measured wave elevation signals, see Fig. 3.6 to Fig. 3.24. One of the main features of the FFT analysis is the conservation of energy of the original time series. The energy in the signal can be expressed by the variance and for the FFT spectrum it is the area under the curve, i.e. the zero'th moment. The calculated variance and zero'th moment are listed in Table 3.3. In order to smooth the power spectrum the WAFO package has been used which has an inbuilt function for performing FFT with a desired amount of smoothing. The smoothing is controlled by the parameter L (maximum lag size of the window function). For lower values of L, increased smoothing is applied. For each of the ten different power spectrums two different smoothing parameters have been applied, i.e. L=300 and L=1500. On top of the three power spectrums which were based on the measured data sets, a Pierson Moskowitz spectrum has been plotted in order to compare the discrepancy to the target value. It was found, that the variance of the wave signals in the tank is remarkably smaller than the theoretical one. This problem has already been discussed and is due to the fact that the significant wave heights in the tank differ from the target wave heights.

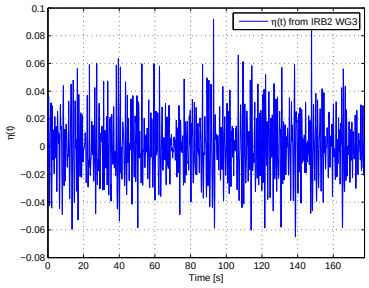

Figure 3.4 Wave elevation at the center of the float without the absorber in the water for a Pierson Moskowitz, $H_{m0} = 0.092m$, $T_p = 1.25sec$.

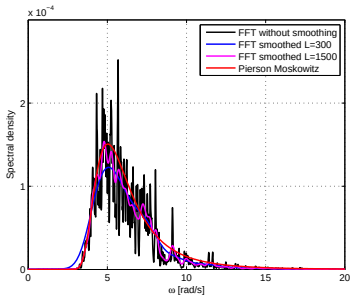

Figure 3.5 FFT with two different degrees of smoothing compared to the non-smoothed FFT spectrum of the wave elevation.

	IRB2 WG3
Variance:	$4.6507 \cdot 10^{-4}$
m_0:	$4.6502 \cdot 10^{-4}$

Table 3.3 Variance of the time series and zero'th moment of response spectra.

The optimal damping value is then calculated by means of a stochastic analysis. Based on the frequency response function $H_{e\eta(\omega)}$ of the excitation moment, the auto-covariance function can be calculated as follows:

$$\kappa_{M_e M_e}(\tau) = \int_{-\infty}^{\infty} \mathrm{e}^{i\omega\tau} S_{M_e M_e}(\omega)\, d\omega = \int_{-\infty}^{\infty} \mathrm{e}^{i\omega\tau} |H_{e\eta}(\omega)|^2\, S_{\eta\eta}(\omega)\, d\omega \tag{3.2}$$

where $S_{\eta\eta}(\omega)$ is the equivalent to the power spectrum of the measured wave states, a smoothing factor of L=300 has been used, see previous plots. The auto-correlation coefficient reads:

$$\rho_{M_e M_e}(\tau) = \frac{\kappa_{M_e M_e}(\tau)}{\sigma^2_{M_e}} \tag{3.3}$$

The optimal damping coefficient is then calculated as follows: ref. to Chapter 2.6:

$$c_c = \int_0^\infty \rho_{M_e M_e}(u) h_{r\dot{\theta}}(u)\, du \tag{3.4}$$

Table 3.4 Evaluation of equation (40) for two different incident wave angles.

Strategy	c_c $[Nm/rad/s^2]$ 90 deg	c_c $[Nm/rad/s^2]$ 0 deg
IRA1	2.031	1.820
IRA2	1.601	1.356
IRA3	1.303	0.879
IRA4	0.948	0.668
IRA5	0.651	0.632
IRB1	1.975	1.799
IRB2	1.581	1.332
IRB3	1.280	0.864
IRB4	0.928	0.662
IRB5	0.651	0.665

The plots of the power spectrums of each wave state are shown below.

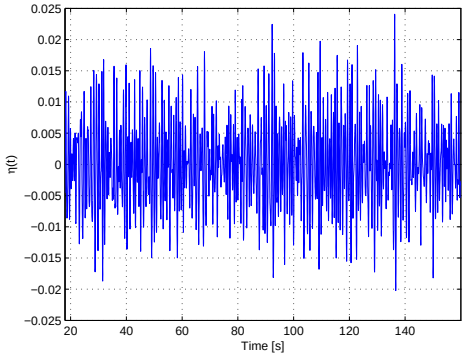

Figure 3.6 Time series of IRA1.

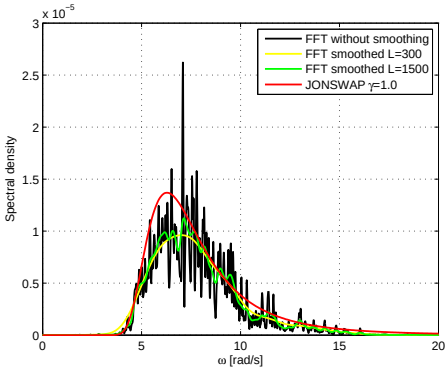

Figure 3.7 Fastfourier analysis of IRA1 for different smoothing levels.

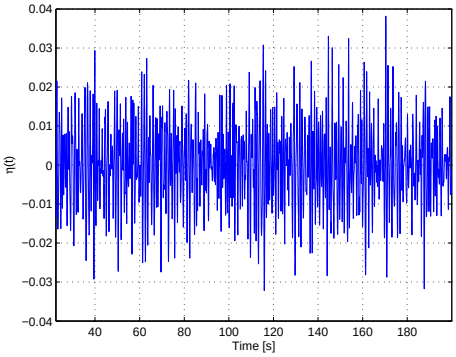

Figure 3.8 Time series of IRA2.

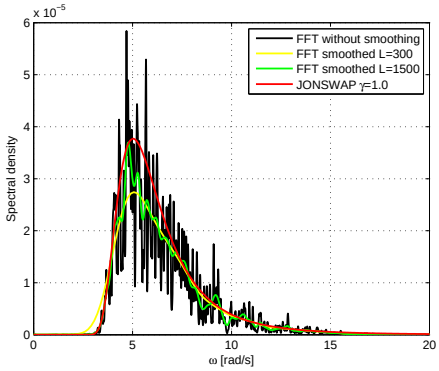

Figure 3.9 Fastfourier analysis of IRA2 for different smoothing levels.

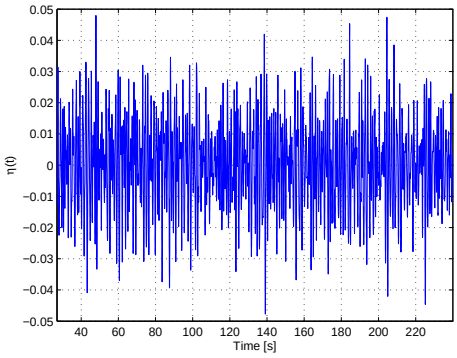

Figure 3.10 Time series of IRA3.

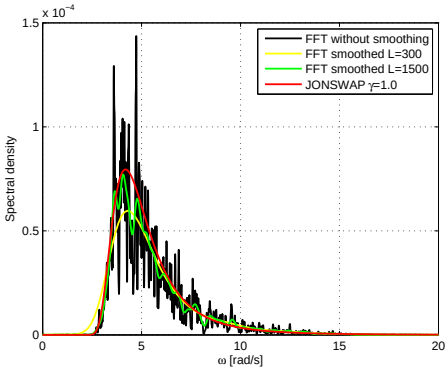

Figure 3.11 Fastfourier analysis of IRA3 for different smoothing levels.

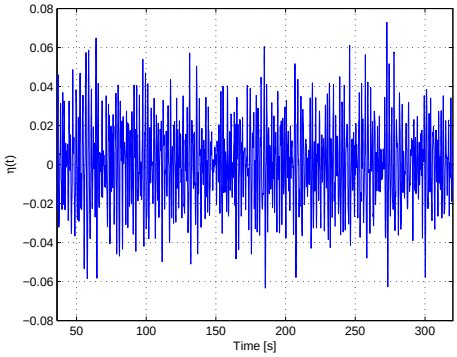

Figure 3.12 Time series of IRA4.

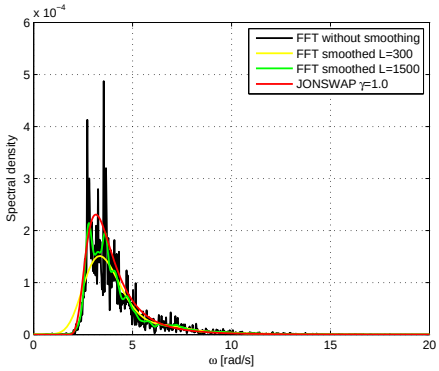

Figure 3.13 Fastfourier analysis of IRA4 for different smoothing levels.

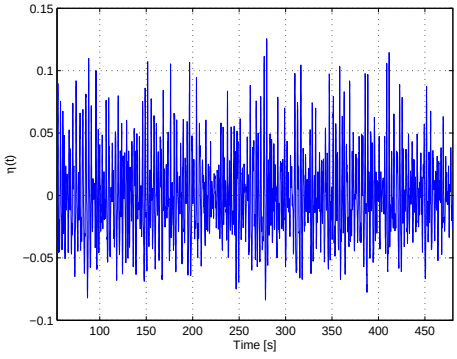

Figure 3.14 Time series of IRA5.

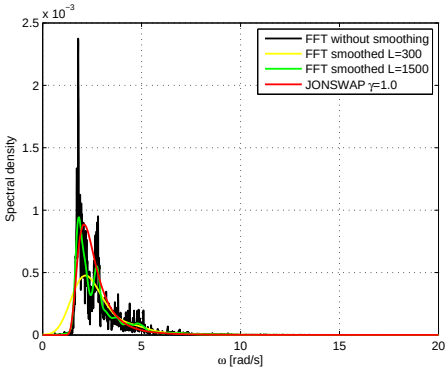

Figure 3.15 Fastfourier analysis of IRA5 for different smoothing levels.

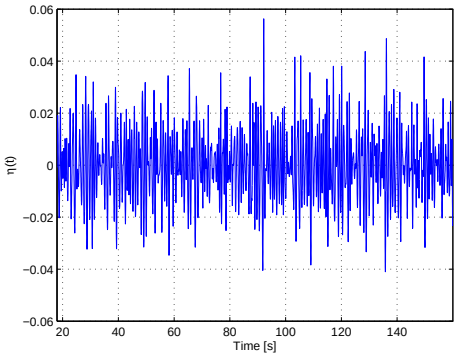

Figure 3.16 Time series of IRB1.

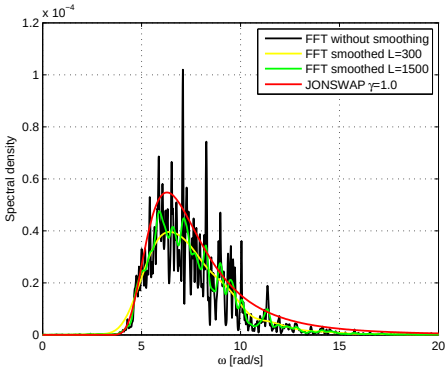

Figure 3.17 Fastfourier analysis of IRB1 for different smoothing levels.

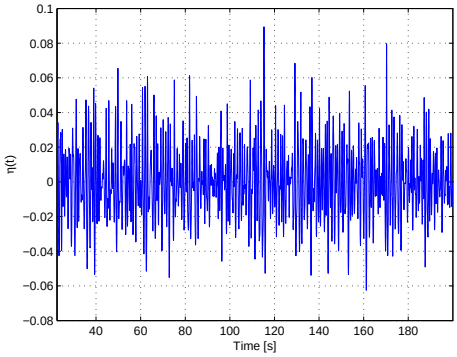

Figure 3.18 Time series of IRB2.

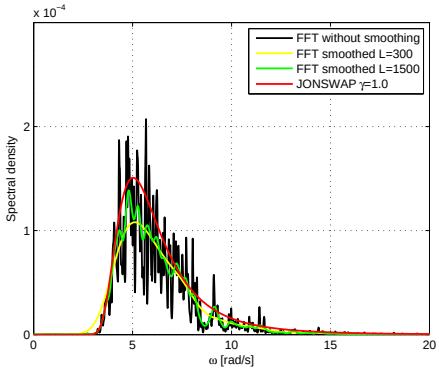

Figure 3.19 Fastfourier analysis of IRB2 for different smoothing levels.

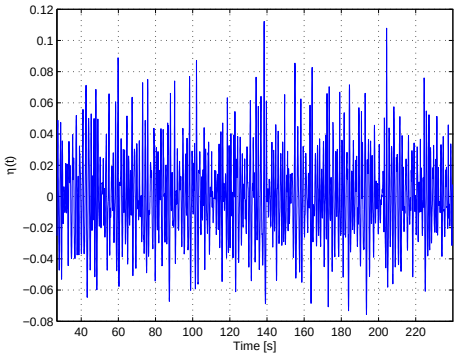

Figure 3.20 Time series of IRB3.

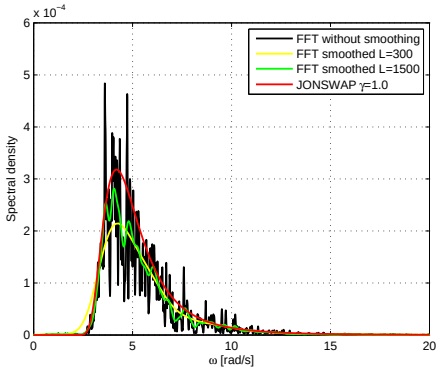

Figure 3.21 Fastfourier analysis of IRB3 for different smoothing levels.

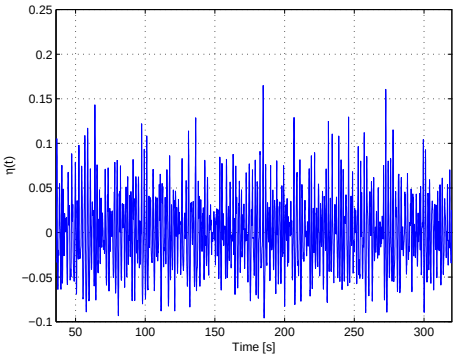

Figure 3.22 Time series of IRB4.

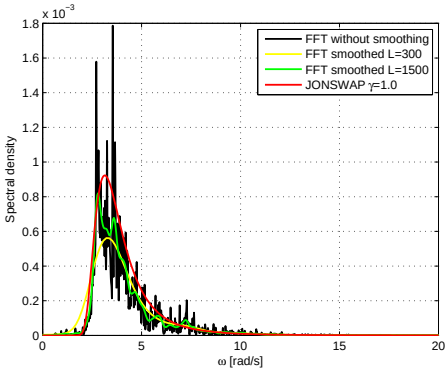

Figure 3.23 Fastfourier analysis of IRB3 for different smoothing levels.

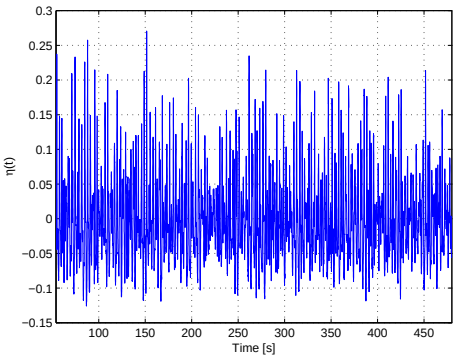

Figure 3.24 Time series of IRB5.

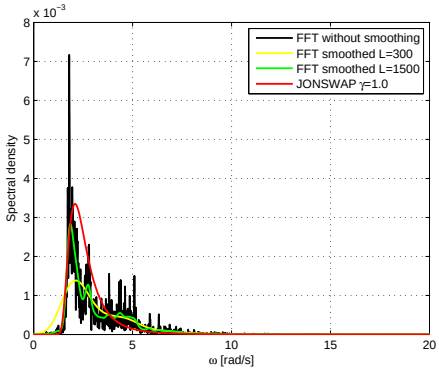

Figure 3.25 Fastfourier analysis of IRB5 for different smoothing levels.

CHAPTER 4
Results

Contents:

- Defining control strategies A to D.
- Annual power production at the test site in Hanstholm.

4.1 Control Strategies A-D

Four different control strategies are tested and are denoted as A, B, C and D. The aim is to continuously approach the optimal situation where the wave excitation force is in phase with the bodys velocity. With each strategy an additional term is introduced in the control moment of Eqn. 4.1 until the optimal is reached. The following table summaries the results when the device is situated parallel to the incoming waves, i.e. at a $90\,\mathrm{deg}$ incident wave angle. Time series are shown for each strategy in the next chapters. The control moment in its general form is given below:

$$M_c(t) = m_c\ddot{\theta}(t) + c_c\dot{\theta}(t) + k_c\theta(t) + b_c\int_{-\infty}^{\infty} h_{c\dot{\theta}}(t-\tau)\dot{\theta}(\tau)\,d\tau \tag{4.1}$$

A – Only the gain factor c_c proportional to the velocity is varied, in a way that a maximum electrical power can be absorbed by the generator. The coefficient is optimized for irregular waves by considering a regular wave train with the peak period of the spectrum.

B – The damping c_c and the stiffness coefficients k_c are varied. The power is maximized by optimizing the coefficients with two variable optimization criterion.

C – The control moment involves a mass moment of inertia m_c, a stiffness coefficient k_c and a damping coefficient c_c. The derivative gain factor c_c is determined by an optimality criterion for the absorbed mean power of the control force under the given sea state.

D – Strategy D involves all the four coefficients in the control moment, namely m_c, c_c, k_c and b_c. Under this condition the applied control law enforces the absorber into phase with the wave excitation moment.

The table 4.1 show the results for three different control strategies, namely A, B and C for four selected wave states. The results show clearly that the efficiency of the device can be increased by a control strategy which enforces the float to oscillate in resonance with the peak period. The power production i.e. P_{inst} is always expressed as the net energy flow, i.e. the energy which has been pumped into the system is subtracted from the instantaneous power production.

Table 4.1 Overview of the non-dimensional performance index, maximum instantaneous mechanical power for: Strategy A; passive control i.e. linear damping coefficient, Strategy B; reactive control with a linear negative spring stiffness and Strategy C; with a damping coefficient, negative spring and a negative mass moment of inertia for the measured irregular wave states (selection).

Measured waves:			A		B		C	
	H_{m0} [m]	T_p [s]	η [-]	P_{inst} [W]	η [-]	P_{inst} [W]	η [-]	P_{inst} [W]
IRA 1	0.031	1.0	0.53	0.6	0.6	1.0	0.8	2.8
IRA 2	0.046	1.25	0.37	1.2	0.7	9.5	0.9	14.7
IRB 1	0.06	1.0	0.52	2.3	0.62	5.1	0.88	20.2
IRB 2	0.09	1.25	0.32	5.06	0.67	34.4	0.88	54.8

4.1.1 Numerical results of each wave state

In the following, the numerical values are shown for each wave state.

Table 4.2 Control strategies A-D: IRA1

IRA1	m_c $[Nm/rad/s^2]$	c_c $[Nm/rad/s]$	k_c $[Nm/rad]$	b_c [-]	P_{abs} $[W]$	η $[-]$	P_{ins} $[W]$	$\frac{P_{inst}}{P_{abs}}$ [-]	$\frac{M_{c,inst}}{M_{c,ave}}$ [-]
A	0	4.0	0	0	0.051	0.5	0.6	11	3.8
B	0	3.0	-31.9	0	0.060	0.6	1.0	17	3.9
C	-1.0	2.2	-71.4	0	0.081	0.8	2.8	34	3.9
D	-0.96	2.0	-	0	0.087	0.9	–		

Table 4.3 Control strategies A-D: IRA2

IRA2	m_c $[Nm/rad/s^2]$	c_c $[Nm/rad/s]$	k_c $[Nm/rad]$	b_c [-]	P_{abs} $[W]$	η $[-]$	P_{ins} $[W]$	$\frac{P_{inst}}{P_{abs}}$ [-]	$\frac{M_{c,inst}}{M_{c,ave}}$ [-]
A	0	4.0	0	0	0.10	0.3	1.2	11.5	3.8
B	0	2.0	-51.4	0	0.23	0.7	9.5	41.6	4.2
C	-1.1	2.0	-79.2	0	0.29	0.9	14.7	49.6	4.0
D	-0.96	1.6	-76.6	0	0.35	1.1	–		

Table 4.4 Control strategies A-D: IRA3

IRA3	m_c $[Nm/rad/s^2]$	c_c $[Nm/rad/s]$	k_c $[Nm/rad]$	b_c [-]	P_{abs} $[W]$	η $[-]$	P_{ins} $[W]$	$\frac{P_{inst}}{P_{abs}}$ [-]	$\frac{M_{c,inst}}{M_{c,ave}}$ [-]
A	0	9.0	0	0	0.18	0.2	1.9	12.1	3.8
B	0	2.0	-61.82	0	0.64	0.8	28.07	43.54	3.9
D	-0.96	1.3	-	0	0.89	1.2	–		

Table 4.5 Control strategies A-D: IRA4

IRA4	m_c $[Nm/rad/s^2]$	c_c $[Nm/rad/s]$	k_c $[Nm/rad]$	b_c [-]	P_{abs} $[W]$	η $[-]$	P_{ins} $[W]$	$\frac{P_{inst}}{P_{abs}}$ [-]	$\frac{M_{c,inst}}{M_{c,ave}}$ [-]
A	0	15.0	0	0	0.29	0.19	4.0	13.6	3.4
B	0	1.0	-72.5	0	2.42	1.6	435	180	4.5
D	-0.96	0.95	-	0	3.14	2.0	–		

Table 4.6 Control strategies A-D: IRA5

IRA5	m_c $[Nm/rad/s^2]$	c_c $[Nm/rad/s]$	k_c $[Nm/rad]$	b_c [-]	P_{abs} $[W]$	η $[-]$	P_{ins} $[W]$	$\frac{P_{inst}}{P_{abs}}$ [-]	$\frac{M_{c,inst}}{M_{c,ave}}$ [-]
A	0	25.0	0	0	0.59	0.14	8.4	14.1	4.8
A	0	1.0	-77.7	0	11.30	3.13	2310	204	3.85
D	-0.96	0.595	-	0	16.9	4.6	–		

Table 4.7 Control strategies A-D: IRB1

IRB1	m_c $[Nm/rad/s^2]$	c_c $[Nm/rad/s]$	k_c $[Nm/rad]$	b_c [-]	P_{abs} $[W]$	η $[-]$	P_{ins} $[W]$	$\frac{P_{inst}}{P_{abs}}$ [-]	$\frac{M_{c,inst}}{M_{c,ave}}$ [-]
A	0	4.0	0	0	0.20	0.53	2.3	14.1	4.8
B	0	3.0	-31.4	0	0.25	0.62	5.1	20.5	4.5
C	-1.1	1.97	-76.4	0	0.34	0.88	20.18	59.1	5.1
D	-0.96	1.97	-	0	0.36	0.92	–		

Table 4.8 Control strategies A-D: IRB2

IRB2	m_c $[Nm/rad/s^2]$	c_c $[Nm/rad/s]$	k_c $[Nm/rad]$	b_c [-]	P_{abs} $[W]$	η $[-]$	P_{ins} $[W]$	$\frac{P_{inst}}{P_{abs}}$ [-]	$\frac{M_{c,inst}}{M_{c,ave}}$ [-]
A	0	7.0	0	0	0.44	0.33	5.06	13.4	4.3
B	0	2.0	-51.4	0	0.90	0.67	34.4	38.0	3.8
C	-1.1	1.97	-76.4	0	0.34	0.88	20.18	59.1	5.1
D	-0.96	1.6	-	0	1.3	0.96	–		

Table 4.9 Control strategies A-D: IRB3

IRB3	m_c $[Nm/rad/s^2]$	c_c $[Nm/rad/s]$	k_c $[Nm/rad]$	b_c [-]	P_{abs} $[W]$	η $[-]$	P_{ins} $[W]$	$\frac{P_{inst}}{P_{abs}}$ [-]	$\frac{M_{c,inst}}{M_{c,ave}}$ [-]
A	0	7.0	0	0	0.64	0.23	6.75	11.0	4.0
B	0	2.0	-61.9	0	2.33	0.85	152	65.3	4.0
D	-0.96	1.3	-	0	3.3	1.18	–		

Table 4.10 Control strategies A-D: IRB4

IRB4	m_c $[Nm/rad/s^2]$	c_c $[Nm/rad/s]$	k_c $[Nm/rad]$	b_c [-]	P_{abs} $[W]$	η $[-]$	P_{ins} $[W]$	$\frac{P_{inst}}{P_{abs}}$ [-]	$\frac{M_{c,inst}}{M_{c,ave}}$ [-]
A	0	15.0	0	0	1.12	0.19	11.3	10.13	4.0
B	0	2.0	-69.5	0	8.37	1.44	579	69	4.0
D	-0.96	0.93	-	0	11.9	2.05	–		

Table 4.11 Control strategies A-D: IRB5

IRB5	m_c $[Nm/rad/s^2]$	c_c $[Nm/rad/s]$	k_c $[Nm/rad]$	b_c [-]	P_{abs} $[W]$	η $[-]$	P_{ins} $[W]$	$\frac{P_{inst}}{P_{abs}}$ [-]	$\frac{M_{c,inst}}{M_{c,ave}}$ [-]
A	0	20.0	0	0	2.02	0.15	32.7	16.2	5.2
B	0	20.0	0	0	2.02	0.15	32.7	16.2	5.2
D	-0.96	0.93	-	0	48.7	3.73	–		

4.1.2 Strategy A - Time series

For this control strategy only the gain factor c_c proportional to the velocity $\dot{\theta}$ is varied, in a way that a maximum electrical power can be absorbed by the generator. The optimization of c_c is done for ten different irregular wave states. Figure 4.2 and Fig. 4.1 show the time series for one irregular wave state with a wave height of $H_{m0} = 0.055m$ and a wave period of $T_p = 0.85sec$ i.e. IRB1. Note that the instantaneous peak of the mechanical energy is approximately 2.3 [W] compared to an average power of 0.2 [W]. The load factor is defined as the average power divided by the instantaneous peak power. Thus, a load factor of 0.08 can be calculated for this wave state.

The capture width ratio for this wave state is $\eta = 0.53$. The average power in function of the damping coefficient are shown in Fig. 4.3 and Fig. 4.4 and compared with the experimental data from the tests. For the passive damped case the comparison between the numerical and experimental tests are in very good agreement. The buoys displacement is shown in Fig. 4.1. The maximum rotational angle is 0.1089 rad. This corresponds to a vertical displacement of 0.0523 m which is smaller than the draft of the float. Hence the float is not expected to rise out of the water thus the linear model may be applied.

Next, the velocity and the excitation force are compared for two wave states. For the first case the peak period of the waves is close to the natural period of the oscillator thus the velocity and the excitation force is almost in phase without applying reactive control, see Figure **??**. The power absorbtion is maximized in this situation. For the second wave state the peak period is higher than the natural period which leads to a small phase shift of the velocity and the excitation force, see Figure 4.6.

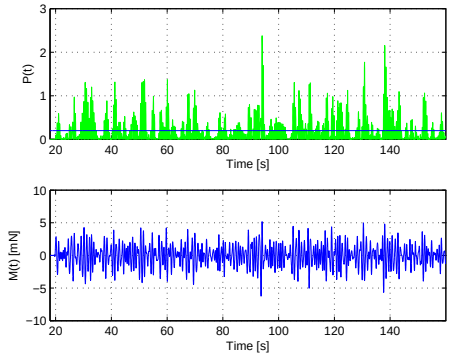

Figure 4.1 Strategy A, blue line corresponds to the free float, whereas the red line is the passive damped oscillator, $m_c = 0$, $c_c = 4Nm/rad/s$, $k_c = 0$, $b_c = 0$, IRB1

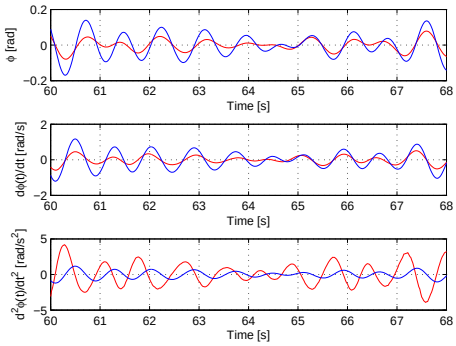

Figure 4.2 Strategy A, power, feedback moment, $m_c = 0$, $c_c = 4Nm/rad/s$, $k_c = 0$, $b_c = 0$, IRB1

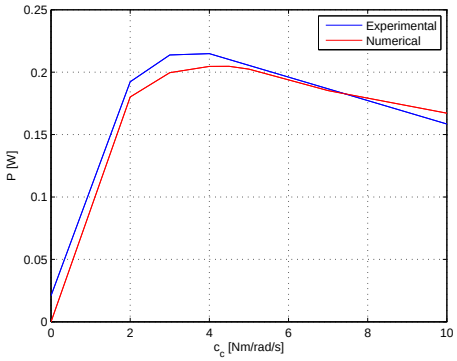

Figure 4.3 Average power in function of the damping coefficient, comparison between numerical model and experimental results - IRB1

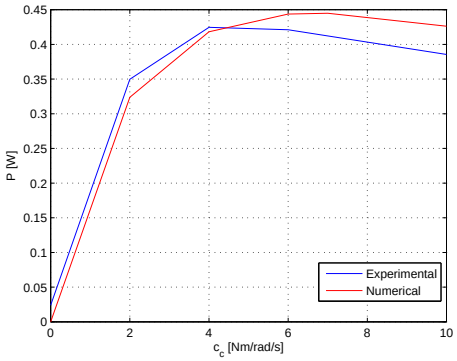

Figure 4.4 Average power in function of the damping coefficient, comparison between numerical model and experimental results - IRB2

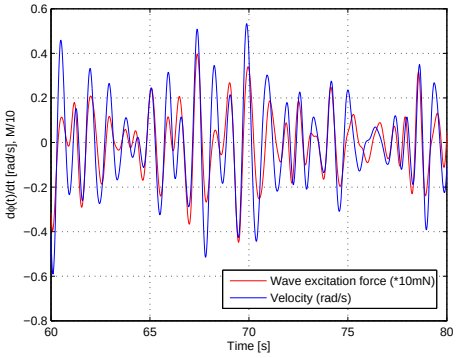

Figure 4.5 Velocity in blue line and excitation force in red line - passive control, the peak period of the excitation force is almost the same as the natural period, velocity and excitation force are almost in phase, IRB1

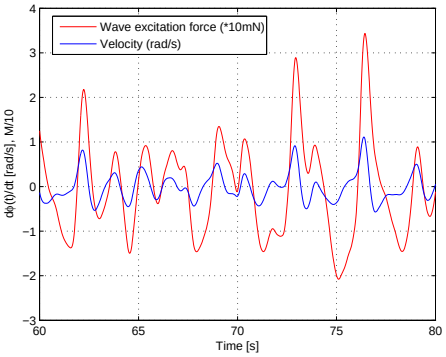

Figure 4.6 Velocity in blue line and excitation force in red line - passive optimal control, velocity and excitation force are out of phase, IRB5

Annual energy production for a discrete number of wave states

The annual energy production (AEP) is calculated for the Hanstholm wave conditions. A selected number of wave states are considered for this calculation i.e. the standardized wave states describing the energy content in the Danish seas. Table 4.12 is based on a review of the existing data on the wave condition at Hanstholm harbour, Ref. (Margheritini 2012).

The wave states are Froude-scaled with a model parameter of 1:20. The water depth in Hanstholm where the device is located is approximately 8 m whereas the water depth in the laboratory is at 0.65 m. The annual energy production of the laboratory model considering an incident wave angle of $90\,\mathrm{deg}$ is 0.54 [W]. For a full scale model the annual energy output per float is equal to 19 [kW]. This value is an upper bond because only the favorable incident wave angle is considered in the calculation. In reality the waves are 3D. Table 4.12 gives the results of the analysis for the given wave states. The irregular time series were calculated based on a Pierson Moskowitz spectrum. The damping value is optimized for each irregular wave state by a simple optimality criterion and is listed in the last column of the table.

It can be seen that the damping coefficient does not vary considerably with the peak period resulting in a very flat power curve. The last wave state is an extreme event for which the device will not be in operation.

Table 4.12 Performance calculation for the standardized wave states at Hanstholm harbour, control strategy A, selected wave states.

Selected wave states Hanstholm	H_{m0} $[m]$	T_p $[s]$	$P_{prob.}$ $[-]$	P_{abs} $[W]$	$\frac{H_{m0}}{\lambda_p}$ $[-]$	$P_{abs} * P_{rob.}$ $[W]$	c_{opt} $[Nm/rad/s^2]$
1	0.045	1.051	0.545	0.242	0.026	0.13	4
2	0.075	1.163	0.182	0.658	0.036	0.11	4
3	0.100	1.230	0.107	1.167	0.043	0.12	5
4	0.125	1.319	0.052	1.790	0.047	0.08	5
5	0.150	1.431	0.027	2.460	0.049	0.05	6
6	0.190	1.610	0.018	3.577	0.052	0.05	7
7	0.260	1.901	0.001	–	0.055	0	–
Total AEP						0.54	

Annual energy production for a full scatter diagram

The annual energy production is calculated for the full scatter diagram at the Hanstholm test site. The applied control strategy is simple and efficient i.e. passive damping has been applied. The damping coefficient is optimized for each irregular wave state.

In Fig. 4.7 the optimal damping coefficient is given in the first column for each peak period of the scatter diagram. The red numbers indicate the wave states for which the linear numerical model is not appropriate to calculate the dynamical response of the float. In other words the experiments have shown that the linear fluid-structure assumption is only valid for a steepness factor smaller than 0.05. The maximum wave height for which energy can still be produced is 3.5 m. For wave states above this level the structure enters into a protection mode.
The annual energy production for the laboratory model is approximately 0.58 [W]. Note that this value is approximately the same as we have found in the previous calculation however the computational burden is much higher when considering all the wave states in a scatter diagram. In this calculation the damping coefficient has been optimized for each peak period of the scatter diagram. Keeping the damping coefficient constant at a value of 8 Nm/rad/s, for instance, would reduce the the annual power production to about 0.5442 [W], i.e. minus 7 % compared to the case where the damping coefficient is changed to each each wave period. The power matrix for the situation where the damping coefficient is held constant is shown in Figure 4.10. The difference is visible in the maximum value of the power production indicated at the colorbar on the right hand side.

	Scale 1:20	c_opt	[Nm/rad/s^2]																			
	Hm0/λm0	9	9	7	5	4	4	4	5	5	6	7	8	9	9	9	10	13	14	15	16	17
	Hm0 - Tm01	0,25	0,56	0,67	0,78	0,89	1,01	1,12	1,23	1,34	1,45	1,57	1,68	1,79	1,90	2,01	2,12	2,24	2,35	2,46	2,57	3,58
In operation	0,01	0,06	0,01	0,01	0,01	0,01	0,00	0,00	0,00	0,00	0,00	0,00	0,00	0,00	0,00	0,00	0,00	0,00	0,00	0,00	0,00	0,00
	0,03	0,31	0,06	0,04	0,03	0,02	0,02	0,02	0,01	0,01	0,01	0,01	0,01	0,01	0,01	0,01	0,01	0,01	0,01	0,01	0,00	0,00
	0,05	0,51	0,10	0,07	0,05	0,04	0,03	0,03	0,02	0,02	0,02	0,02	0,01	0,01	0,01	0,01	0,01	0,01	0,01	0,01	0,01	0,01
	0,08	0,82	0,16	0,11	0,08	0,06	0,05	0,04	0,04	0,03	0,03	0,02	0,02	0,02	0,02	0,02	0,02	0,02	0,01	0,01	0,01	0,01
	0,10	1,02	0,20	0,14	0,11	0,08	0,06	0,05	0,04	0,04	0,03	0,03	0,03	0,03	0,02	0,02	0,02	0,02	0,02	0,02	0,02	0,01
	0,13	1,33	0,27	0,19	0,14	0,11	0,08	0,07	0,06	0,05	0,04	0,04	0,04	0,03	0,03	0,03	0,03	0,03	0,02	0,02	0,02	0,02
	0,15	1,54	0,31	0,21	0,16	0,12	0,10	0,08	0,07	0,06	0,05	0,05	0,04	0,04	0,04	0,03	0,03	0,03	0,03	0,03	0,02	0,02
	0,18	1,84	0,37	0,26	0,19	0,15	0,11	0,09	0,08	0,07	0,06	0,06	0,05	0,05	0,04	0,04	0,04	0,03	0,03	0,03	0,03	0,02
	0,20	2,05	0,41	0,29	0,21	0,16	0,13	0,10	0,09	0,08	0,07	0,06	0,06	0,05	0,05	0,04	0,04	0,04	0,04	0,03	0,03	0,02
Safe mode	0,23	2,35	0,47	0,33	0,24	0,19	0,15	0,12	0,10	0,09	0,08	0,07	0,06	0,06	0,05	0,05	0,05	0,04	0,04	0,04	0,04	0,03
	0,25	2,56	0,51	0,36	0,26	0,20	0,16	0,13	0,11	0,10	0,09	0,08	0,07	0,06	0,06	0,06	0,05	0,05	0,05	0,04	0,04	0,03
	0,28	2,87	0,57	0,40	0,29	0,23	0,18	0,15	0,12	0,11	0,10	0,09	0,08	0,07	0,07	0,06	0,06	0,05	0,05	0,05	0,05	0,03
	0,30	3,07	0,61	0,43	0,32	0,24	0,19	0,16	0,13	0,12	0,10	0,09	0,08	0,08	0,07	0,07	0,06	0,06	0,05	0,05	0,05	0,04
	0,33	3,38	0,67	0,47	0,35	0,27	0,21	0,17	0,15	0,13	0,11	0,10	0,09	0,08	0,08	0,07	0,07	0,06	0,06	0,06	0,05	0,04

Figure 4.7 In the matrix above the steepness factors are indicated for each wave state of the scatter diagram.

Influence of the non-linear hydrostatic behavior on the AEP

The influence of the non-linear hydrostatic restoring moment is practically negligible.

4.1.3 Strategy B - Time series

The damping c_c and the stiffness coefficients k_c are varied. The two coefficients are optimized for each wave state by maximizing the average power absorbtion. The average power is increased by 20% from 0.2 [W] to 0.25 [W] compared with the control Strategy A. On the other hand the load factor decreases to 0.049. Note that the instantaneous power $P(t)$ can be negative, see Fig.

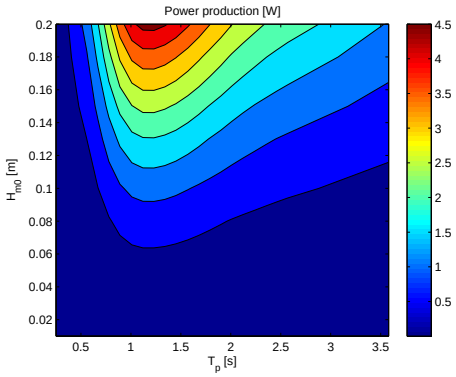

Figure 4.8 Power production for a linearly damped system, damping coefficient is optimized for each wave state.

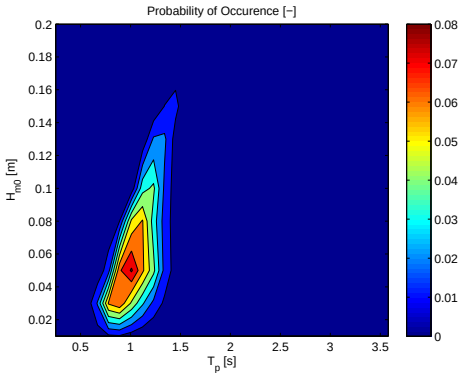

Figure 4.9 Probability of occurrence for Hanstholm scatter diagram.

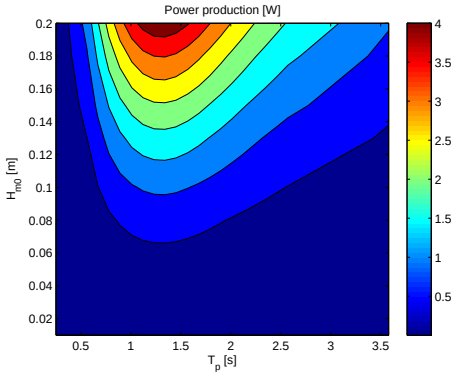

Figure 4.10 Power production matrix for the case where the damping coefficient is held constant.

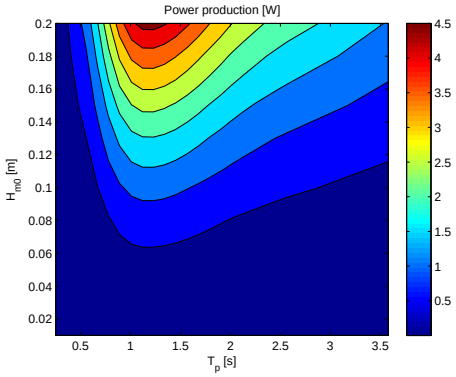

Figure 4.11 Power production matrix for a linearly damped system, damping coefficient is optimized for each wave state. The annual energy production is increased by 7 %.

4.25 indicating that energy is feed into the system. The negative spring stiffness must be taken into account for the calculation of the average power, thus it is reasonable to talk about a net-energy from the point on when power is feed into the system. The surface plots below show the optimum average power in function of the two control parameters for the different wave series. The increase in power production is considerably higher than for the previous waves i.e. 72%, the load factor decreases and is now 0.0159 (-67%). Note the two different shapes of the power surface. For peak periods away from the natural period the surface turns out to be more peaky. The negative pto-stiffness increases due to the fact that more energy is needed to force the oscillator to resonate with the incoming waves. The optimal damping coefficient decreases. The two latter facts are relatively disadvantageous for the present wave energy converter. Reactive control applied to a point absorber results in a system which is highly sensible to changes of the optimal control coefficients. A small change of the pto-stiffness k_c will significantly reduce the power for the situation where the wave period is away from the natural period. If the peak period is close to the natural period the power surface plot is more smoothed.

Hence, it is important to know for what purpose reactive control is applied. A differentiation could be as follows: i) in the first case one could be interested in maximizing the power for each wave state, on the other hand it could be beneficial to choose a strategy to maintain a constant capture width ratio, lets say for the majority of the wave states, by changing the natural period of the system. It is probably clear that, applying a negative spring is always connected with feeding in electrical power. Another method could be to passively change the mass moment of inertia by introducing a moveable mass a long the brace arm.
The load factor compared with other renewable energy technologies is normally in the range of 0.1 -0.6. For WEPTOS, a load factor of 0.3 was measured during tank testing, assuming constant/linear damping.

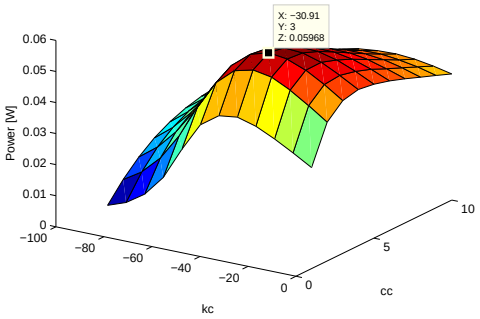

Figure 4.12 Average power in function of the damping and the stiffness coefficient - IRA1

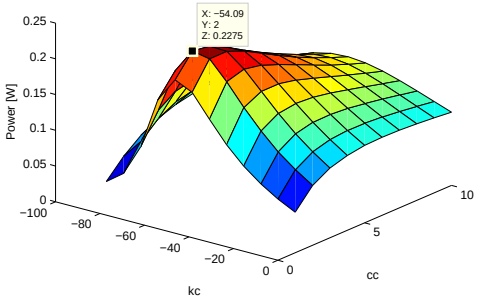

Figure 4.13 Average power in function of the damping and the stiffness coefficient - IRA2

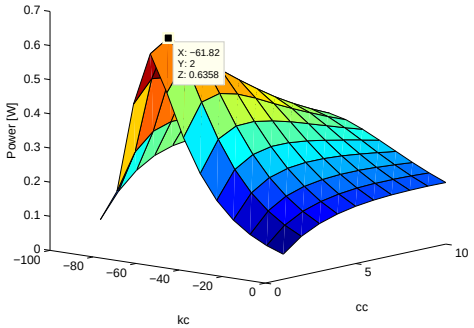

Figure 4.14 Average power in function of the damping and the stiffness coefficient - IRA3

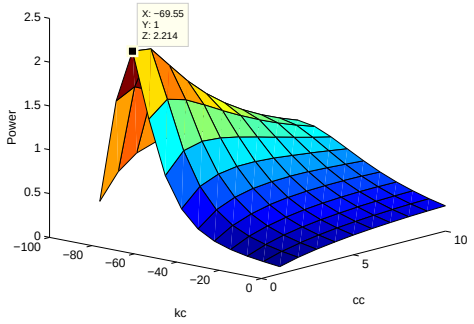

Figure 4.15 Average power in function of the damping and the stiffness coefficient - IRA4

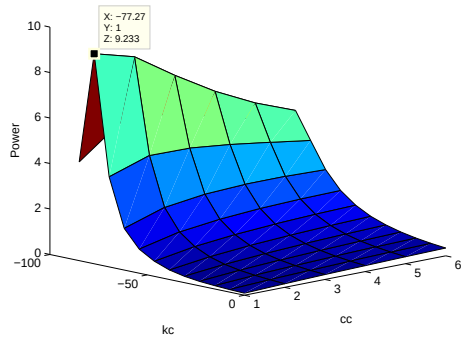

Figure 4.16 Average power in function of the damping and the stiffness coefficient - IRA5

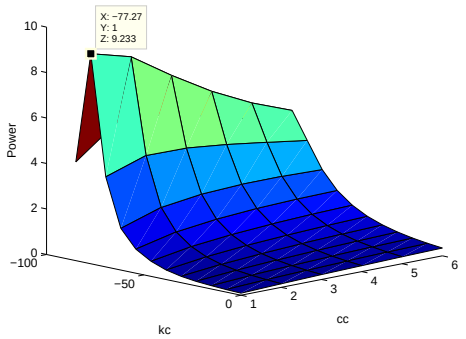

Figure 4.17 Average power in function of the damping and the stiffness coefficient - IRA5

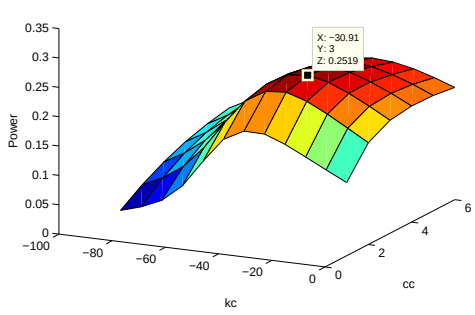

Figure 4.18 Average power in function of the damping and the stiffness coefficient - IRB1

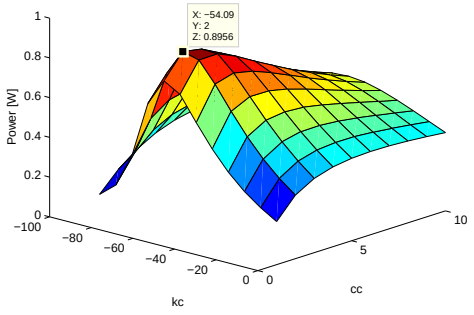

Figure 4.19 Average power in function of the damping and the stiffness coefficient - IRB2

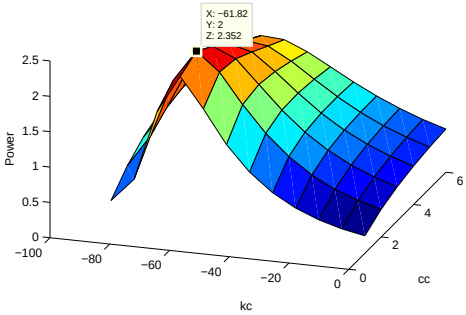

Figure 4.20 Average power in function of the damping and the stiffness coefficient - IRB3

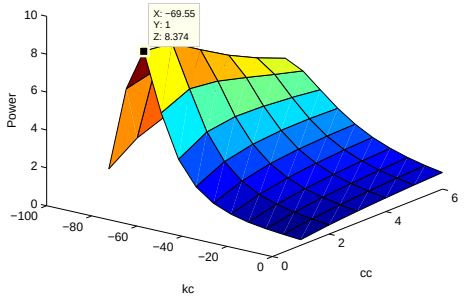

Figure 4.21 Average power in function of the damping and the stiffness coefficient - IRB4

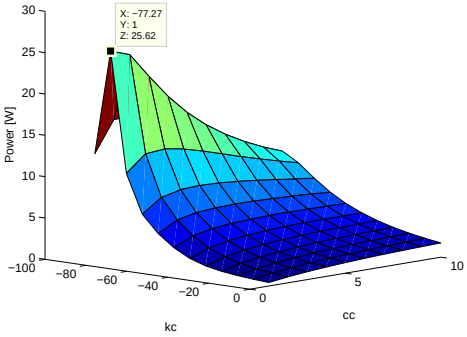

Figure 4.22 Average power in function of the damping and the stiffness coefficient - IRB5

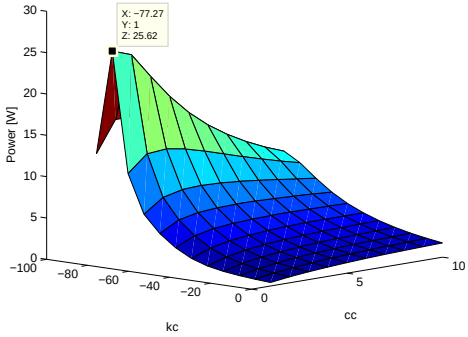

Figure 4.23 Average power in function of the damping and the stiffness coefficient - IRB5

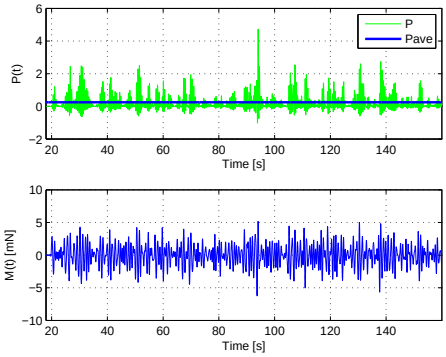

Figure 4.24 Average power in function of the damping and the stiffness coefficient - IRB5

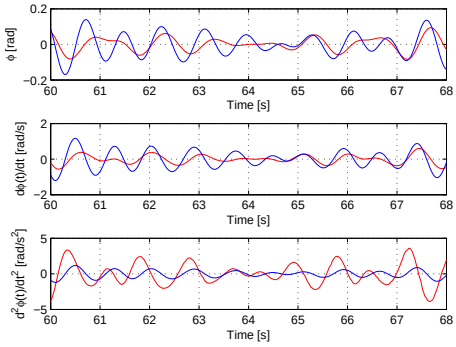

Figure 4.25 Strategy B, $m_c = 0$, $c_c = 3Nm/rad/s$, $k_c = -31.94Nm/rad$, $b_c = 0$, for the waves IRB1

Annual energy production applying reactive control

In this section the energy production is calculated by including a reactive control strategy. The spring stiffness is calculated for each peak frequency which appears in the scatter diagram. This control strategy enforces the motions of the WEC to be in phase with the incoming waves without the need for wave prediction. However the control strategy is still considered to be linear as long as no amplitude or force constraints are implemented.
It must be noted that by introducing a force or amplitude constraint the oscillator becomes out of phase again and the energy production is reduced. On the other hand if there are no force or amplitude constraints, the displacements i.e. the rotations will become too high and the float will rise out of the water and hence the linear fluid-structure interaction would not be valid any more. In the following two graphs the velocity and the wave excitation force are compared for two different control strategies: i) In the left graph, reactive control has been applied, the damping and stiffness coefficient were optimized for the particular wave state i.e. for a peak period of $T_p = 1.45sec.$ by a two-parameter optimization algorithm, the calculation has shown that the optimal control parameters are: $c_c = 2Nm/rad/s$ and $k_c = -49.3Nm/rad$. These values may change slightly if the intervals of the the optimization algorithm is refined. Note that the velocity and excitation moment is almost in phase. ii) on the right side the situation is somehow more unfavorable regarding the energy absorbtion. Only passive damping is applied, i.e. no reactive control, the velocity and the excitation moment are out of phase. The amplitude of the velocity is approximately three times smaller than in the previous case i).

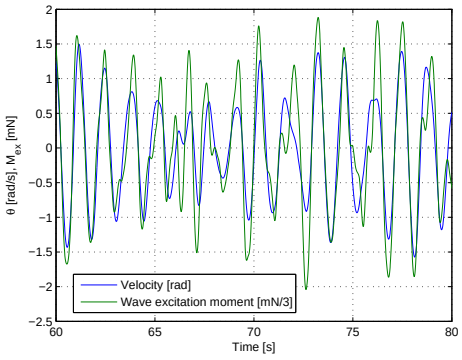

Figure 4.26 The blue curve is the velocity of the buoy whereas the green curve is the wave excitation moment divided by a factor of 3, $H_{m0} = 0.05m$, $T_p = 1.45sec$ applying reactive control, $P_{ave} = 0.541W$.

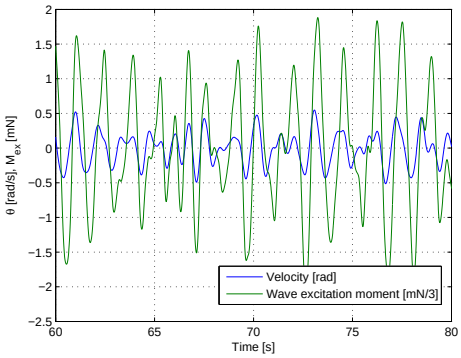

Figure 4.27 Velocity and wave excitation moment out of phase, $H_{m0} = 0.05m$, $T_p = 1.45sec$, applying passive control, $P_{ave} = 0.2714W$.

PTO-load constraint

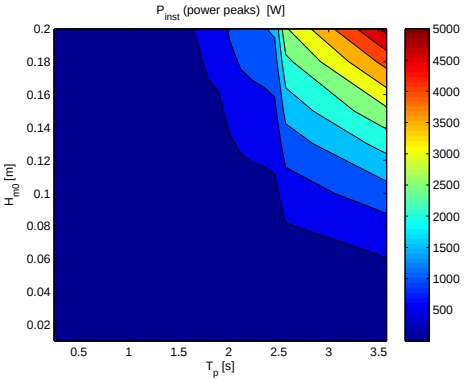

Figure 4.28 Average power matrix applying reactive control including a PTO-load constraint, the annual energy production is estimated to be $0.6103W$, i.e. an increase of 11 $\%$.

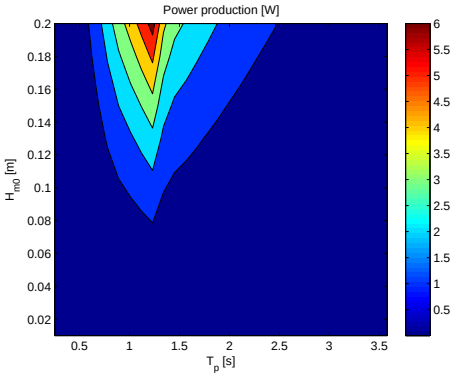

Figure 4.29 Instantanous maximum peaks for each wave state - no constraint.

4.1.4 Strategy C

We assume that the wave excitation moment $M_e(t)$ is completely observable from measurements of the sea-state elevation $\eta(t)$, the following sub-optimal control law was implemented:

$$M_c(t) = -J\,\ddot{\theta}(t) + 2c_c\,\dot{\theta}(t) - R\,\theta(t) \tag{4.2}$$

where $m_c = -J$, c_c replaced by $2c_c$, $k_c = -R$. The derivative gain factor $2c_c$ is determined by an optimality criterion for the absorbed mean power of the control force under the given sea-state:

$$c_c = \int_0^\infty \rho_{M_e M_e}(u) h_{r\dot{\theta}}(u)\,du \tag{4.3}$$

$\rho_{M_e M_e}(\tau)$ denotes auto-correlation coefficient function for the wave excitation moment, cf. Eqn.(61).

The average power becomes:

$$P_{abs} = \frac{1}{T}\int_0^T (m_c\ddot{\theta}(t) + c_c\dot{\theta}(t) + k_c\theta(t))\dot{\theta}(t)dt \tag{4.4}$$

In Figure 4.30 the velocity is plotted in blue and the wave excitation force is plotted in red. The velocity of the float is nearly in phase with the excitation force. In this case a large amount of wave excitation force can be transformed into electrical energy. However still a small phase difference is present.

<clearpage

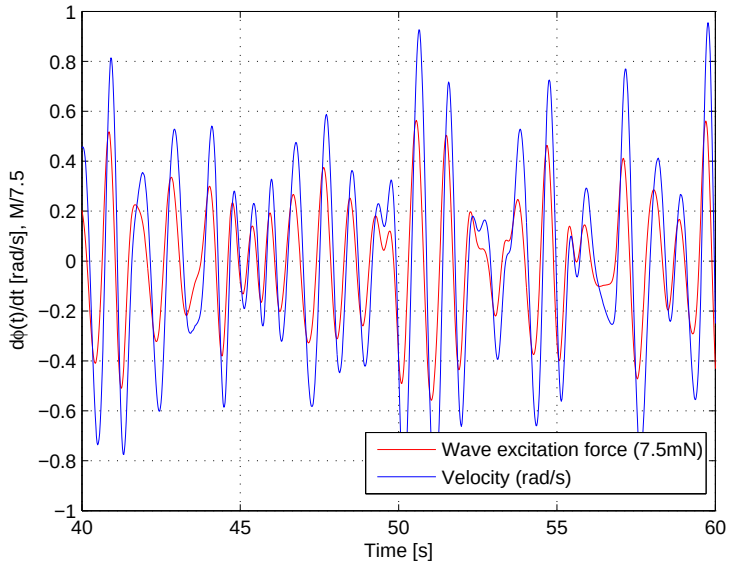

Figure 4.30 Velocity of the float in blue line and the wave excitation force in red line are in phase with each other.

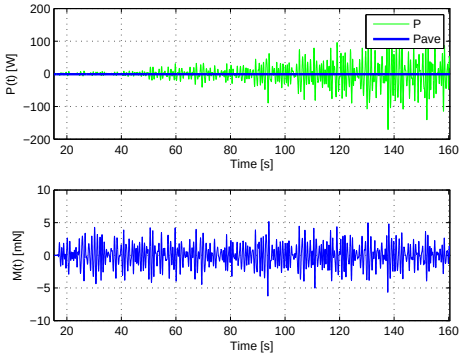

Figure 4.31 Strategy C, $m_c = -1.1$, $c_c = 1.97Nm/rad/s$, $k_c = -87.04Nm/rad$, $b_c = 0$, for the waves IRB1

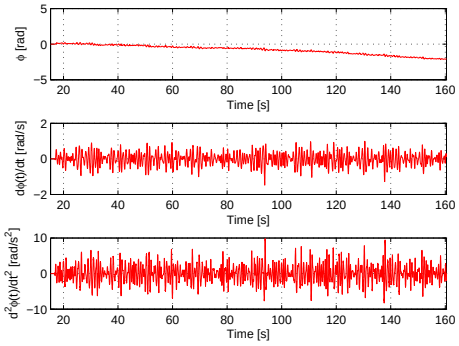

Figure 4.32 Strategy C, $m_c = -1.1$, $c_c = 1.97Nm/rad/s$, $k_c = -87.04Nm/rad$, $b_c = 0$, for the waves IRB1

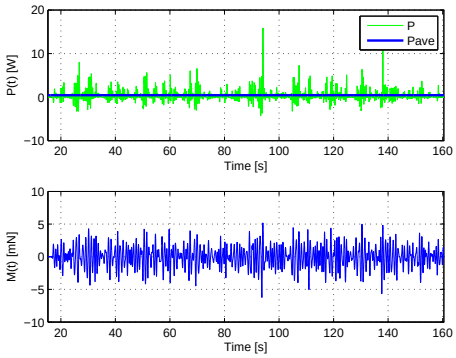

Figure 4.33 Strategy C, $m_c = -1.1$, $c_c = 1.97Nm/rad/s$, $k_c = -76.4Nm/rad$, $b_c = 0$, for the waves IRB1

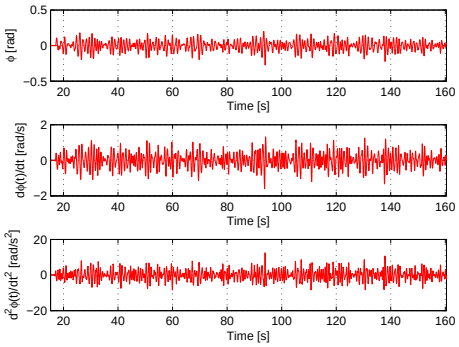

Figure 4.34 Strategy C, $m_c = -1.1$, $c_c = 1.97Nm/rad/s$, $k_c = -76.4Nm/rad$, $b_c = 0$, for the waves IRB1

4.1.5 Strategy D

Strategy D involves all the components in the control moment namely $m_c = -J$, c_c is replaced by $2c_c$, $k_c = -R$ and $h_{c\dot{\theta}}(t) = -h_{r\dot{\theta}}(t)$. The derivative gain factor $2c_c$ is determined by an optimality criterion for the absorbed mean power of the control force under the given sea-state, see Eqn. 3.4. Under this condition the applied control law enforces the absorber into phase with the wave excitation moment.
The optimal damping value is calculated by means of a stochastic analysis of the given wave elevation data.
For practical applications optimal control comes along with quiet a number of uncertainties. First of all the prediction of the incoming waves is difficult to obtain and for most cases inaccurate when dealing with real-sea waves. For the present case no future information of the wave state is required which indicates that the control strategy is causal. For the case where the float is oscillating close to its resonance period the motion rotation of the brace is very large and may be unrealistic. In reality the displacement and the power take off force is restricted by i) the geometry of the device and ii) characteristics of the power take off system.
In (Li 2011) an end-stop system is included which limitates the heave displacement at a certain level. The method which is used is as simple as introducing another stiffness-damper system on top of the power take off which is able to damp the extreme motions. By applying reactive control a very high pto force is required. The generated force is often much higher than the linear generator can provide thus the pto force needs to be restricted as well. The paper of (Li 2011) describes a simulation of the reactive causal control with displacement limits and then a method of choosing an appropriate limit on the available power take off force. The model is build in Simulink.

The numerical values for Strategy D for all the ten wave states are given in Table 4.14.

Table 4.13 Control strategy D, resonance condition

Strategy C	m_c $[Nm/rad/s^2]$	c_c $[Nm/rad/s]$	k_c $[Nm/rad]$	b_c [-]	$P_{c,\mathrm{opt}}$ $[W]$	cc_{JS} $[Nm/rad/s]$	P_{wave} $[W/m]$	η [-]
IRA1	-1.36	2.026	-86	1	0.0872	2.014	0.47	0.729
IRA2	-1.36	1.601	-86	1	0.3273	2.626	1.30	0.995
IRA3	-1.36	1.300	-86	1	0.8898	1.323	2.73	1.281
IRA4	-1.36	0.951	-86	1	3.140	0.929	7.94	1.557
IRA5	-1.36	0.595	-86	1	16.925	0.616	30.48	2.186
IRB1	-1.36	1.971	-86	1	0.3567	2.014	1.88	0.746
IRB2	-1.36	1.579	-86	1	1.2858	1.626	5.18	0.976
IRB3	-1.36	1.276	-86	1	3.265	1.323	10.94	1.175
IRB4	-1.36	0.932	-86	1	11.916	0.929	31.75	1.478
IRB5	-1.36	0.651	-86	1	48.659	0.616	115.25	1.662

Inserting $\sigma^2_{M_e} = \kappa_{M_e M_e}(0)$ into equation of the autocorrelation function we get the following expression for the optimal power absorbtion:

$$\bar{P}_{c,\mathrm{opt}} = \frac{1}{4c_c} \int_0^\infty |H_{e\eta}(\omega)|^2 \, S_{\eta\eta}(\omega) \, d\omega \tag{4.5}$$

A reformulation of the equation introduced in Chapter 2 gives the following equation to express the non dimensional performance index. The numerical values are given in Table 4.14.

$$\eta^* = \frac{1}{4c_c \rho g D} \frac{\int_0^\infty |H_{e\eta}(\omega)|^2 \, d\omega}{\int_0^\infty c_g(\omega) d\omega} \tag{4.6}$$

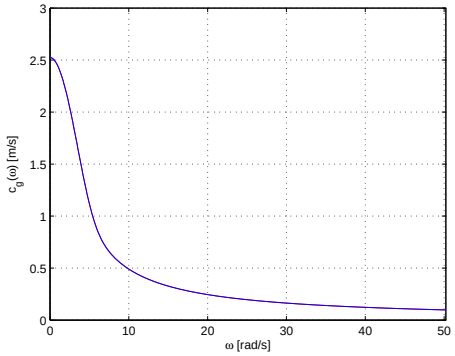

Figure 4.35 Excitation moment $H_{e\eta}(\omega)^2$

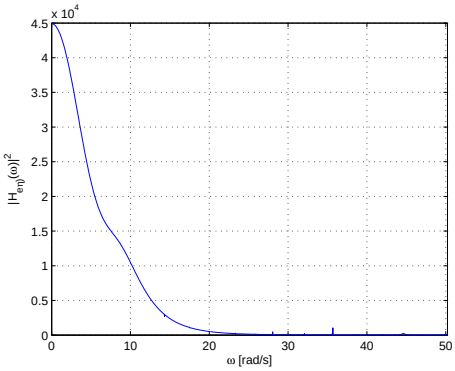

Figure 4.36 Group velocity c_g

Table 4.14 Control strategy D, resonance condition

Strategy D	P_{opt} $[W]$	η $[-]$	η^* $[-]$
IRA1	0.087	0.917	0.6815
IRA2	0.327	1.098	0.8624
IRA3	0.890	1.117	1.0614
IRA4	3.140	2.052	1.4519
IRA5	16.92	4.621	2.3207
IRB1	0.357	0.924	0.7005
IRB2	1.286	0.957	0.8745
IRB3	3.265	1.187	1.0821
IRB4	11.916	2.050	1.4815
IRB5	48.659	3.730	2.1210

Bibliography

Budal, Falnes J., K. (1975). A resonant point absorber of ocean-wave power. *Nature.* **256**, 478–479. With corrigendum in Vol. 257, p.626.

Cummins, W.E. (1962). The impulse response function and ship motions. *Schiffstechnik* **9**, 101–109.

Evans, D.V. (1976). A theory for wave power absorbtion by oscillating bodies. *J. Fluid Mechanics* **77**(1), 1–25.

Falnes, J. (1995). On non-causal impulse response functions related to propagating water waves. *Applied Ocean Research* **17**, 379–389.

Falnes, J. (2007). A review of wave-energy extraction. **20**(4), 185–201.

Haskind, M.D. (1953). Oscillation of a ship on a calm sea. *Society of Naval Architects and Marine Engineers*.

Li, Crozier R. Macpherson E., Bin. (2011). Reactive causal control of a linear generator in irregular waves for wave power systems.

Margheritini, L. (2012). Review on available information on waves in the danwec area. Techical Report 135, Dept. of Civil Eng., Aalborg University.

Matlab (2012). *Matlab Reference Guide*. Natick, MA, USA: The MathWorks.

Mei, C.C. (1976). Maximum wave-power absorbtion under motion constraints. *J. of Ship Research* **20**.

Neumann, F., Winands, V., and Sarmento, A.J.N.A. (2008). Pico shoreline OCW: status and new perspectives. *Proc., 2th Annual Int. Conf. on Ocean Energy (ICOE)*.

Nielsen, Sichani M.T. Kramer M.M. Kofoed J.P., S.R.K. (2012). Optimal control of power outtake of wave energy point absorbers. Technical report, Lectures Notes for a PhD course.

Næsee, Moan T., A. (2012). *Stochastic dynamics of marine structures*.

Ochi, M. K. (1990). *Applied Probability and Stochastic Processes*. John Wiley and Sons.

Perez, T. and Fossen, T. I. (2009). A matlab tool for parametric identification of radiation-force models of ships and offshore structures. **30**(1), 1–15.

Salter, S.H. (1974). Wave power. *Nature* **249**, 720–724.

S.R.K. Nielsen, M.M. Kramer B. Basu Z. Zhang., Q. Zhou (2012). Optimal control of nonlinear wave energy point converters. *Ocean Engineering*.

Taghipour, Arswendy A., R. (2008). Structural analysis of a multi-body wave energy converter in the frequency domain by interfacing wamit and abaqus. *International Conference on Offshore Mechanics and Artic Engineering, Estoril, Portugal*.

WAMIT (2012). *WAMIT Manual*. Chestnut Hill, Massachusetts, USA: WAMIT INC.

Wavelab (2012). *Wavelab Manual*.

APPENDIX A
Extended abstract

Title: Numerical time integration methods for a point absorber wave energy converter.

Published in
The 27th International Workshop on Water Waves and Floating Bodies
IWWWFB, 22-25 April 2012, Ingeniørhuset, Copenhagen.

The paper can be downloaded on the following official website of the Workshop:
http://www.iwwwfb.org/Workshops/27.htm

Numerical time integration methods
for a point absorber wave energy converter

A.S. Zurkinden[1] & M.M. Kramer
Wave Energy Research Group,
Department of Civil Engineering,
Aalborg University,
email: az@civil.aau.dk, mts@civil.aau.dk

Keywords: Wave energy converters, point absorber, time integration, state-space model, nonlinear hydrostatic behavior.

1 Background

The objective of this abstract is to provide a review of models for motion simulation of marine structures with a special emphasis on wave energy converters. The time-domain model is applied to a point absorber system working in pitch mode only. The device is similar to the well-known Wavestar float located in the Danish North Sea. The main objective is to produce a tool that can accurately simulate the dynamics of a floating structure with an arbitrary geometry provided the frequency domain coefficients are calculated beforehand. The latter calculation is based on linear fluid structure interaction (small deformations of the fluid surface and body), inviscid incompressible, irrotational flow and a linearized Euler-Bernoulli formulation of the fluid pressure.
The time-domain analysis of a floating structure involves the calculation of a convolution integral between the impulse response function of the radiation force and the unknown body velocity due to an external force. The convolution integral can be seen as a memory effect where the system response in the past affects the response in the future. Two different time-domain models will be presented. The first one is based on a discretization of the convolution integral. The calculation of the convolution integral is performed at each time step regardless of the chosen numerical scheme. In the second model the convolution integral is replaced by a system of linear ordinary differential equations. The formulation of the state-space model is advantageous regarding the computational effort and the robustness of the solver. Another important feature is the linear-time invariance of the system. In a next step the influence of the nonlinear hydrostatic behavior of the float is investigated by using a simplified formulation.

2 Problem formulation

2.1 Truncation of the convolution integral

The equation of motion for the analyzed geometry can be formulated by a momentum equilibrium condition around the fixed point, see Fig. 1, which leads to the following equation:

$$(M_{44} + a_{44}^{\infty})\ddot{\varphi}_4(t) + \int_0^t K_{44}(t-\tau)\dot{\varphi}_4(\tau)d\tau + C_{44}\varphi_4(t) + c^{pto}\dot{\varphi}_4(t) = \int_{-\infty}^{\infty} h_4(t-\tau)\eta(t)d\tau \qquad (1)$$

Pitch $\varphi_4(t)$ is the corresponding degree of freedom around the bearing, indicated with the indices $i = 4$, $j = 4$. M_{44} corresponds to the mass moment of inertia, a_{44}^{∞} is the added mass at infinite high frequencies, $K_{44}(t)$ is the impulse response function of the radiation force, C_{44} is the hydrostatic stiffness coefficient, c^{pto} is a constant damping coefficient, representing the linear power take off system, $h_4(t)$ is the impulse response function of the excitation force and $\eta(t)$ corresponds to the

[1]presenting author

surface elevation. The impulse response function of the radiation force can be seen as the system identity. If we know the response to an impulse, then we know the response to any excitation by convolution with the impulse response function. The basic work for this formulation of the problem was laid by W.E. Cummings (1962) [1]. The convolution integral in Eqn. 1 can be expressed by means of a sum:

$$\int_0^t K_{44}(t-\tau)\dot{\varphi}_4(\tau)d\tau = \Delta t \sum_{\tau=0}^{t} K_{44}(t-\tau)\dot{\varphi}_4(\tau) \tag{2}$$

Expanding the sum in Eqn. 2, we get the following expression:

$$\Delta t \sum_{\tau=0}^{t} K_{44}(t-\tau)\dot{\varphi}_4(\tau) = \Delta t[K_{44}(t)\dot{\varphi}_4(0) + K_{44}(t-1)\dot{\varphi}_4(1) + ... + K_{44}(0)\dot{\varphi}_4(t)] \tag{3}$$

The equation of motion can then be written:

$$(M_{44}+a_{44}^{\infty})\ddot{\varphi}_4(t)+K_{44}(0)\dot{\varphi}_4(t)+C_{44}\varphi_4(t)+c^{pto}\dot{\varphi}_4(t) = \int_{-\infty}^{\infty} h_4(t-\tau)\eta(t)d\tau - \int_0^{t^-} K_{44}(t-\tau)\dot{\varphi}_4(\tau)d\tau \tag{4}$$

The numerical integration of Eqn. 4 only requires the calculation of the integral at the preceding time-steps and can therefore be considered as a known quantity. A fourth order Runge Kutta scheme with a constant time step Δt has been used to evaluate the linear equation of motion given in Eqn. 4. Drawbacks of this method are *i)* time consuming *ii)* the convolution integral needs to be calculated at each time step *iii)* the impulse response function needs to be interpolated with the same Δt as the time integration, which is not very convenient. The results are shown in the last page of this abstract. Fairly good agreement can be observed when comparing the numerical discretization of the convolution integral with an analytical calculation for regular waves, i.e. when a constant damping coefficient can be assumed.

2.2 Rational approximation to the radiation force

In this section a method is applied to circumvent the drawbacks of the discretization, presented in the previous chapter. The convolution integral is replaced by an equivalent system of coupled first order differential equations, which are solved along with the equations of motion of the absorber, S.R.K Nielsen [2]. The method is based on an initial replacement of the actual frequency response function of the floating body $H_{r\dot{\varphi}_4}(\omega)$ which was calculated by the software WAMIT, [3]. The approximating rational function is given in the form

$$\left.\begin{aligned} H_{r\dot{\varphi}_4}(s) \approx \frac{P(s)}{Q(s)} = \frac{p_0 s^{m-1} + p_1 s^{m-1} + ... + p_{m-1}s}{s^n + q_1 s^{n-1} + ... + q_n} \end{aligned}\right\} \quad s = i\omega \tag{5}$$

The unknowns are the coefficients of polynomials P and Q. The parameters p_0, p_1,..., p_{m-1} and q_0, q_1,..., q_n denotes the *poles* and the *zeros* of the rational approximation and are all real. The order of the filter as given by the pair n, m may be chosen freely with the only restriction that $m \leq n$. A rational causal approximation for $H_{r\dot{\varphi}_4}$ can be obtained by the MATLAB *control toolbox* [4] or the *MSS FDI toolbox* [5]. Next, the convolution integral is approximated with the product of the constants p_0, p_1,..., p_{m-1} and the new unknowns i.e the additional state vectors $I(t)$.

$$\int_0^t K_{44}(t-\tau)\dot{\varphi}_4(\tau)d\tau \approx \left[\begin{array}{cccc} p_0 & p_1 & \ldots & p_{m-1} \end{array}\right] I(t) \tag{6}$$

where the time derivation of $I(t)$ is given as follows:

$$\dot{I}(t) = \left[\begin{array}{cccc} -q_1 & -q_2 & -q_3 & q_n \\ 1 & 0 & 0 & 0 \\ 0 & 1 & 0 & 0 \\ 0 & 0 & 1 & 0 \end{array}\right] I(t) + \left[\begin{array}{c} 1 \\ 0 \\ 0 \\ 0 \end{array}\right] \dot{\varphi}_4(t) \tag{7}$$

We are now able to approximate the convolution integral of the radiation force by inserting Eqn. 6 into Eqn. 1. As a result we end up in having a time-invariant system for the radiation force which is advantageous regarding computational time and storage requirements.

$$(M_{44} + a_{44}^{\infty})\ddot{\varphi}_4(t) + \left[\begin{array}{cccc} p_0 & p_1 & \ldots & p_{m-1} \end{array}\right] I(t) + C_{44}\varphi_4(t) + c^{pto}\dot{\varphi}_4(t) = \int_{-\infty}^{\infty} h_4(t-\tau)\eta(t)d\tau \tag{8}$$

2.3 Nonlinear hydrostatic behavior

The change of the hydrostatic pressure at each instantaneous position of the float below the water plane can be characterized by taking into account a nonlinear hydrostatic behavior. This effect can be observed at the two extremities of the red curve, see Fig. 2. On the upper left corner, the float successively dips into the water and on the lower right end of the curve the float starts to be fully submerged by the water. In between, the derivation of the wetted surface is small, hence a linear approximation of the hydrostatic moment becomes justifiable. The red curve is a result of experiments which were carried out at the Hydraulic Laboratory at Aalborg University. In the following model a simplified formulation of the nonlinear hydrostatic effect is presented, where the red curve is approximated by a piecewise trilinear curve, see Fig. 2. The nonlinear force is computed by implementing a displacement control algorithm, i.e. it is assumed that the wave amplitude is zero in the vicinity of the float.

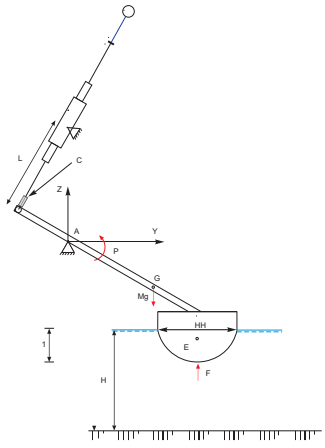

Figure 1: *Wavestar lab model, froude scaled 1:20*

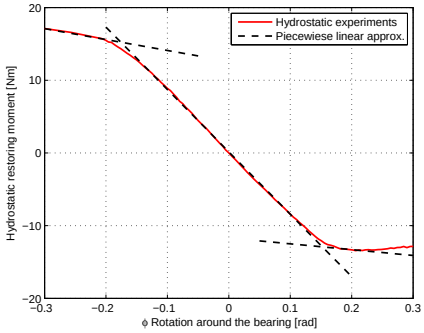

Figure 2: *Hydrostatic restoring moment, piecewise linear approximation*

3 Results: Wavestar float - lab model scale 1:20

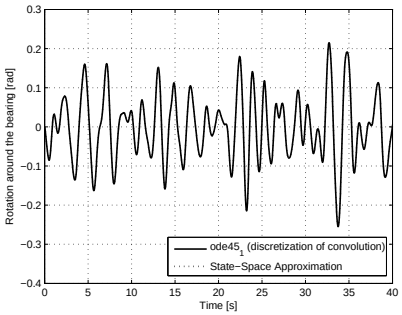

Figure 3: *Body response under panchromatic wave excitation, $H = 0.1m$, $T = 2.1s$*

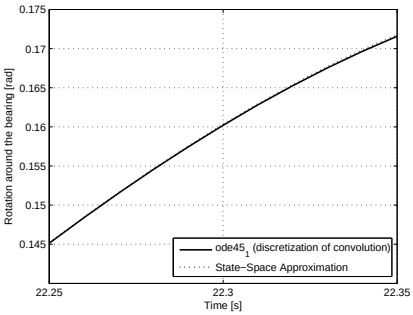

Figure 4: *Body response under panchromatic wave excitation, $H = 0.1m$, $T = 2.1s$, zoom*

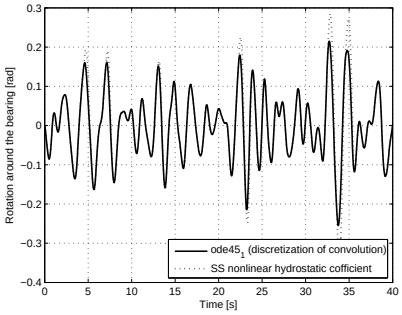

Figure 5: *Non linear hydrostatic, simplified implementation*

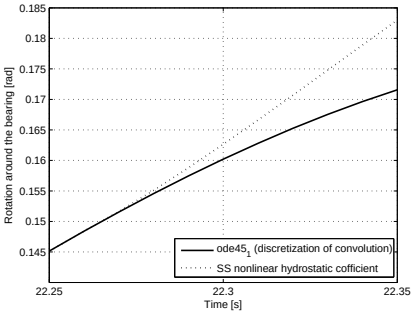

Figure 6: *Non linear hydrostatic, simplified implementation, zoom*

References

[1] Cummins, W.E. The impulse response functions and ship motions. Schiffstechnik. 1962 (9) 101-9

[2] Soeren, R.K. Nielsen. Structural Dynamics, Vol. 3. Dept. of Civil Eng., Aalborg University 2007, DCE Lecture Notes No. 11

[3] WAMIT Software. WAMIT User Manual, Version 7.0. WAMIT Inc.

[4] Control System Toolbox 9.1. A userguide for the control system toolbox 9.1 in Matlab. Matlab Help

[5] Perez, T., Fossen, T.I. A Matlab Tool for Parametric Identification of Radiation-Force Models of Ships and Offshore Structures. Modelling, Identification and Control, 2009 MCI-30(1) 1-15

APPENDIX B
Paper 1

Title: Comparison between numerical modeling and experimental testing of a point absorber WEC using linear power take-off system.

Published in
Proceedings of the ASME 2012 31st International Conference on Ocean,
Offshore and Artic Engineering,
OMAE 2012, June 10-15, 2012, Rio de Janeiro, Brazil.

Proceedings of the ASME 2012 31st International Conference on Ocean, Offshore and Artic Engineering
OMAE 2012
June 10-15, 2012, Rio de Janeiro, Brazil

OMAE2012-83692

COMPARISON BETWEEN NUMERICAL MODELING AND EXPERIMENTAL TESTING OF A POINT ABSORBER WEC USING LINEAR POWER TAKE-OFF SYSTEM

Andrew S. Zurkinden
Wave Energy Research Group
Departement of Civil Engineering
Aalborg University
9000 Aalborg, Danmark
Email: az@civil.aau.dk

Morten Kramer
Wave Energy Research Group
Departement of Civil Engineering
Aalborg University
9000 Aalborg, Danmark
Email: mmk@civil.aau.dk

Mahdi Teimouri
Wave Energy Research Group
Departement of Civil Engineering
Aalborg University
9000 Aalborg, Danmark
Email: mts@civil.aau.dk

Marco Alves
Wave Energy Centre
1000 Lisbon, Portugal
Email: marco@wave-energy-centre.org

ABSTRACT

Currently, a number of wave energy converters are being analyzed by means of numerical models in order to predict the electrical power generation under given wave conditions. A common characteristic of this procedure is to integrate the loadings from the hydrodynamics, power take-off and mooring systems into a central wave to wire model. The power production then depends on the control strategy which is applied to the device. The objective of this paper is to develop numerical methods for motion analysis of marine structures with a special emphasis on wave energy converters. Two different time domain models are applied to a point absorber system working in pitch mode only. The device is similar to the well-known Wavestar prototype located in the Danish North Sea. A laboratory model has been set up in order to validate the numerical simulations of the dynamics. Wave Excitation force and the response of the device for regular and irregular waves were measured. Good correspondence is found between the numerical and the physical model for relatively mild wave conditions. For higher waves the numerical model seems to underestimate the response of the device due to its linear fluid-structure interaction assumption and linearized equation of motion. The region over which the numerical model is valid will be presented in terms of non-dimensional parameters describing the different wave states.

1 Introduction

The idea of extracting energy from ocean waves is relatively old and many WECs have been proposed during the last decades [1]. These have initiated commercial WEC projects using devices such as different buoy concepts, Oscillating-Water-Column (OWC) plants like Pico [2], the Pelamis [3], overtopping WEC types like the Wave Dragon [4], the point absorber approach used for the SEAREV [5] and the Wave Star device [6], see Fig. 1. Oscillating devices and notably point absorbers constitute an important class of wave energy converters particularly with regard to offshore deployment.

The main objective of this paper is to produce a tool that can accurately simulate the dynamics of a floating structure with an

arbitrary geometry provided the frequency domain coefficients are calculated beforehand. The latter calculation is based on linear fluid structure interaction i.e. small deformations of the fluid surface and body, inviscid incompressible, irrotational flow and a linearized Euler-Bernoulli formulation of the fluid pressure. The time-domain analysis of a floating structure involves the calculation of a convolution integral between the impulse response function of the radiation force and the unknown body velocity. The convolution integral can be seen as a memory effect where the system response in the past affects the response in the future whereas the corresponding impulse response function is causal. Two different time-domain models will be presented. The first one is based on a discretization of the convolution integral [7] and [8]. The calculation of the convolution integral is performed at each time step regardless of the chosen numerical scheme. In the second model the convolution integral is replaced by a system of linear ordinary differential equations, [9] and [10]. The formulation of the state-space model is advantageous regarding the computational effort and the robustness of the solver [11]. Another important feature is the linear-time invariance of the system.

FIGURE 1. WAVESTAR PROTOTYPE DEVICE, TEST SITE IN HANSTHOLM, DENMARK

In order to compare the numerical results with measured data, a laboratory model has been set up. The experimental device is to some extent a reproduction of the Wavestar prototype device which is located out in Hanstholm off the Northwest coast of Denmark. The model is scaled to a factor of 1:20 compared to the prototype. It consists of a float which is attached to an arm and equipped with a linear power-take off system (PTO) based on the electromagnetic principle. It is well understood that the efficiency of a wave energy converter can be considerably improved by adopting a more advanced control strategy [12]. When a point absorber is left uncontrolled, the simplest but poorest way to optimize the power-take-off is to tune the natural frequency to a characteristic frequency in the local sea state such as the peak frequency in the wave spectrum at the site where the device will be deployed. Maximum power transfer between the wave and the device will occur, when the natural period of these coincides, so the absorber is oscillating at resonance, [1]. In turn, this means the velocity of the absorber is in phase with the excitation wave force at any time, and hence a maximum kinetic is supplied to the WEC. At excitation frequencies away the resonance frequency a phase difference is present, and the power outtake is correspondingly reduced. Evans [13] pointed out in 1976 that for heaving bodies, operating in resonance with the natural period of the waves may require negative applied springs due to the relative high inbuilt hydrostatic stiffness. Keeping this observation in mind, the following suboptimal control law has been used.

A feed-back force is introduced by the actuator to control the motions of the float in a way which maximizes the power absorption. Reactive control is applied by means of a proportional-derivative (PD) control algorithm. For monochromatic waves the optimal control law can be calculated in advance by maximizing the power function [14]. The latter assumption is only valid when the excitation force or at least its phase is known in advance at each time step. For irregular waves, on the other hand, the optimal control becomes non-causal [14] and [16]. For the present case a causal sub-optimal feed-back control law has been applied which is based on the assumption that a wave energy converter with favorable response characteristics in regular waves will be good in irregular waves as well. Thus the damping coefficients are optimized for a number of relevant sea states representing the Danish Sector of the North Sea. A common characteristic of applying reactive control to a wave energy converter is that the motions of the device can be damped or accelerated, or a combination of both by the feed-back force. In the latter case the controller i.e. the generator force transmits energy into the system in form of negative spring stiffness whereas in the former case, energy is absorbed by the damping coefficient. Regardless of the control strategy, any numerical model can simulate both cases with equal accuracy for the given range where linear fluid structure interaction can be adopted. When considering experimental tests or real sea tests the control situation becomes slightly more complex. By introducing negative spring stiffness the system becomes more sensitive to incoming waves hitting the body. As a result, slamming or wave overtopping effects occur more often. It is clear that these effects violate the assumptions in the numerical model stated above. However by introducing a negative spring stiffness the optimal damping coefficient can be decreased, whereas the power production is increased due to the increase of the bodies' velocity. Experiments on the prototype have shown that the net energy production for the cases where

negative spring stiffness was applied increased, [12]. The upper limit of this control strategy lies in the stroke restriction of the hydraulic cylinders or in the case of a linear generator by the strokes in the slider and the stator.
The present results were carried out for zero spring stiffness only. A more detailed study on the prototype applying negative spring stiffness can be found in [12].

2 The dynamic model

The equation of motion will be described for the single degree of freedom point absorber, equipped with a linear power take-off system, shown in Fig. 2. The lever arm is assumed to be infinitely rigid and is constrained to move around the fixed point A. The motion is positive in the counter clockwise direction. The equation of motion is obtained by formulating the momentum equilibrium condition around point A:

$$(M_{44}+a_{44}^{\infty})\ddot{\phi}_4(t)+\int_0^t K_{44}(t-\tau)\dot{\phi}_4(\tau)d\tau+C_{44}\phi_4(t) +M_c(t)=\int_{-\infty}^{\infty}h_{\phi 4}(t-\tau)\eta(\tau)d\tau \quad (1)$$

Pitch $\phi_4(t)$ is the corresponding degree of freedom around the bearing, indicated with the indices $i=4$, $j=4$. M_{44} corresponds to the mass moment of inertia around the fixed point of the float mass and the lever arm, a_{44}^{∞} is the added mass at infinitely high frequencies, $K_{44}(t)$ is the impulse response function of the radiation force, C_{44} is the hydrostatic stiffness coefficient, $M_c(t)$ represents the control force moment from the power take-off system, $h_4(t)$ is the impulse response function of the excitation force and $\eta(\tau)$ corresponds to the surface elevation of the waves. In the following experiment two-dimensional regular and irregular waves are considered, propagating in the positive y-direction relative to (x,y,z)-coordinate system defined in Fig. 2.
The impulse response function of the radiation force can be seen as the system identity. If we know the response to an impulse, then we know the response to any excitation by convolution with the impulse response function. The basic work for this formulation of the problem was laid by W.E. Cummins [17]. In the following section two approaches will be compared to solve the convolution integral in Eqn.(1).

2.1 Truncation of the convolution integral

The convolution integral in Eqn.(1) can be expressed by means of a sum:

$$\int_0^t K_{44}(t-\tau)\dot{\phi}_4(\tau)d\tau=\Delta t\sum_{i=0}^{m}K_{44}((m-i)\Delta t)\dot{\phi}_4(i\Delta t),t=m\Delta t \quad (2)$$

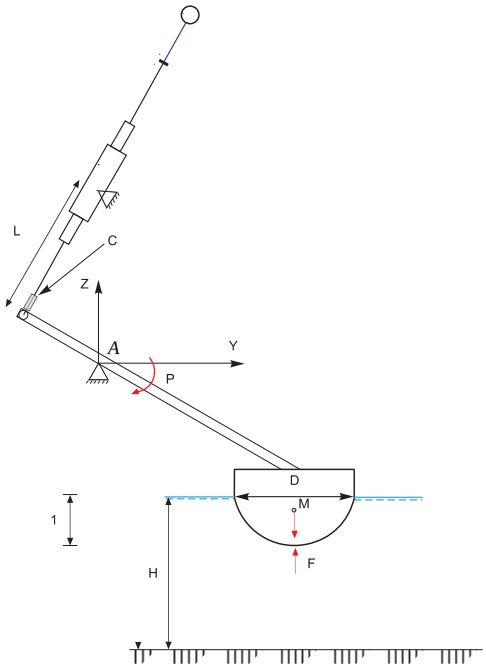

FIGURE 2. DEFINITION OF THE LABORATORY MODEL REPRESENTING THE WAVESTAR PROTOTYPE MODEL IN HANSTHOLM, REF. FIG. 1, STATIC REFERENTIAL STATE

TABLE 1. NUMERICAL VALUES OF THE LAB MODEL

Description:	Symbol:	Value:	Unit:
Mass of the float:	m_f	2.972	kg
Mass of the float arm:	m_{fa}	0.851	kg
Length of the float arm:	L	0.680	m
Diameter of the float:	D_o	0.254	m
Lever arm initial:	c	0.200	m
Piston displacement:	$l(t)$	*var.*	m
Mass moment of Inertia:	J	0.778	kgm^2
Hydrostatic stiffness:	r_h	86.00	Nm
Water depth:	h	0.650	m
Draught:	d	0.104	m
Wavelength:	λ	*var.*	m
Eigenfrequency:	ω_n	7.95	rad/s
PTO velocity gain:	c_c	*var.*	Ns/m

Equation (1) can be rearranged as:

$$(M_{44}+a_{44}^{\infty})\ddot{\phi}_4(t)+K_{44}(0)\dot{\phi}_4(t)+C_{44}\phi_4(t)+M_c(t) = \int_{-\infty}^{\infty} h_4(t-\tau)\eta(t)d\tau - \int_0^{t^-} K_{44}(t-\tau)\dot{\phi}_4(\tau)d\tau \quad (3)$$

The right hand side of Eqn.(3) only requires calculation of the integral at the preceding time-steps and can therefore be considered as a known quantity. A fourth order Runge Kutta scheme with a constant time step has been used to evaluate the linear equation of motion given in Eqn.(3). The drawbacks of this method are i) it is time consuming, ii) the convolution integral needs to be calculated at each time step, iii) the impulse response function needs to be interpolated with the same time step as the time integration, which is not very convenient. In Fig. 4 two independent solutions are given for the rotational displacement subjected to irregular waves. Note that the damping coefficient is zero for the sake of comparison of the two solvers.

2.2 Rational approximation of the radiation force

The radiation force moment $M_r(t)$ is given, cf. Eqn. (1)

$$M_r(t) = -a_{44}^{\infty}\ddot{\phi}_4(t) - M_{r,0}(t) \quad (4)$$

where

$$M_{r,0}(t) = \int_0^t K_{44}(t-\tau)\dot{\phi}_4(\tau)d\tau \quad (5)$$

The idea in this section is to replace the convolution integral by an equivalent system of coupled first order differential equations, which are solved numerically along with the equations of motion of the absorber. The method is based on an initial replacement of the actual frequency response function $H_{r\dot{\phi}_4}(\omega)$ with an approximating *rational function* $\tilde{H}_{r\dot{\phi}_4}(\omega)$ given in the form

$$\tilde{H}_{r\dot{\phi}_4}(s) = \frac{P(s)}{Q(s)} = \frac{p_0 s^m + p_1 s^{m-1} + ... + p_{m-1}s + p_m}{s^n + q_1 s^{n-1} + ... + q_{n-1}s + q_n}\Bigg\} s = i\omega \quad (6)$$

The unknowns are the coefficients of polynomials P and Q. The parameters p_0,p_1,...,p_{m-1},p_m and q_1,...,q_{n-1} q_n define the *poles* and the *zeros* of the rational approximation and are all real. The order of the filter as given by the pair (n,m) may be chosen freely with the only restriction that $m \leq n$, and that all poles have negative real part, i.e.

$$Re(p_j) < 0, \qquad j = 1, ..., n \quad (7)$$

Eqn. (7) ensures that the filter is *stable* and *causal*. Correspondingly, the indicated approach only applies to frequency response functions. A rational causal approximation for $H_{r\dot{\phi}_4}$ can be obtained by the *MATLAB control toolbox* [18] or the *MSS FDI toolbox* [11]. Next, the convolution integral $M_{r,0}(t)$ is obtained as output of the following system of differential equations:

$$M_{r,0}(t) = p_0\frac{d^m y}{dt^m} + p_1\frac{d^{m-1}y}{dt^{m-1}} + \cdots + p_{m-1}\frac{dy}{dt} + p_m y \quad (8)$$

$$\frac{d^n y}{dt^n} + q_1\frac{d^{n-1}y}{dt^{n-1}} + \cdots + q_{n-1}\frac{dy}{dt} + q_n y = \dot{\phi}_4(t) \quad (9)$$

where $y(t)$ is an auxiliary variable, which cannot be related with any physical interpretation. Eqn. (9) may be written in the following state vector form

$$\dot{\mathbf{z}}_r(t) = \mathbf{A}_r\,\mathbf{z}_r(t) + \mathbf{b}_r\dot{\phi}_4(t) \quad (10)$$

where:

$$\mathbf{z}_r(t) = \begin{bmatrix} y(t) \\ \frac{d}{dt}y(t) \\ \frac{d^2}{dt^2}y(t) \\ \vdots \\ \frac{d^{n-2}}{dt^{n-2}}y(t) \\ \frac{d^{n-1}}{dt^{n-1}}y(t) \end{bmatrix}, \quad \mathbf{b}_r = \begin{bmatrix} 0 \\ 0 \\ 0 \\ \vdots \\ 0 \\ 1 \end{bmatrix} \quad (11)$$

$$\mathbf{A}_r = \begin{bmatrix} 0 & 1 & 0 & \cdots & 0 & 0 \\ 0 & 0 & 1 & \cdots & 0 & 0 \\ \vdots & \vdots & \vdots & \ddots & \vdots & \vdots \\ 0 & 0 & 0 & \cdots & 0 & 1 \\ -q_n & -q_{n-1} & -q_{n-2} & \cdots & -q_2 & -q_1 \end{bmatrix} \quad (12)$$

Similarly, Eqn.(5) may be written on the vector form

$$M_{r,0}(t) = \mathbf{p}_r \, \mathbf{z}_r(t) \tag{13}$$

$$\mathbf{p_r} = \begin{bmatrix} p_m & p_{m-1} & \cdots & p_1 & p_0 & 0 & \cdots & 0 \end{bmatrix} \tag{14}$$

By rearranging the equations above the equation of motion can now be rewritten in a state space model as follows:

$$\frac{d}{dt}\mathbf{z}(t) = \mathbf{A}\mathbf{z}(t) + \begin{bmatrix} 0 \\ \frac{1}{(M_{44}+a_{44}^{\infty})} \\ \mathbf{0} \end{bmatrix} \int_{-\infty}^{\infty} h_{\phi 4}(t-\tau)\eta(\tau)d\tau \tag{15}$$

where

$$\mathbf{z}(t) = \begin{bmatrix} \phi_4(t) \\ \dot{\phi}_4(t) \\ \mathbf{z}_r(t) \end{bmatrix} \tag{16}$$

$$\mathbf{A} = \begin{bmatrix} 0 & 1 & \mathbf{0} \\ -\frac{C_{44}}{(M_{44}+a_{44}^{\infty})} & 0 & -\frac{1}{(M_{44}+a_{44}^{\infty})}\mathbf{p}_r \\ \mathbf{0} & \mathbf{b}_r & \mathbf{A}_r \end{bmatrix} \tag{17}$$

In Eqn.(15) the control moment $M_c(t)$ has been omitted. The method has been illustrated below for the absorber defined in Fig. 2 with the numerical values in Tab. 1, using the relatively low order filter $(m,n) = (4,5)$. In Fig. 3 the resulting frequency response function has been compared with the corresponding target frequency response function calculated by the BEM program WAMIT, [19]. Note that only the real part of the frequency response function has been displayed, i.e the hydrodynamic damping coefficient of the float. The two time integration methods were compared with each other. A constant time step of $\Delta t = 0.01s$ has been assumed for all the calculations. The wave excitation force is calculated for a JONSWAP spectrum with a significant wave height of $H_s = 0.1m$ and a peak period of $T_p = 2.1s$, the peak enhancement factor is $\gamma = 3.3$. It can be seen from Fig. 4 that the time domain implementation based on a state-space and a direct convolution evaluation give results of similar quality. Similar results were found by [7].

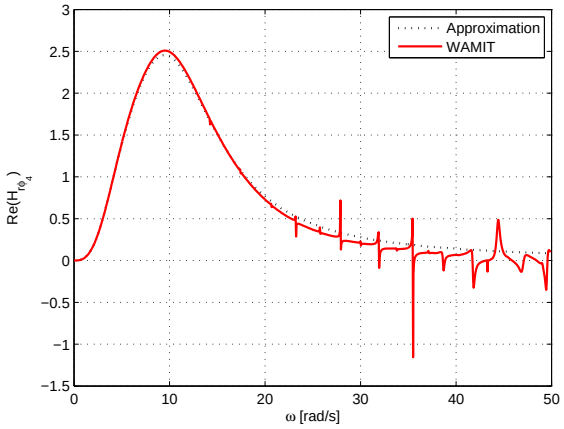

FIGURE 3. RATIONAL APPROXIMATION TO $Re(H_{r\dot{\phi}_4}(\omega))$ OF ORDER $(m,n) = (4,5)$

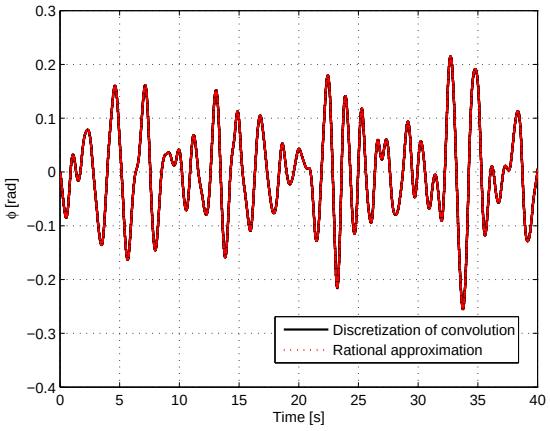

FIGURE 4. COMPARISON OF TWO TIME INTEGRATION METHODS FOR A JONSWAP SPECTRUM $(H_s = 0.1m, T_p = 2.1s)$, i) DISCRETIZATION OF THE CONVOLUTION INTEGRAL ii) RATIONAL APPROXIMATION OF THE CONVOLUTION INTEGRAL

2.3 Control moment

The control force moment $M_c(t)$ is work conjugated to the contraction of the piston arm BC and is used to control the motion of the WEC in a way that a maximum power outtake is obtained. The following rather general parameterized feed-back control law is presumed:

$$M_c(t) = m_c\ddot{\phi}_4(t) + c_c\dot{\phi}_4(t) + k_c\phi_4(t) + \int_{-\infty}^{\infty} h_{c\dot{\phi}_4}(t-\tau)\dot{\phi}_4(\tau)\, d\tau \tag{18}$$

m_c denotes the gain factor for the control force component proportional to the acceleration, c_c signifies the gain factor for

the control force component proportional to the velocity and k_c denotes the gain factor for the control force component proportional to the rotational displacement ϕ_4. In control theory the force components proportional to the displacement and the velocity are referred to as proportional and derivative control, respectively. m_c and k_c may attain positive as well as negative values. c_c is always positive in the present application. The last term in Eqn. (18) represents the weighted influence on the control force of previous and future velocities. Accordingly, the impulse response function is not causal. It should be noticed that for the practical implementation of the control law in the experiments m_c, k_c and $h_{c\dot{\phi}_4}$ has been set to be zero for the present investigation.

3 Description of the experimental setup

The geometrical device shown in Fig. 2 is represented by a physical model shown in Fig. 6. The wave energy absorber is equipped with an electric power generator via a linear actuator based on the electromagnetic principle. A linear movement, forced by the waves, generates a direct electromagnetic force without the use of mechanical devices such as cams, belts or gearboxes. The motor consists of two main parts: the slider and the stator. The slider is a precision assembly that consists of a stainless steel tube, which is filled with neodymium magnets. The stator, also called the bearing of the slider, contains the position sensors and a microprocessor board. The device is supplemented by a force and a displacement transducer. The displacement sensor consists of a laser measurement system which is mounted on top of the transducer. The unfiltered force signal and displacement signal were recorded at a sample frequency of 1000 Hz through the use of A/D converter. In total 5 wave gauges were placed around the float in order to accurately measure the incoming waves produced by the wave makers in the tank. The excitation moment was then calculated by means of a convolution integral between the measured wave elevation $\eta^m(t)$ and the linear impulse response function of the excitation moment $h_{\varphi 4}$, which was previously calculated by the use of the BEM code WAMIT, [19]. The following linear relationship was assumed for calculating the excitation moment based on the measured wave signal, Eqn. 19. This moment is then compared with the force which was measured in the load transducer multiplied with the lever arm. The results are plotted in Fig. 9, 11, 13 and 15 for regular and irregular waves respectively. In order to measure the force, the float was kept in a fixed position. In this case the actuator is in the displacement control mode. The numerical calculation of the excitation moment is given by:

$$M_{ex} = \int_{-\infty}^{\infty} h_{\varphi 4}(t-\tau)\eta^m(t)d\tau \qquad (19)$$

where $\eta^m(t)$ is the measured wave elevation at the position of the float, see Fig. 5. The numerical calculation of the rotational displacement is then calculated by using the measured time signal of the excitation moment. In this case the accumulated error is reduced.

TABLE 2. PLOTTED TIME SERIES, H=WAVE HEIGHT, T=WAVE PERIOD, λ=WAVE LENGTH, d=WATER DEPTH=0.65M

Waves:	$\frac{H}{\lambda}$	H	T	c_c	$\frac{H}{gT^2}$	$\frac{d}{gT^2}$
	$\frac{H_{m0}}{\lambda_p}$	H_{m0}	T_p		$\frac{H_{m0}}{gT_p^2}$	$\frac{d}{gT_p^2}$
	$[-]$	$[m]$	$[sec]$	$[kgm/s]$	$[-]$	$[-]$
Regular 1:	0.055	0.09	1.0	6	0.0096	0.066
Regular 2:	0.109	0.30	1.4	15	0.016	0.03
Irregular 1:	0.02	0.14	3.0	20	0.0016	0.007
Irregular 2:	0.04	0.28	3.0	20	0.003	0.007

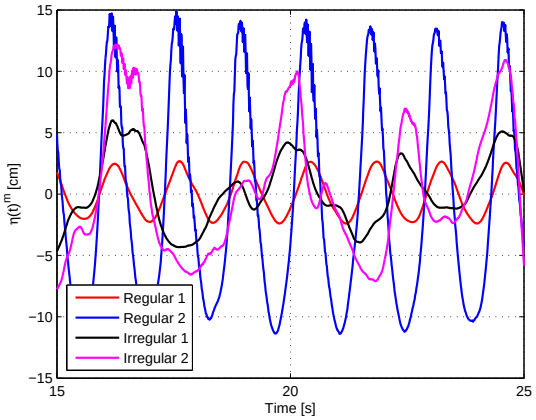

FIGURE 5. WAVE MEASUREMENT AT THE FLOAT FOR THE FOUR ANALYZED SIGNALS

FIGURE 6. REGULAR WAVES 2, $\frac{H}{\lambda} = 0.10$

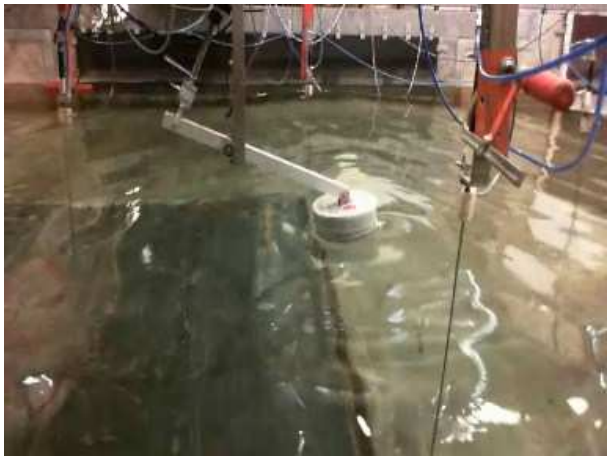

FIGURE 7. IRREGULAR WAVES 1, $\frac{H}{\lambda} = 0.02$

4 Results - Time series

Four different experimental time series were compared with the numerical calculation. Tab. 2 gives an overview which waves have been considered for the comparison. The irregular waves were calculated using a Pierson Moskowitz spectrum. For each wave state a number of runs have been analyzed varying the damping factor c_c to the value where the maximum power was measured by the system. For the regular waves the simulation time was approximately 60 sec, for irregular waves the measurement time was increased to 500 sec. In order to compare the time series, only 4 to 5 periods are shown in the plots. The numerical model is fed with the time series of the excitation moment which was measured with the force transducer holding the float in the fixed position. In the case of the irregular waves, the data series of the wave elevations had to be stored in order to reproduce the same signal when the device was in the floating position. In general good agreement was found between the results from the time domain solver and the experimental data.

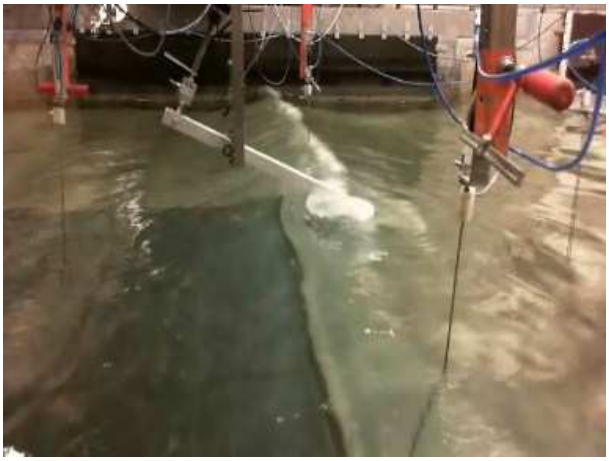

FIGURE 8. IRREGULAR WAVES 2, $\frac{H}{\lambda} = 0.04$

Regular 1 The measured force signal and the excitation moment based on the diffraction radiation theory are given in Fig. 9. The equation of motion is solved by using the measured force signal as an input and is then compared with the experimental rotations measured directly at the device, see Fig. 10. The latter comparison seems to be in very good agreement. It must be emphasized that due to technical limitations in the laboratory it was not possible to simulate purely linear waves which would require a factor of $\frac{H}{gT^2} <= 0.001$ for intermediate depth [20]. Thus all the wave signals which have been measured are described by higher order wave theories.

Regular 2 The float is overtopped at each wave crest passing the device, see Fig. 6. The force sensor is unable to measure the signal accurately due to the submergence of the float, see Fig. 11. Fig. 12 shows the rotational displacement, it can be concluded that the numerical model underestimates the dynamics of the float for the given wave heights and periods. Note that the non dimensional parameter is quiet high $\frac{H}{gT^2} <= 0.016$. The non linear shape of the waves can be observed in Fig. 5.

Irregular 1 Next, irregular waves have been measured and compared with the numerical calculations. The situation looks similar to the regular 1 wave, cf. first case. The excitation force based on the numerical calculation is accurately representing the measured signal. Moreover the rotational displacement seems to be in good agreement with the experiments. The assumptions of linear fluid-structure interaction can be adopted.

Irregular 2 In this case, irregular waves with a relative zero moment height to peak wavelength ratio of 0.04 were compared

with the numerical model. The overtopping of the device does not take place at each wave crest, compared to case 2 for steep regular waves.

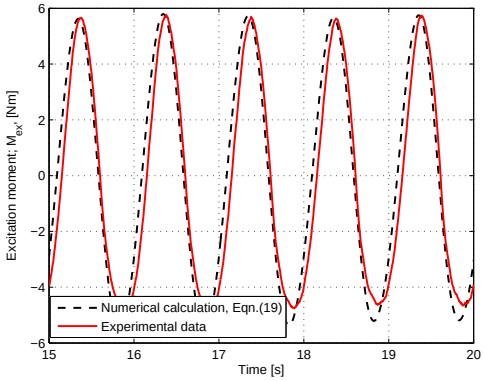

FIGURE 9. MEASURED MOMENT IN THE FIXED POSITION COMPARED WITH THE NUMERICAL CALCULATION, $H/\lambda = 0.05$

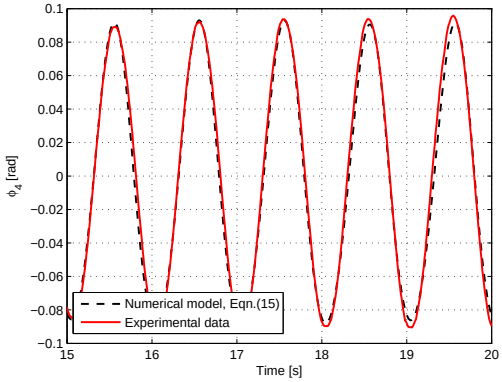

FIGURE 10. MEASURED ROTATIONAL DISPLACEMENT COMPARED WITH THE NUMERICAL MODEL, $H/\lambda = 0.05$

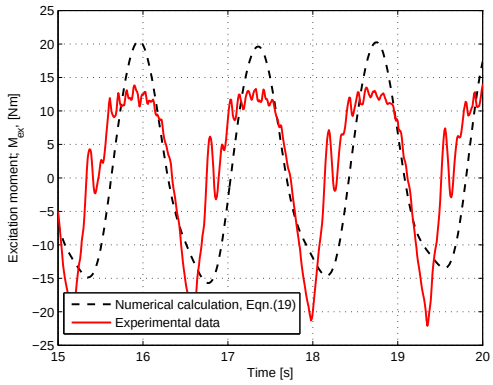

FIGURE 11. MEASURED MOMENT IN THE FIXED POSITION COMPARED WITH THE NUMERICAL CALCULATION, $H/\lambda = 0.10$

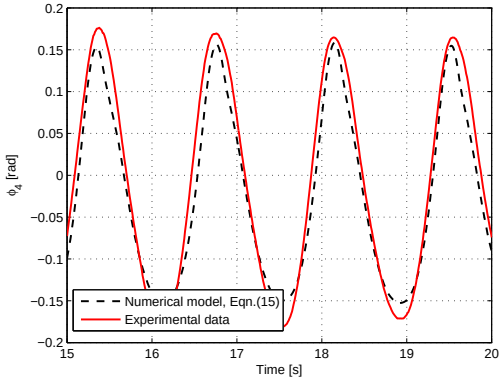

FIGURE 12. MEASURED ROTATIONAL DISPLACEMENT COMPARED WITH THE NUMERICAL MODEL, $H/\lambda = 0.10$

5 Conclusions

Two time domain models have been implemented in MATLAB describing the dynamics of the wave energy device shown in Fig. 2. The equation of motion is described by Cummins integro-differential equation which involves a convolution integral of the radiation force. A simplified power take off system has been introduced by means of a linear velocity proportional feedback force. The first method is based on a discretization of the convolution integral. The drawbacks of it are that it is time consuming, the convolution integral needs to be calculated at each time step and the impulse response function needs to be interpolated with the same time step as the time integration scheme. In the second model the convolution integral is replaced by a system of linear ordinary differential equations, which are solved numerically along with the equations of motion of the absorber. The two methods were compared with each other and the output

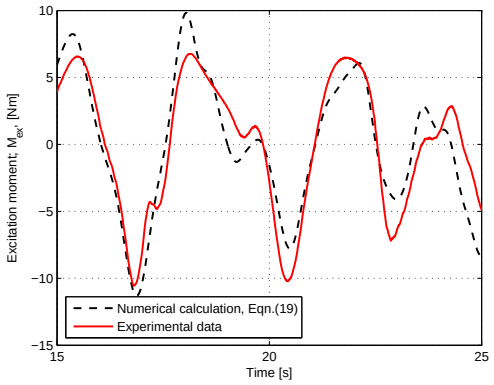

FIGURE 13. MEASURED MOMENT IN THE FIXED POSITION COMPARED WITH THE NUMERICAL CALCULATION , $H_{m0}/\lambda_p = 0.02$

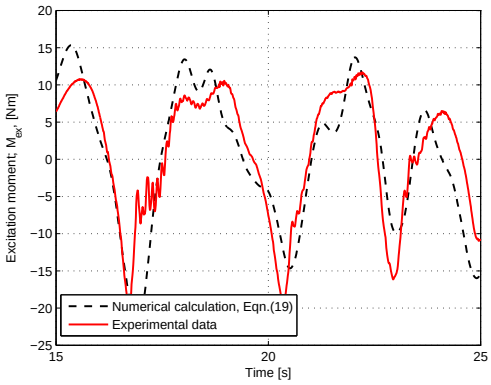

FIGURE 15. MEASURED MOMENT IN THE FIXED POSITION COMPARED WITH THE NUMERICAL CALCULATION, $H_{m0}/\lambda_p = 0.04$

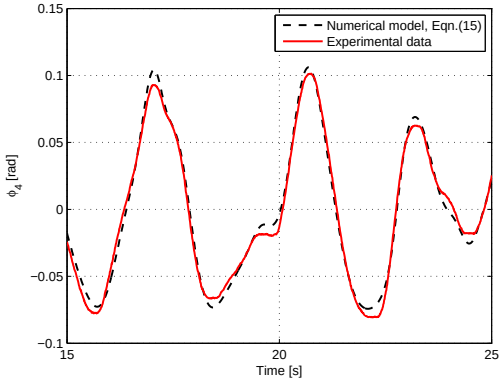

FIGURE 14. MEASURED ROTATIONAL DISPLACEMENT COMPARED WITH THE NUMERICAL MODEL, $H_{m0}/\lambda_p = 0.02$

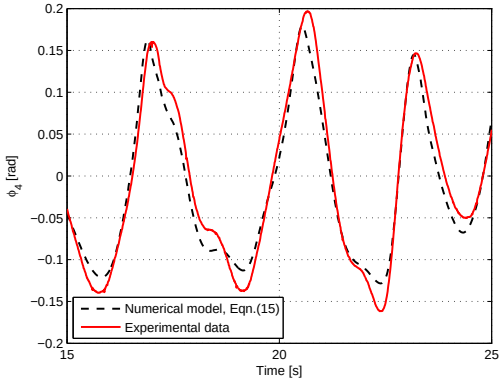

FIGURE 16. MEASURED ROTATIONAL DISPLACEMENT COMPARED WITH THE NUMERICAL MODEL, $H_{m0}/\lambda_p = 0.04$

results are in good agreement. The performance of the numerical model was then validated by means of experimental results. The comparison was carried out for four different waves, looking at the force moment measurement and the response i.e. the dynamics of the float. Two regular and two irregular waves with different wave height to wavelength ratios were compared. It can be concluded that for relatively mild steepness factors the numerical model based on linear-fluid structure interaction seems to be well adopted, provided that the input to the solver i.e the excitation force moment corresponds to the measured one. A numerical generated excitation force moment would most probably lead to inaccuracies as can be concluded from the plots. For higher steepness factors the numerical calculation seems to underestimate the dynamics of the float. The latter one is most probable due to the fact that non-linear effects such as non-linear hydrostatic restoring forces become important due to the high velocities and displacements of the float.

ACKNOWLEDGMENT

The authors wish to thank the financial support from the Danish Council for Strategic Research under the Programme Commission on Sustainable Energy and Environment (Contract 09-067257, Structural Design of Wave Energy Devices). The help of Francesco Ferri during the experimental tests is gratefully acknowledged.

REFERENCES

[1] Falnes, J. Ocean waves and oscillating systems: linear interactions including wave-energy extraction. Cambridge:

Cambridge University Press. 2002

[2] Neumann, F., Winands, V., Sarmento, A.J.N.A. Pico Shoreline OCW: status and new perspectives. Proceedings of the 2nd International Converence on Ocean Energy, ICOE, 2008

[3] Pelamis Wave Power. www.pelamiswave.com

[4] Wave Dragon. www.wavedragon.net

[5] Ruellan, M., BenAhmed, H.Multon, B., Josset, C., Babarit, A. and Clement, A. Design methodology for a SEAREV wave energy converter. IEEE Transactions on Energy Conversion, 25(3): 760.767, 2010.

[6] Wavestar Energy. www.wavestarenergy.com

[7] Taghipour, R. Efficient Prediciton of Dynamic Response for flexible and Multi-Body Marine Structures PhD Thesis, 2008

[8] Kashiwagi, M. A time-domain mode-expanison method for calulating transien reponses of a pontoon-type vlfs. Marine Science and Technology 5, 89-100, 2000

[9] Yu, Z. and Falnes, J. State-space modeling of a vertical cylinder in heave. Applied Ocean Research. 17:265-275, 1995

[10] Nielsen, S.R.K. Structural Dynamics, Vol, 3. Dept. of Civil Eng., Aalborg University. DCE Lecture Notes No. 11, 2007

[11] Perez, T. and Fossen, T. I. A Matlab Tool for parametric identification of radiation-force models of ships and offshore structures. Modelling, Identification and Control, MIC-30(1):1-15. 2009

[12] Hansen, R.H., Kramer, M.M. Modelling and Control of the Wavestar Prototype. EWTEC Conference - Proceedings, 2011

[13] Evans, D. V. Wave power absorbtion by oscillating bodies. J. Fluid Mech. 77(1) 1-25, 1976

[14] Nielsen, S.R.K, Kramer, M.M., Kirkegaard, P.H. Optimal control of wave energy absorbers. PhD course, 2011

[15] Kramer, M.M., Marquis, L., Frigaard, P. Performance Evaluation of the Wavestar Prototype. EWTEC Conference - Proceedings, 2011

[16] Fusco, F., Ringwood, J.V. Short-Term Wave Forecasting for Real-Time Control of Wave Energy Converters . IEEE Transactions on sustainable energy, Vol. 1, No.2, 2010

[17] Cummins, W.E. The impulse response function and ship motions. Schiffstechnik 9:101-109, 1962

[18] *Reference Guide*. The MathWorks, Natick, MA

[19] WAMIT manual. www.wamit.com.

[20] Le Mehaute, B. An Introduction to Hydrodynamics and Water Waves. Springer, New York